

# Tunable Metamaterial Leaky Wave Antenna based on Microwave Liquid Crystal Technology

Vom Fachbereich Elektrotechnik und Informationstechnik der Technischen  
Universität Darmstadt zur Erlangung des akademischen Grades eines  
Doktor-Ingenieurs (Dr.-Ing.) genehmigte

Dissertation

von

M.Sc.

María Roig Parras

geboren am 24. Mai 1983 in Madrid, Spanien

Referent:	Prof. Dr.-Ing Rolf Jakoby
Korreferent:	Prof. Dr.-Ing Ferran Martín Antolín
Tag der Einreichung:	14.7.2015
Tag der mündlichen Prüfung:	01.10.2015

D17

Darmstadt 2015



*Erklärung laut §9 PromO*

Ich versichere hiermit, dass ich die vorliegende Dissertation allein und nur unter Verwendung der angegebenen Literatur verfasst habe. Die Arbeit hat bisher noch nicht zu Prüfungszwecken gedient.

*Darmstadt den 14. Juli 2015*

---

María Roig Parras



---

## DEDICATORIA

---

Este trabajo está dedicado a mis padres, Manolo y Marian, como agradecimiento a sus impagables esfuerzos para darnos a mi hermana y a mí la educación y formación necesarias para disfrutar de oportunidades de otra forma inaccesibles y labrar nuestros propios caminos aunque ello significara separarnos.

Además, quiero agradecerles en estas líneas el haberme inculcado la cultura del esfuerzo y la dedicación como forma de superar dificultades y conseguir objetivos, pues es ésta, sin lugar a dudas, la convicción que más me ha ayudado a la hora de hacer frente a los obstáculos en el largo camino recorrido hasta hoy.

También quiero dedicarle esta tesis a mi hermana Silvia por ser fuente inagotable de ánimo y apoyo, y pilar fundamental de mi vida.



---

## ACKNOWLEDGEMENTS

---

The present dissertation was accomplished during my time as a research assistant at the Institute for Microwave Engineering and Photonics at the Technische Universität Darmstadt in Darmstadt, Germany. I would like to use the present document to thank all people that have contributed to this work to a greater extent.

First, I would like to thank my supervisor and *Doktorvater* Prof. Dr.-Ing. Rolf Jakoby for the opportunity and the trust he placed in me to develop the research work presented in this thesis. My gratitude extends to Prof. Dr. Ferrán Martín for co-supervising this work and his kind and encouraging manners in all our encounters.

I wish to express my deeply heartfelt gratitude to Prof. Dr.-Ing. Christian Damm and Dr. Matthias Maasch who crucially contributed to the successful outcome of this work with their guidance, multiple and fruitful discussions, advice, and helpfulness.

I take this opportunity to make special mention of the technical staff members Ms. Karin Boye, Mr. Peter Kieslich and Mr. Andreas Semrad who have always keenly advised me and helped me through the manufacturing process of my structures and setups.

Last, I wish to thank my family for their unconditional support, encouragement and patience during all this years, especially when the work left me little time for them.

Darmstadt, October 2015

*María Roig Parras*



---

## ABSTRACT

---

In this work, a continuously electrically tunable metamaterial leaky wave antenna for Ka-band applications is designed, manufactured and investigated, which features one dimensional beam steering capabilities.

The antenna concept is developed based on the theory of leaky wave antennas and metamaterials. Leaky wave antennas provide low profile and high directivity while metamaterials offer design flexibility by means of dispersion engineering. Additionally, liquid crystal is employed as tunable material to achieve voltage tunable beam scanning. The design, implementation and characterization of the voltage tunable metamaterial unit cell that makes up the leaky wave antenna is described in detail. The design and analysis of the dispersion characteristic of the unit cell is based on equivalent circuit, analytical and full-wave models. Moreover, tunability and loss analysis as well as far field investigations are carried out.

Since technological constraints limit the feasibility of the unit cell, their influence on the design and fabrication process of the antenna is analyzed. Considering these constraints, a fabrication process that combines microwave structures with resistive voltage biasing networks and liquid crystal cavities is developed in this work. Different manufactured antenna prototypes are presented. A magnetically biased leaky wave antenna, which uses a static magnetic field to achieve a beam steering at 27 GHz is used to demonstrate and investigate the proposed unit cell concept. In addition, an electrically biased leaky wave antenna, where the orientation of liquid crystal molecules is changed by a tuning voltage that yields voltage beam scanning capability around 27 GHz is developed. Simulation, vectorial network analysis and far field measurement results of both prototypes are compared and a detailed analysis of the magnetic and electric biasing techniques is presented. Response time investigations are carried out for the manufactured voltage tunable leaky wave antenna and the liquid crystal material utilized in this work.

The presented electrically tunable metamaterial leaky wave antenna concept in combination with the fabricated prototypes demonstrates that the usage

of continuously tunable metamaterials is a solid option for the realization of leaky wave antennas with a low profile at the Ka-Band. Moreover, due to the good electromagnetic properties of liquid crystal material at higher frequencies, the presented antenna concept and design methods can be applied for frequencies up to 4 THz, which is of particular importance for current and future applications in modern wireless communication systems.

---

## ZUSAMMENFASSUNG

---

In dieser Arbeit werden kontinuierlich elektrisch abstimmbare Metamaterial-Leckwellenantennen für Ka-Band-Anwendungen mit eindimensionaler Strahlschwenkung entworfen, hergestellt und untersucht.

Das entwickelte Antennenkonzept basiert auf der Verknüpfung von Leckwellenantennen und Metamaterialien. Leckwellenantennen bieten eine hohe Direktivität bei geringer Bauhöhe während Metamaterialien Flexibilität im Entwurfsprozess anhand ihrer Dispersionseigenschaften ermöglichen. Zusätzlich wird durch Einsatz von Flüssigkristallen als steuerbares Material eine spannungsgesteuerte Strahlschwenkung erreicht. Entwurf, Implementierung und Charakterisierung von spannungsgesteuerten Metamaterial-Einheitszellen, aus denen die Leckwellenantenne besteht, werden detailliert beschrieben. Der Entwurfsprozess und die Analyse der Dispersionseigenschaften sowie der Steuerbarkeit von Einheitszellen werden anhand von Ersatzschaltbildern und analytischen sowie Vollwellen-Modellen durchgeführt. Weiterhin werden Toleranz- und Verlustanalysen sowie Fernfelduntersuchen durchgeführt. Außerdem werden technologische Randbedingungen, die die Realisierbarkeit der untersuchten Einheitszellen einschränken, sowie der Einfluss von Entwurfs- und Herstellungstoleranzen auf die Antenne untersucht. Darüber hinaus wird ein Herstellungsprozess zur Kombination der Mikrowellenstrukturen mit resistiven Speisernetzwerken und Flüssigkristallkavitäten umfassend untersucht und in dieser Arbeit vorgestellt.

Verschiedene aufgebaute Antennenprototypen werden präsentiert. Anhand einer magnetisch steuerbaren Leckwellenantenne für 27 GHz, welche ein statisches Magnetfeld zur Strahlschwenkung benutzt, wird das vorgestellte Einheitszellen-Konzept demonstriert und untersucht. Zusätzlich wird eine elektrisch steuerbare Leckwellenantenne präsentiert, bei der die Orientierung von Flüssigkristallmolekülen und damit eine Strahlschwenkung bei etwa 27 GHz durch Anlegen einer variablen Spannung realisiert wird. Simulationsergebnisse, vektorielle Netzwerkanalysen und Fernfeldmessungen beider Prototypen werden verglichen und eine detaillierte Analyse der magnetischen sowie elektrischen Steuerung durchgeführt. Darüber hinaus werden die Steuerzeiten

der aufgebauten elektrisch steuerbaren Leckwellenantenne mit dem in dieser Arbeit verwendeten Flüssigkristall ermittelt.

Die in dieser Arbeit vorgestellten Konzepte in Verbindung mit gefertigten Prototypen zeigen, dass der Einsatz von kontinuierlich abstimmbaren Metamaterialien eine zuverlässige Möglichkeit bietet, elektrisch steuerbare Leckwellenantennen für das Ka-Band zu realisieren. Aufgrund der guten elektromagnetischen Eigenschaften von Flüssigkristallen bei höheren Frequenzen, ist das dargestellte Antennenkonzept sowie Entwurfsmethoden für Frequenzen bis mindestens 4 THz anwendbar. Dies ist insbesondere für aktuelle und zukünftige Anwendungen in modernen, drahtlosen Kommunikationssystemen von großer Bedeutung.

---

## CONTENTS

---

1	INTRODUCTION	1
1.1	Thesis Outline . . . . .	5
2	TUNABLE PLANAR METAMATERIAL STRUCTURES	7
2.1	Dispersion Characteristics of Periodic Structures . . . . .	7
2.1.1	The Transmission Line Model Applied to Periodic Structures . . . . .	8
2.1.2	The Composite Right-/Left-handed Unit Cell . . . . .	12
2.2	Tunable Metamaterials . . . . .	15
2.2.1	Tuning Techniques . . . . .	16
2.2.2	Tuning of Nematic Liquid Crystal . . . . .	17
2.3	Extraction Methods . . . . .	21
2.3.1	Complex Scattering Parameters Matrix . . . . .	21
2.3.2	Eigenmode Analysis . . . . .	22
3	METAMATERIAL BASED LEAKY WAVE ANTENNAS	23
3.1	Traditional Leaky Wave Antennas . . . . .	24
3.2	Metamaterial based Leaky Wave Antennas . . . . .	28
4	TUNABLE METAMATERIAL UNIT CELL DESIGN AND IMPLEMENTATION	31
4.1	Dispersion Engineering of the Unit Cell and Working Principle of the Leaky Wave Antenna . . . . .	32
4.2	Implementation of the Unit Cell . . . . .	36
4.2.1	Circuit Simulation and Layout Implementation . . . . .	38
4.2.2	Full-wave Analysis . . . . .	42
4.2.3	Distributed Lumped Elements Calculation . . . . .	44
4.3	Fabrication Process . . . . .	47
4.4	Tunability Analysis of the Composite Right-/Left-Handed Unit Cell	50
4.5	Tolerance Analysis . . . . .	53
4.6	Loss Analysis . . . . .	67
5	LIQUID CRYSTAL BASED TUNABLE METAMATERIAL LEAKY WAVE ANTENNA	71
5.1	Tuning Techniques: Design and Implementation . . . . .	71

- 5.1.1 Magnetic Tuning . . . . . 72
- 5.1.2 Electric Tuning . . . . . 73
- 5.2 Magnetically biased Leaky Wave Antenna . . . . . 75
  - 5.2.1 Dispersion Characteristics . . . . . 77
  - 5.2.2 Calculation of Far Field Patterns of Leaky Wave Antennas. . . . . 80
  - 5.2.3 Directivity Calculations . . . . . 82
  - 5.2.4 Measured Radiation Pattern . . . . . 84
- 5.3 Electrically biased Leaky Wave Antenna . . . . . 87
  - 5.3.1 Dispersion Characteristics . . . . . 87
  - 5.3.2 Impact of the Biasing Circuitry on the Dispersion Characteristic . . . . . 91
  - 5.3.3 Directivity Calculations . . . . . 91
  - 5.3.4 Measured Radiation Pattern . . . . . 94
  - 5.3.5 Cross Polarization Measurement . . . . . 96
  - 5.3.6 Radiation Efficiency . . . . . 98
  - 5.3.7 Response Time Investigations . . . . . 100
  
- 6 CONCLUSION AND OUTLOOK . . . . . 105
  
- A APPENDIX . . . . . 111
  - A.1 Capacitance Calculation Method for Multilayered Substrate Based Interdigital Capacitors . . . . . 111
  - A.2 Inductance Calculation Method for a Composite Right-/Left-Handed Unit Cell Meander Inductor . . . . . 113
  
- List of Abbreviations . . . . . 117
  
- List of Symbols . . . . . 119
  
- Bibliography . . . . . 123
  
- List of Publications of the Author . . . . . 133

---

## INTRODUCTION

---

Modern wireless communication systems have experienced an exponential growth in the past decades. Antennas, as one of the key components of communications systems front-end, have a direct impact on the performance and limitations of such systems. As the number of users and applications grows, communication systems become more complex and the antennas within them have to fulfill new requirements such as low power consumption (if they are tunable), reduced size and weight, ease of mass production, and low cost.

The concept of leaky wave antennas (LWAs) was initially introduced in the first half of the twentieth century but it was not until the past decades when the development of planar LWAs drew interest on this category of structures due to their multiple advantages like narrow and highly directive beams, inherently simple feeding network, and reduced profile. All of these characteristics make LWAs a solid candidate to overcome many of the mentioned challenges faced by contemporary communication systems. Furthermore, the low profile and relative ease of manufacturing [1] make them ideally suited for modern communication systems since they yield high quality RF performance at low cost [2].

The combination of LWAs with metamaterials has proved to be an advantageous association due to the unique properties of these artificial materials. Metamaterials increase the design flexibility of these antennas and allow for meeting more demanding requirements, e.g. planarity. Metamaterials can be designed as planar structures, resulting in a reduced size and low profile. Choosing the proper unit cell configuration, they can be designed to provide continuous radiation from backfire to endfire, including the broadside direction [3–6], which has traditionally been an issue for classical leaky wave antennas.

Moreover, metamaterials lead to major flexibility in the design of LWA since it is possible to tailor the dispersion response of the unit cell to obtain a desired dispersion characteristic, which, in turn, is responsible for the radiation characteristic of the metamaterial based LWA.

The first steps towards this type of antennas date back to the year 2002 when Grbic and Eleftheriades proposed and demonstrated a backward radiating metamaterial transmission line [7] and its application as a leaky wave antenna [8]. In these works, a leaky wave antenna based on the metamaterial transmission line approach is presented. The antenna consists of a negative refractive index transmission line that enabled the antenna to radiate in the backward quadrant from backfire to broadside by scanning with frequency. However, scanning with frequency is not reasonable for communications using a frequency band.

The first composite right-/left-handed (CRLH) based leaky wave antennas were presented by Eleftheriades [9] and Liu [10] also in 2002. From this point on, many leaky wave antennas based on this metamaterial configuration have been studied in different technologies such as microstrip [11–14], coplanar waveguide [15–18], slotted line [19–21], rectangular hollow waveguides [22, 23] and, more recently, substrate integrated waveguides [24–27]. Besides the different available technologies and their impact in the design and performance of these antennas, other aspects of CRLH based leaky wave antennas have been considered, such as tapering of the unit cell size in order to increase the bandwidth [28] or to improve the side lobe level [29]. Integration of further well known metamaterial elements, such as split-ring resonators, in the unit cell to achieve the mentioned CRLH configuration [30] and analyze their impact on the performance of the leaky wave antenna [31] has also awaken interest in the past years.

Other authors have focused on the enhancement of the CRLH leaky wave antenna characteristics for instance, higher gain [32], polarization reconfigurability [33] or counteracting the effect of substrate bending on the electronic beam focusing process [5, 34]. The enhancement of the CRLH based leaky wave antennas performance in terms of beam steering, directivity, and side lobe level is currently one of the major interest fields regarding this type of metamaterial antenna since their inherent characteristics make them suitable for applications such as radiolink communications [35], where cylindrical CRLH leaky wave antennas are used.

Most CRLH leaky wave antennas with different topologies, applications, and manufacturing technologies use frequency tuning in order to achieve beam steering, such as the prototype presented in [36] which is based on substrate integrated waveguide technology. In [37], a CRLH leaky wave antenna is used to steer the radiation beam from the backward to the forward quadrant by scanning the frequency from 3.4 GHz to 4.3 GHz. Other authors have made use of the CRLH concept combining it with purpose-tailored materials such as ferrites [38].

Nevertheless, in contrast to frequency scanning, it is desirable for many applications, in particular in broadcasting and communications, where a frequency band containing the information is used, to perform beam steering at a fixed operation frequency. This can be realized by using semiconductor varactors [39, 40] or p-i-n diodes [41]. However, the poor performance of these tuning elements at high frequencies, limits the operation frequency to about 7 GHz. For higher operation frequencies, it is possible to use liquid crystal (LC) at its nematic phase as a continuously tunable anisotropic dielectric [42]. When a static electric or magnetic field is applied, the LC molecules tend to orient parallel to it. This varies the permittivity encountered by the electric RF field, which tunes the radiation angle of the antenna. Hence, the tuning of the radiation angle is influenced by the tunability of the LC based varactors. This approach is proposed in [23] where a waveguide based metamaterial leaky wave antenna is presented. In this case, the antenna achieves continuous beam scanning but the beam scanning range is limited to  $\pm 10^\circ$ . Furthermore, it works at a relatively low frequency of 7.6 GHz.

In this work, a voltage tunable leaky wave antenna operated at the Ka-Band is designed, implemented, and analyzed. The working principle for such an antenna is based in the dispersion characteristic of the phase constant  $\beta$ . Leaky wave antennas usually take advantage of this effect by using frequency scanning in order to perform beam steering, since a small change in the frequency implies a significant variation in the phase shift and thus the radiation angle  $\psi$ .

In order to perform beam scanning without varying the frequency, it is required that the presented antenna is able to change between a positive and a negative value of  $\beta$ . According to the radiation properties of LWAs, for a positive  $\beta$  the LWA radiates in the forward quadrant while for a negative  $\beta$  the LWA radiates in the backward quadrant. The tuning between positive and negative  $\beta$  can be done using varactors that vary the phase constant of the propagating wave. Varactor tunability is accomplished in this work by the

usage of liquid crystal as a continuously tunable anisotropic dielectric since it shows reduced losses and good performance at microwave frequencies.

The varactor is implemented within the novel and purposely designed meta-material unit cell that makes up the proposed LWA prototypes by periodical repetition. The investigation, design, and characterization of the unit cell is the major and most challenging part of this work. Being essential to provide the LWA with the desired scanning behavior, its design and implementation is strongly influenced by the high operating frequency and the technological constraints derived from it. These two aspects, combined with the chosen CRLH configuration, lead to a novel unit cell geometry with continuous tuning capabilities around 27 GHz.

The developed tunable unit cell is employed in two manufactured LWA prototypes presented in this work as a proof-of-concept. For fundamental investigations of the liquid crystal loaded unit cell, one of the presented prototypes is a magnetically biased leaky wave antenna. For the magnetic tuning of the liquid crystal two rare earth magnets with a field strength of 1.4 T are used. For the far field measurements, a specific magnetic biasing setup is designed and fabricated. The magnetically biased LWA shows a beam steering capability of  $11^\circ$  at 27 GHz.

The second prototype is an electrically biased leaky wave antenna, where the orientation of the LC molecules is performed by applying a tuning voltage between 0 V and 60 V. For this LWA, the layout of the unit cell is modified to implement the biasing network, responsible for distributing the biasing voltage along the antenna. This planar biasing network concept is based on highly resistive nickel-chromium lines that distribute the DC tuning voltage. Their resistive characteristic prevents the propagation of the RF signal along the biasing circuitry thus minimizing the parasitic effects introduced by the biasing network on the overall performance of the antenna. The electrically biased LWA shows a beam steering capability of  $15^\circ$ , from  $-6^\circ$  to  $9^\circ$ , with respect to broadside at 26.7 GHz.

Simulations, vectorial network analysis, and far field measurements of both prototypes are also presented to characterize and analyze the performance. In addition, response time investigations show that for the utilized liquid crystal and the proposed geometry, the electrically biased leaky wave antenna needs 9 s to the steer beam from  $-6^\circ$  to  $9^\circ$  by an applied tuning voltage of 120 V.

To the best knowledge of the author, this is the first voltage tunable liquid crystal based metamaterial leaky wave antenna being fabricated as prototype,

capable of performing continuous beam scanning from backward to forward quadrant though the broadside direction at the Ka-band.

The presented electrically tunable metamaterial leaky wave antenna concept in combination with the fabricated prototypes demonstrates the feasibility of continuously tunable metamaterials as a solid option to produce leaky wave antennas with a low profile at the Ka-Band. Moreover, this concept can be scaled up to higher frequencies due to the good performance shown by liquid crystal for frequencies up to 4 THz, which is especially convenient for current and future applications in modern wireless communication systems in the mm-wave and THz range.

## 1.1 THESIS OUTLINE

The second chapter of this thesis is an introduction to metamaterials and their dispersive nature, which is the basis of this work. In this chapter, the properties of the composite right-/left-handed unit cell are analyzed in detail and a description is given of how these may be controlled at discretion to obtain the desired response in frequency. Moreover, the basics of liquid crystal and its application as a continuously tunable dielectric are presented. Finally, possible simulation and extraction methods that can be used for the design and measurement of the leaky wave antenna parameters are analyzed.

Chapter three focuses on the concept of leaky wave antennas. Their working principle in combination with the dispersion characteristic of metamaterials enables the beam scanning behavior which is the subject of this work. In addition, an overview of the different LWA concepts and main characteristics of leaky wave antennas is provided.

The fourth chapter focuses on the design, implementation and analysis of the unit cell that forms the leaky wave antenna. The unit cell, based on the composite right-/left-handed configuration, unites the advantages of metamaterials with those of the leaky wave antenna introduced in the previous two chapters. A detailed description of the unit cell layout design is given, taking into account size, shape, and geometry in order to control the scanning behavior of the antenna. Furthermore, the manufacturing process of the unit cell and the antenna is described in detail. The effect of the tolerances, introduced by the manufacturing process, on the performance of the unit cell and, hence, the leaky wave antenna is investigated in a tolerance analysis.

Finally, a further analysis of losses and their influence on the performance of the unit cell is carried out.

Chapter five presents two fabricated prototypes based on the unit cell introduced in chapter four. The first prototype is magnetically biased and consists of fifteen unit cells. This prototype is designed and fabricated as a proof-of-concept. The second leaky wave antenna prototype is electrically biased and includes a biasing network. The design and implementation of this antenna, with 32 unit cells, is the goal of this thesis. For both antennas, the effect of the different biasing techniques on the antenna performance, advantages and disadvantages are analyzed in detail. The simulated and measured phase shift, impedance, radiation angle, beam scanning range and far field pattern are presented together with further antenna parameters such as half power beam width, side lobe level, and cross-polarization. In addition, the time response performance of the electrically biased leaky wave antenna is analyzed.

In the sixth chapter, a summary of the work, the main concepts introduced in each chapter, and the most significant obtained results are presented and commented. Finally, an outlook to future work perspectives and potential applications is given.

---

## TUNABLE PLANAR METAMATERIAL STRUCTURES

---

Metamaterials are defined in literature mostly as artificial materials engineered to have advantageous and unusual properties that can otherwise not be found in nature. These properties derive from specific individual, smaller than wavelength, and normally periodically arranged elements incorporated to traditional materials in a specifically designed manner to obtain the desired electromagnetic response. This implies that the properties of metamaterials actually depend not only on their chemical composition but also on their geometry, shape, size and even orientation regarding the propagating wave.

For the periodic structures in this work, the lattice constant, the distance between elements, is much smaller than the propagating wavelength. If this condition is satisfied, it is possible to characterize the material by its effective parameters and refer to it as a metamaterial [43]. This statement is analyzed in the following section.

### 2.1 DISPERSION CHARACTERISTICS OF PERIODIC STRUCTURES

A periodic structure, as depicted in Fig. 2.1, is formed by the constant repetition of a basic element, denominated lattice or unit cell. At infinitely long periodic structures, the voltages and currents along the structure have a periodic nature [44, 45], i.e. their magnitude stays constant whereas their phase varies periodically along the length of the structure. The periodicity of the voltages and the currents along a periodic structure is advantageous, since knowing  $V$  and  $I$  at a certain point  $z_0$  enables the calculation of both parameters at any other point of interest of the periodic structure by just calculating the phase shift between that point and  $z_0$ . For the periodic structures investi-

gated in this work, this represents the possibility of determining the behavior of the propagating wave at each interface of the unit cell and thus the microwave characteristic of the whole periodic structure. The electromagnetic behavior of the propagating wave can be, hence, described by the characteristic dispersion properties of a single unit cell. These dispersion properties are determined by the relation between the voltages and currents at the unit cell interfaces and the effect of the unit cell on the propagation constant  $\gamma$  of the propagating wave.

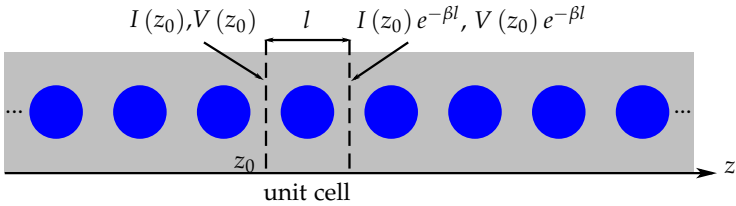


Figure 2.1: Infinitely long periodic structure and its unit cell.

The unit cell characteristic behavior is described by the Bloch impedance  $Z_B$  and the propagation shift within the unit cell,  $\gamma l$ . The Bloch impedance  $Z_B$  is the impedance at the input and output ports of the unit cell, whereas  $\gamma$  is the propagation constant within the periodic structure.

In a periodic waveguiding structure, when the unit cell size is small and  $l \rightarrow 0$ , the periodic structure is considered to become a uniform one. In this case, the Bloch impedance  $Z_B$ , which is only defined at the ports of the unit cell, can be approximated by the characteristic impedance  $Z_c$ , which is invariant along the waveguiding structure for the operating frequency  $f_0$ .

Since the work presented in this thesis focuses on a leaky wave antenna based on a periodical transmission line metamaterial, a detailed analysis of such an approach will be carried out considering a two conductor transmission line model.

### 2.1.1 The Transmission Line Model Applied to Periodic Structures

A short transmission line section is shown in Fig.2.2. Due to causality, the current and voltage at the output of the section are directly dependent on the

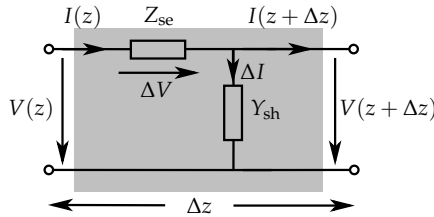


Figure 2.2: Transmission line section with a finite length.

current and voltage at its input, respectively. If the transmission line section has an incremental length of  $\Delta z$ , then

$$V(z + \Delta z) = V(z) - \Delta V = V(z) - I(z) \cdot Z_{se} \quad (2.1)$$

and

$$\begin{aligned} I(z + \Delta z) &= I(z) - \Delta I = I(z) - (V(z) - I(z) \cdot Z_{se}) \cdot Y_{sh} \\ &= I(z) - (V(z) - \Delta V) \cdot Y_{sh}. \end{aligned} \quad (2.2)$$

$Z_{se}$  is the series impedance,  $Y_{sh}$  the shunt branch admittance,  $\Delta V = I(z) \cdot Z_{se}$  is the voltage over the series impedance  $Z_{se}$ , and  $\Delta I = (V(z) - \Delta V) \cdot Y_{sh}$  is the current through admittance  $Y_{sh}$ .

Regrouping terms and dividing equations by  $\Delta z$ ,

$$\frac{V(z + \Delta z) - V(z)}{\Delta z} = - \frac{I(z) \cdot Z_{se}}{\Delta z} \quad (2.3)$$

$$\frac{I(z + \Delta z) - I(z)}{\Delta z} = - \frac{(V(z) \cdot Y_{sh} - \Delta V \cdot Y_{sh})}{\Delta z} \quad (2.4)$$

are obtained.

To apply the equations defined above for the unit cell at any point of the artificial periodic waveguiding structure, this has to be homogeneous. If the periodic waveguiding structure is homogeneous, then voltages and currents and, hence, impedance and propagation shift can be calculated independently of the total length of the periodic waveguiding structure, i.e. independently of the amount of unit cells. To verify the homogeneity of the considered artificial transmission line, an infinitesimally short section is considered. For this

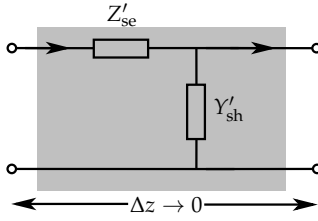


Figure 2.3: Infinitesimally short section of a transmission line.

purpose, it is considered that the finite section length represented in Fig. 2.2 tends to zero,  $\Delta z \rightarrow 0$  (which implies that the voltage over  $Z_{se}$  also tends to zero,  $\Delta V \rightarrow 0$ ). As shown in Fig. 2.3, under this condition,  $Z_{se}$  and  $Y_{sh}$  become distributed immittances,

$$Z'_{se} = \lim_{\Delta z \rightarrow 0} \frac{Z_{se}}{\Delta z} \quad (2.5)$$

and

$$Y'_{sh} = \lim_{\Delta z \rightarrow 0} \frac{Y_{sh}}{\Delta z}, \quad (2.6)$$

respectively. Accordingly, equations (2.3) and (2.4) can be expressed as

$$\frac{\delta V(z)}{\delta z} = -I(z) \cdot Z'_{se}, \quad (2.7)$$

and

$$\frac{\delta I(z)}{\delta z} = -V(z) \cdot Y'_{sh}. \quad (2.8)$$

Substituting equations (2.7) and (2.8) in each other, second order differential equations are obtained for both the voltage and the current

$$\frac{\delta^2 V(z)}{\delta z^2} - V(z) \cdot Y'_{sh} Z'_{se} = 0, \quad (2.9)$$

$$\frac{\delta^2 I(z)}{\delta z^2} - I(z) \cdot Y'_{sh} Z'_{se} = 0, \quad (2.10)$$

which describe the propagation of waves in a transmission line in the  $z$  direction. The general solution for this kind of equation, is given in the form of  $c_1 \cdot e^{-kz} + c_2 \cdot e^{kz}$ . Applying this to (2.9) and (2.10), the solutions

$$V(z) = V_0^+ \cdot e^{-\gamma z} + V_0^- \cdot e^{\gamma z} \quad (2.11)$$

and

$$I(z) = I_0^+ \cdot e^{-\gamma z} + I_0^- \cdot e^{\gamma z} \quad (2.12)$$

are obtained for voltage and current at a certain point  $z$  of the homogeneous transmission line.  $V_0^+$  and  $V_0^-$  are the amplitudes of the forward and backward propagating voltages, respectively, while  $I_0^+$  and  $I_0^-$  are the amplitudes of the forward and backward propagating currents. Since the voltage and current are directly related by means of the characteristic impedance  $Z_c$ , it is also possible to express the current as

$$I(z) = \frac{V_0^+ \cdot e^{-\gamma z} - V_0^- \cdot e^{\gamma z}}{Z_c}. \quad (2.13)$$

In equations (2.11)-(2.13),

$$\gamma = \alpha + j\beta = \pm \sqrt{Z'_{se} Y'_{sh}} \quad (2.14)$$

is the propagation constant within the transmission line, where  $\alpha$  and  $\beta$  are the attenuation and phase constants, respectively, and  $Z_c$  its characteristic line impedance, which is defined as

$$Z_c = \pm \sqrt{\frac{Z'_{se}}{Y'_{sh}}}. \quad (2.15)$$

The propagation constant  $\gamma$  and the characteristic impedance  $Z_c$  are determined by the distributed admittance and impedance that form the transmission line. This implies that, the performance of such a transmission line can be tailored and controlled to meet the desired design specifications in frequency by manipulating  $Z'_{se}$  and  $Y'_{sh}$ .

On one hand, by choosing the proper elements that form  $Z'_{se}$  and  $Y'_{sh}$ , it is possible to control the propagation of the wave along the transmission line and the impedance it encounters. On the other, by following the opposite process, it is possible from a desired propagation characteristic and impedance to obtain the necessary elements that form the transmission line that meet such

requirements. This property is what makes the transmission line model such a powerful tool for the analysis and design of periodic structures. Metamaterial structures have to be not only periodical but also satisfy the homogeneity condition in order to apply the transmission line model.

Metamaterials are often considered to be homogeneous when their average cell size  $l$  is smaller than  $\lambda_g/10$  [45, 46]. Satisfying this condition and, hence, considering metamaterials as homogeneous media implies that metamaterials analysis can be approached by the transmission line model [45], which means that the waveguiding structure and thus the unit cell, can be considered uniform and homogeneous.

### 2.1.2 The Composite Right-/Left-handed Unit Cell

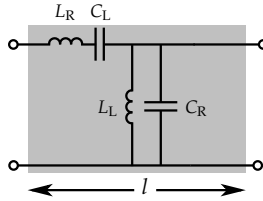


Figure 2.4: Ideal composite right-/left-handed Unit Cell.

The definition of characteristic impedance  $Z_c$  and propagation constant  $\gamma$  as a function of  $Z_{se}$  and  $Y_{sh}$  is valid for any transmission line that is homogeneous and can be divided into periodic infinitesimally short sections, independently of the value of  $Z_{se}$  and  $Y_{sh}$ . If  $Z_{se}$  and  $Y_{sh}$  are substituted by lumped capacitors and inductances as depicted in Fig. 2.4, then a composite right-/left-handed (CRLH) unit cell is obtained.

The CRLH unit cell equivalent circuit is formed by an inductance  $L_R$  and a capacitance  $C_L$  in the series branch and another inductance  $L_L$  and capacitance  $C_R$  in the shunt branch. If the CRLH unit cell is at least ten times smaller

than the guided wavelength,  $l < \lambda_g/10$ , the different elements of the CRLH unit cell can be defined as

$$\begin{aligned} L_R &= L'_R \Delta l, & C_R &= C'_R \Delta l, \\ L_L &= \frac{L'_L}{\Delta l}, & C_L &= \frac{C'_L}{\Delta l}, \end{aligned}$$

and the series and shunt immittances become

$$Z_{se}^{\text{CRLH}} = Z'_{L'_R} + Z'_{C'_L} = j\omega L'_R + \frac{1}{j\omega C'_L}, \quad (2.16)$$

$$Y_{sh}^{\text{CRLH}} = Y'_{L'_L} + Y'_{C'_R} = \frac{1}{j\omega L'_L} + j\omega C'_R, \quad (2.17)$$

respectively.

Following equations (2.14) and (2.15), the propagation constant  $\gamma$  and the characteristic line impedance of the CRLH transmission line become

$$\begin{aligned} \gamma^{\text{CRLH}} &= \alpha + j\beta = \pm \sqrt{Z_{se}^{\text{CRLH}} Y_{sh}^{\text{CRLH}}} \\ &= \pm j \sqrt{\omega^2 L'_R C'_R + \frac{1}{\omega^2 C'_L L'_L} - \left( \frac{L'_R}{L'_L} + \frac{C'_R}{C'_L} \right)} \\ &= \pm \frac{j}{\omega} \sqrt{L'_R C'_R (\omega^2 - \omega_{se}^2) (\omega^2 - \omega_{sh}^2)} \end{aligned} \quad (2.18)$$

and

$$Z_c^{\text{CRLH}} = \pm \sqrt{\frac{Z_{se}^{\text{CRLH}}}{Y_{sh}^{\text{CRLH}}}} = \pm \sqrt{\frac{L'_L}{C'_L}} \sqrt{\frac{\omega^2 L'_R C'_L - 1}{\omega^2 C'_R L'_L - 1}}. \quad (2.19)$$

The series inductance  $L'_R$  and shunt capacitance  $C'_R$ , represent the conventional transmission line model and are responsible for the right-handed propagation band (RHB) whereas the series capacitance  $C'_L$  and shunt inductance  $L'_L$  generate the left-handed propagation band (LHB). The transition from the LHB to the RHB of the CRLH unit cell can be described by its shunt and series branch frequencies, i.e.  $\omega_{sh}$  and  $\omega_{se}$ , where the shunt frequency is defined as

$$\omega_{sh} = \sqrt{\frac{1}{C'_R L'_L}} \quad (2.20)$$

and the series frequency as

$$\omega_{se} = \frac{1}{\sqrt{C'_L L'_R}}. \quad (2.21)$$

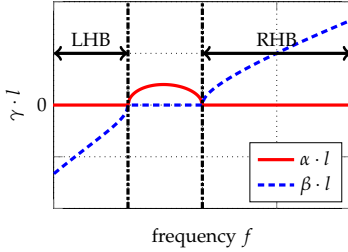


Figure 2.5: Dispersion characteristic of an unbalanced CRLH.

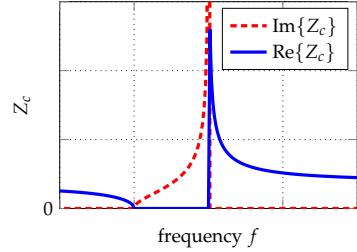


Figure 2.6: Impedance of the unbalanced CRLH.

For the case that  $\omega_{sh}$  and  $\omega_{se}$  have different values, the CRLH is unbalanced and a stopband appears between both frequencies. Within the stopband, the phase shift per unit cell is zero, as it can be seen in Fig. 2.5. In this case, since the group velocity

$$v_g = \frac{\partial \omega}{\partial \beta} \quad (2.22)$$

equals zero, no energy propagates along the structure. The effect of the stopband on the characteristic impedance is shown in Fig. 2.6. As it can be observed, the impedance is purely real below and above the stopband, which is, in turn, limited by a zero and a pole.

The position of the zero and the pole depends on the value of  $\omega_{sh}$  and  $\omega_{se}$ , respectively. The imaginary part of the impedance  $\text{Im}\{Z_c\}$  is always zero in the transmission bands and becomes non zero within the stopband. The slope of  $\text{Im}\{Z_c\}$  within the stopband must always be positive in order to satisfy the Foster's theorem [47].

In the LHB, the phase constant  $\beta$  and thus the phase velocity

$$v_{ph} = \frac{\omega}{\beta} \quad (2.23)$$

have a negative value, which means that the phase propagates backwards. This characteristic is especially important for metamaterial based LWAs since

it allows the scanning in the backward quadrant. The radiation mechanism of a LWA in the backward quadrant is further explained in chapter 3. In the RHB the phase constant  $\beta$  and, therefore, the phase velocity  $v_{ph}$  are both positive [40].

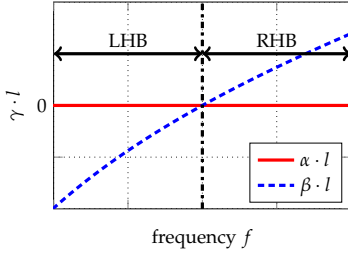


Figure 2.7: Dispersion characteristic of a balanced CRLH.

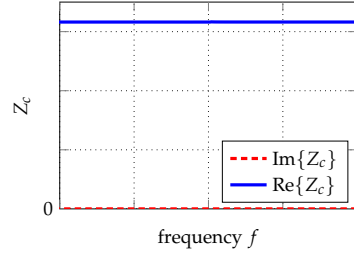


Figure 2.8: Impedance of the balanced CRLH.

When  $\omega_{sh} = \omega_{se}$ , the CRLH is balanced and the propagation constant equals zero for a unique frequency [48] as shown in Fig. 2.7. In that case, the characteristic impedance of the CRLH unit cell has a constant real value along frequency. The imaginary part of the impedance  $\text{Im}\{Z_c\}$  is always zero. This can be seen in Fig. 2.8. It is important to notice that, although the phase constant  $\beta = 0$  and thus the phase velocity  $v_{ph}$  equals zero, the group velocity is not zero, since the slope of the phase shift curve is positive. This implies that, although  $\beta = 0$  there is propagation of energy. Exactly this effect is the basis of the broadside radiation of the LWA studied in this work.

The dispersive response of the CRLH unit cell can be tailored to obtain the desired propagation constant, characteristic impedance, and group velocity by setting the proper values of the distributed lumped elements. This design flexibility is of utmost importance for the present work since it enables the design of the propagation and stopbands, which are responsible for the radiation characteristic of the metamaterial based LWA.

## 2.2 TUNABLE METAMATERIALS

Tunable metamaterials are those with the capability of varying their response to an electromagnetic stimulus. Tunability allows tailoring of the electromagnetic response of metamaterials according to the intended application or ef-

fect. In this manner, incident waves can be absorbed, transmitted or reflected and thus tunable metamaterials are often used in sensors, frequency selective surfaces (FSS), absorbers, tunable filters and antennas, lenses, electromagnetic cloaking for RF communications or even matching networks.

### 2.2.1 *Tuning Techniques*

There are several methods that enable the implementation of tunable metamaterials [49]. For instance, tuning the elements in the unit cell circuit by inserting or modifying the impedance of one or several of them. For this purpose, tunable capacitors such as semiconductor varactors [39, 40, 50–52], MEMS [53, 54], switches [55] or p-i-n diodes [41, 56] are commonly used. The main drawback of these techniques is the poor performance at high frequencies due to the parasitic effects which limits the operation frequency to about 7 GHz.

Mechanical tuning, on the other hand, consists on physically modifying the geometry or size of the unit cell or the distance between consecutive elements in real time. In order to do so different mechanisms can be utilized such as tilting [57] or moving [58] the conductive components of the circuit. These techniques influence the coupling between the elements within the unit cell shifting the resonant frequency as a result. In [59], stretching the substrate leads to a further separation between elements, which also shifts the resonance frequency. The main disadvantage of this technique is inherent to the method itself, since geometrical tuning has to be done mechanically, which is difficult to design and, more importantly, to implement.

A further manner to achieve tunable metamaterials is through material tuning. Material tuning is based on the use of substrates where the conductivity, permeability or permittivity along the unit cell can be controlled. Conductivity can be controlled by incorporating, for instance, a semiconductor material layer to the structure and applying voltage [60] or thermal variation [61]. The usage of ferrites at microwave frequencies allows variation of the permeability but this is not a practical solution due to the lack of linearity [62].

Permittivity tuning can be achieved utilizing tunable dielectric materials. Two tunable dielectric materials which are widely used are  $\text{Ba}_{0.5}\text{Sr}_{0.5}\text{TiO}_3$  (BST) ferroelectric films and liquid crystal (LC). Using these type of tunable dielectrics influences the phase shift per unit cell and consequently the frequency response of the metamaterial structure. In the case of BST, the tuning

is achieved by applying a variable voltage, such in [63, 64]. Although BST shows a good performance at microwave frequencies, it is particularly well suited for planar applications due to its film-like structure and can be easily doped in order to meet specific requirements. The high losses at high frequencies together with the high biasing voltage and its sensitivity to temperature are its main limitations.

Another possibility for higher operation frequencies is the usage of liquid crystal (LC) at its nematic phase as a continuously tunable anisotropic dielectric [42]. In the nematic phase, the effective permittivity of LC can be easily varied in several manners, like applying a bias voltage or a magnet induced magnetic field, for example. A further advantage of LC is the possibility of using it not only for the RF spectrum but also for higher frequencies, even up to 4 THz [65], since the performance of LC increases with frequency [66]. Its liquid nature enables the further possibility of using it not only for planar structures but also for two-dimensional and three dimensional [67] structures since it can flow and occupy any arbitrarily shaped fixed volume or cavity.

Being a continuously tunable dielectric and showing low losses for frequencies above 10 GHz makes liquid crystal the most suitable mean to achieve tunability at the Ka-Band, where the LWA presented in this thesis is intended to function. For this reason, liquid crystal is chosen in this work as the dielectric material to develop a tunable metamaterial based LWA.

### 2.2.2 *Tuning of Nematic Liquid Crystal*

In order to take advantage of liquid crystal continuous tunability capabilities, the director vector  $\vec{n}$  of the liquid crystal molecules has to be controlled. As depicted in Fig. 2.9, the effective permittivity that a RF electric field  $\vec{E}_{RF}$  encounters when it propagates through LC depends on the angle between the  $\vec{E}_{RF}$  and the director vector  $\vec{n}$  [24, 68]. The tuning of LC, therefore, consists of the variation of the direction of the director vector  $\vec{n}$  to achieve the desired effective permittivity. For this purpose, different techniques can be employed to align the LC molecules, and thus switch between the desired effective permittivities.

**Surface Pre-alignment:** It is possible to pre-align the liquid crystal molecules director vector  $\vec{n}$  in a defined direction by using a treated polyimide thin film [69, 70]. To do so, the polyimide is spin coated and baked on the desired surface. Once the alignment layer is cured, the film is rubbed with a velvet

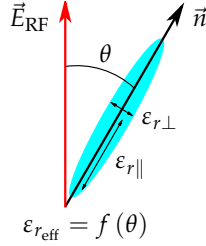


Figure 2.9: Definition of  $\epsilon_{\text{eff}}$  as a function of  $\theta$  for the LC at the nematic phase.

cloth in order to create the grooves that will anchor the LC molecules in the vicinity [71]. As a result, the major axis of the molecules close to the polyimide layer is oriented parallel to the grooves and rubbing direction. A depiction of the grooves in the polyimide layer can be seen in Fig. 2.10. In this case, the grooves and, therefore, the director vector  $\vec{n}$  of the LC molecules follow the  $x$  direction. The polyimide layer has a thickness of few nanometers since a thicker layer could affect the RF performance of the device [72]. The mechanical alignment remains fixed once it is performed on the structure. This implies it has to be used in combination with magnetic or electrical alignment in order to achieve tunability.

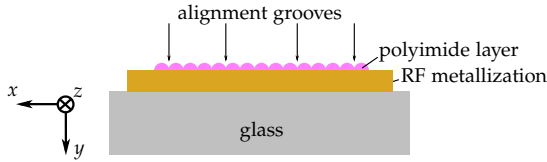


Figure 2.10: Mechanical alignment of the LC molecules.

**Magnetic Alignment:** Application of a static magnetic field aligns the director vector  $\vec{n}$  of the LC molecules parallel to the magnetic field lines. This type of alignment is accomplished in this work by the usage of rare earth magnets. As depicted in Fig. 2.11 the magnetic field lines go through the cavity where the LC is contained and enforce the alignment of the molecules. This technique is used and further investigated section 5.1.1 of this work.

**Electric Alignment** This technique, represented in Fig. 2.12, is based on the application of a static or low frequency electric field that forces the LC molecules director vector  $\vec{n}$  to align parallel to the low frequency electric

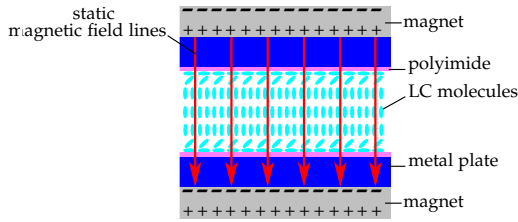


Figure 2.11: Magnetic alignment of the LC molecules.

field lines. As with the previous method, this technique is also investigated in detail in this work and a detailed description regarding this is provided in section 5.1.2.

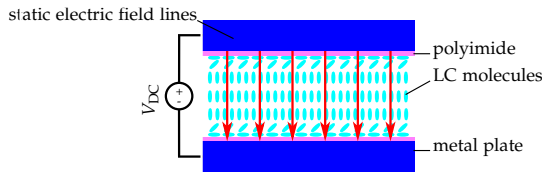


Figure 2.12: Electric alignment of the LC molecules.

Electric and magnetic alignment techniques are both based on the utilization of an external static field. In real applications, the mechanical and static field methods are combined to obtain continuous tunability.

In absence of an electric or magnetic static field, the mechanical alignment layer anchors the molecules in its vicinity parallel to the grooves direction. The interaction between molecules forces those molecules at a further distance from the polyimide layer to follow the orientation imposed by the mechanical alignment. This effect is shown in Fig. 2.13. In this state, it is considered that the overall average effective permittivity of the LC is the perpendicular permittivity  $\epsilon_{r_{\text{eff}}} = \epsilon_{r_{\perp}}$ .

When a static field is applied, as in Fig. 2.14, the molecules are subject to two forces in opposite directions, this is, the anchoring force of the polyimide layer and the static field. If the static field force is greater than the anchoring one, the majority of the molecules in the LC will gradually rotate. Despite the molecules in the center of the LC follow the static field lines, those closer to the alignment layer remain parallel to the electrodes leading to an overall

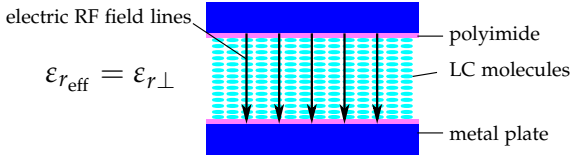


Figure 2.13: LC molecules oriented perpendicular to the propagating electric RF field lines.

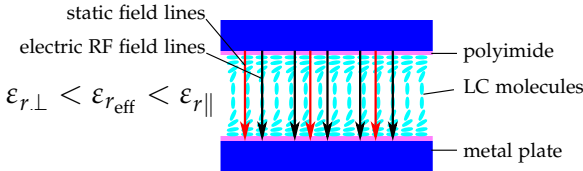


Figure 2.14: LC molecules intermediate orientation.

average permittivity  $\epsilon_{r_{\perp}} < \epsilon_{r_{\text{eff}}} < \epsilon_{r_{\parallel}}$ . When the intensity of the static field is strong enough to overcome the mechanical forces induced by the polyimide layer, all molecules, except those close to the polyimide alignment layer, align parallel to the static field lines [24]. Consequently, the liquid crystal shows a parallel permittivity  $\epsilon_{r_{\parallel}}$ , which is shown in Fig. 2.15.

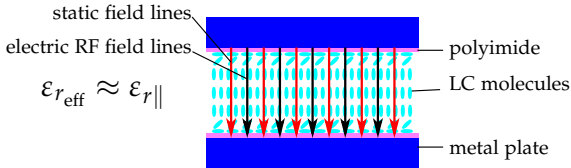


Figure 2.15: LC molecules oriented parallel to the propagating electric RF field lines.

For this work, liquid crystal material TUD-649 from Merck KGaA is used. This is an experimental mixture, with  $\epsilon_{r_{\perp}} = 2.43$  and  $\tan \delta_{\perp} = 0.0066$  and  $\epsilon_{r_{\parallel}} = 3.22$  and  $\tan \delta_{\parallel} = 0.0016$  at 30 GHz. The material tunability of the LC is defined regarding the maximum relative permittivity of the mixture as

$$\tau_{LC} = \frac{\epsilon_{r_{\parallel}} - \epsilon_{r_{\perp}}}{\epsilon_{r_{\parallel}}} = 24.5\%. \tag{2.24}$$

## 2.3 EXTRACTION METHODS

As introduced in section 2.1, the phase shift  $\beta l$  per unit cell and impedance  $Z_c$  along frequency are the only information required to determine the dispersion characteristic of a CRLH transmission line. Since such an artificial transmission line is used in this work for the design of the leaky wave antenna, obtaining  $\beta l$  and  $Z_c$  is necessary for the design of the radiation properties of the antenna. In general, artificial structures based on the periodical repetition of a unit cell usually present many discontinuities as a result of such periodicity. At each one of these discontinuities there is the possibility that the propagating wave excites higher order modes, whose energy might be added to that of the propagating wave. It is, therefore, essential to take into account the effect of the higher order modes to obtain accurate simulation results. Considering this, there are several methods to extract  $\beta l$  and  $Z_c$  by means of full-wave simulation such as the Scattering Parameters Matrix or the Eigenmode simulation.

### 2.3.1 *Complex Scattering Parameters Matrix*

In this work, the extraction of the phase shift  $\beta l$  per unit cell and the characteristic impedance  $Z_c$  of the considered CRLH metamaterial transmission line is based on the Complex Scattering Parameters Matrix. This matrix is obtained directly as a result of a full-wave simulation along frequency. Moreover, this method is also applied on the measured scattering parameters to extract the measured phase shift and impedance, enabling the characterization of the dispersion properties of the manufactured leaky wave antenna.

The matrix is used as input information in the Nicholson-Ross-Weir Algorithm (NRW) [73] and both the phase shift and the impedance are obtained directly from it. The NRW approach implies normal propagation of the wave inside the material, i.e. no oblique incidence on the unit cell, and offers a broadband description of the medium dispersive properties [74].

Since it is based on the scattering parameters, the losses can be included in the final results, which is advantageous. The main disadvantage is that when the number of higher order modes excited in the structure is very high, the accuracy of the delivered results strongly depends on the number of simulated unit cells. This could be overcome by simulating as many unit cells as possible but has the drawback that the simulation time and computational

Table 2.1: Advantages and disadvantages of the Eigenmode solver and the Complex Scattering Parameters Matrix extraction methods.

Eigenmode solver	S-Parameters matrix
– Only $\beta l$ is extracted	+ $\gamma l$ and $Z_c$ are extracted
– Lossless simulation	+ Losses simulation possible
+ Higher order modes simulation	– Higher order modes neglected
+ Infinite periodicity in propagation direction	+ Broadband description of dispersive properties

cost increase linearly with the number of unit cells. For this reason, an optimal solution between the number of unit cells and the simulation time that provides accurate enough results has to be found.

### 2.3.2 Eigenmode Analysis

The Eigenmode solver takes into account the effect of a high number of higher order modes at the simulated structure discontinuities. Furthermore, it also considers the unit cell as infinitely periodical in the propagation direction, avoiding the effect of the first and last elements.

The main advantage of this approach is that, by just simulating one unit cell, the overall effect of the higher order modes is obtained. Nevertheless, this type of simulation presents several drawbacks. First, it only delivers information about the phase shift per unit cell. This means that the  $Z_c$  has to be calculated separately, which can be done employing field averaging techniques [75–78]. However, there is no general way to define the impedance in a three dimensional scenario, and the different approaches lead to different results. A further drawback of the eigenmode solver is the fact that losses are not taken into account. This means it is not possible to obtain any information about the metallic, dielectric and, more important, the radiation losses since open boundaries are not supported.

A comparison between both methods is shown in Table 2.1, where the explained advantages and disadvantages of each method are compared.

# 3

---

## METAMATERIAL BASED LEAKY WAVE ANTENNAS

---

Leaky wave antennas (LWAs) have been widely investigated in the last years due to their unique characteristics, such as narrow and directive beams as well as an inherent simple feeding network. They belong to the category referred to as traveling wave antennas, which are based on a waveguiding structure with some kind of mechanism to leak power along its length and thus radiate [79].

The difference between a structure acting as a leaky wave antenna or a mere waveguide is closely related to the relation between  $\beta$  and  $\beta_0$ . If  $|\beta| > \beta_0$ , the wave will propagate along the structure whereas the wave will be radiated when  $|\beta| < \beta_0$ . The limit between these two situations is when  $|\beta| = \beta_0$  which corresponds to the backfire and enfire directions, where the LWA starts radiating [79].

The radiation angle of a LWA with respect to broadside direction, this is, perpendicular to the waveguiding structure axis, is determined by [80]

$$\psi = \sin^{-1} \left[ \frac{\beta(f)}{\beta_0(f)} \right] \quad (3.1)$$

where  $\beta_0$  is the free space phase constant and  $\psi$  is defined as the angle of the maximum of the beam with respect to the broadside direction  $y$ , as shown in Fig. 3.1.

The direct dependance of the radiation angle  $\psi$  on the phase constant  $\beta$  implies that it is possible to achieve beam scanning by simply varying the phase constant of the propagating wave.

Due to the dispersion characteristic of the phase constant  $\beta$  several manners to achieve beam scanning are possible. Most commonly, this is done by

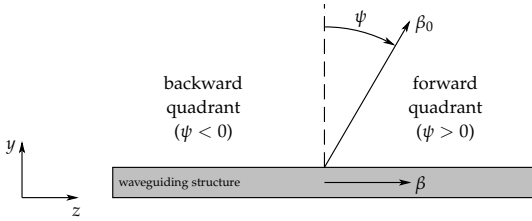


Figure 3.1: Working principle of a leaky wave antenna.

frequency tuning, since a variation in frequency provokes, automatically, a change in  $\beta$ . However, it is often desirable for many applications to perform beam steering at a fixed frequency. This can be realized by using tunable components or tunable materials.

The possibility of controlling the radiation angle by varying the phase constant, together with the high directivity and simple feeding network typical of these kind of antennas, make leaky wave antennas the most suitable type of antenna for the development of the continuously tunable antenna at the Ka-Band aimed in this work.

### 3.1 TRADITIONAL LEAKY WAVE ANTENNAS

Leaky wave antennas are divided into uniform and periodic depending on their geometry, radiation and dominant mode characteristics.

Uniform antennas present a constant cross section all along the antenna length. Their traveling wave is fast, which means the phase velocity  $v_{ph}$  of the propagating wave is greater than the velocity of light  $c_0$ . If an aperture is made in a fast wave guiding structure, the energy will be instantly radiated to the exterior as it propagates.

The first uniform LWAs date from the middle 1960s [81, 82] and are mostly based on a rectangular waveguide, filled with either air or a dielectric with a longitudinal slot, or a non-radiative dielectric waveguide (NRD).

A rectangular waveguide with a longitudinal opening is shown in Fig. 3.2. The opening can be placed at anywhere on the guiding structure, such as the side as shown in 3.2a or the top as in 3.2b.

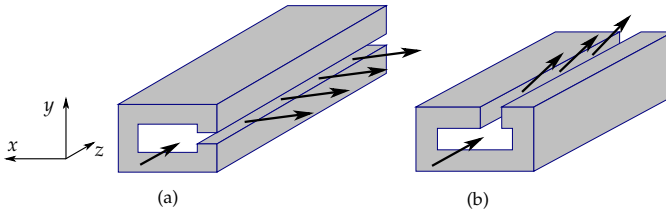


Figure 3.2: Rectangular waveguide based leaky wave antennas.

The NRD, shown in Fig. 3.3, is made up of two long parallel metallic plates separated by less than half the wavelength in a vacuum by a rectangular dielectric. The NRD will only act as a LWA if the dielectric is placed asymmetrically in the cross section, since this asymmetry transforms the confined mode into a leaky mode [83–85].

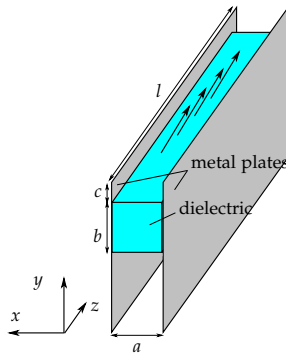


Figure 3.3: Leaky wave antenna based on a non-radiative dielectric waveguide.

Periodic LWAs, on the contrary, present a periodic modulation of the geometry. Each periodic modulation is seen as a discontinuity from the wave and produces a wave formed by an infinite number of spatial harmonics, the so called Floquet modes [86]. These spatial harmonics can be either slow, when its phase velocity  $v_{ph}$  is lower than the light velocity  $c_0$ , or fast. In opposition to fast harmonics, slow harmonics propagate along the guiding structure but can't be radiated. For this reason, periodic LWAs are designed to work

at a fast harmonic that produces radiation, usually  $n = -1$  since only the propagation of one mode is desired [87].

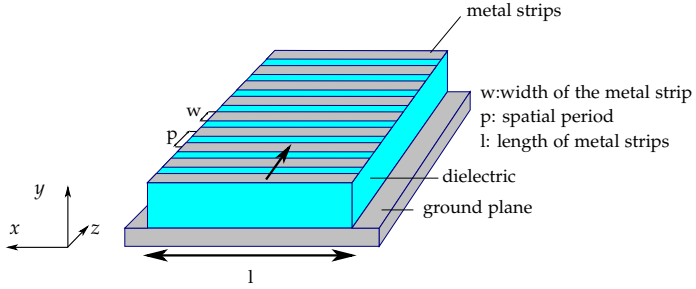


Figure 3.4: Classical 1D periodic leaky wave antenna.

Other significant parameters, such as beamwidth, scan angle behavior or radiation pattern, can be defined in a general form for both types of LWAs.

The beamwidth of the main lobe is defined as

$$\Delta\psi = \frac{1}{(L/\lambda_0) \cos(\psi)} \tag{3.2}$$

where  $L$  is the physical length of the antenna for the periodical LWA or the length of the effective aperture if a uniform LWA is considered [79].

The amount of power that is radiated per unit length is represented by the leakage constant  $\alpha_{\text{leak}}$ . If the leakage constant is large, then most of the power is radiated at the start of the opening. Consequently, the LWA has a small effective aperture which leads to a wide beam. In the case that the leakage constant is small, then the power of the traveling wave reaches the end of the opening which means the antenna has a large effective aperture leading to narrow beamwidth and higher gain and directivity. As a result, it is considered that the leakage constant  $\alpha_{\text{leak}}$  is responsible for the LWA beamwidth.

Traditionally, LWAs aim to radiate about 90% of the power injected, the remaining 10% of the power being absorbed by the load impedance matched at the end of the antenna. In this case, the relation between the electric length of

the antenna  $L$ , i.e. the effective aperture, and the leakage factor per unit length  $\alpha_{\text{leak}}$ . is [45, 79]

$$\frac{L}{\lambda_0} \approx \frac{0.18}{\alpha_{\text{leak}}/k_0}. \quad (3.3)$$

In a metamaterial based LWA is extremely difficult to calculate the needed leakage factor  $\alpha_{\text{leak}}$  to achieve 90% of radiated power, since the radiation of a single unit cell is neglectable. Instead, a high number of unit cells is necessary to form a radiating structure.

Some very directive LWA present a ratio of  $\alpha_{\text{leak}}/k_0 = 0.02$ , which leads to an effective antenna aperture of  $L/\lambda_0 \approx 9$ . This antenna aperture is much longer, in terms of  $\lambda$ , than a usual resonant antennas which is what makes LWA so directive in comparison [45].

From equations (3.1), (3.2), and (3.3) it can be derived that the beam angle is determined by the phase constant of the leaky wave along frequency whereas the beamwidth is mostly influenced by the total length of the LWA or the field distribution at the aperture. In other words, the length of the effective aperture and the leakage constant are dependent on each other and, in turn, have a direct impact on the directivity of the LWA.

The radiation pattern of LWAs is, as in every antenna, the Fourier transformation of the field distribution at the antenna aperture. The finite length of the antenna provokes the appearance of sidelobes [88]. Although LWAs usually present a poor sidelobe level, this can be improved in several manners such tapering the opening and, hence, the aperture distribution in uniform LWAs, or increasing the length of the effective aperture of the antenna in general.

Leaky wave antennas, like traveling wave antennas in general, have a characteristic far field pattern with a wide fan-like form in the direction transverse to the propagation direction and a narrow pencil beam in the propagation direction [89]. This is due to the fact that the aperture on the propagation direction is normally very long whereas in the transverse direction it is very short. If a 2D beam scanning leaky wave antenna is desired, it is possible to achieve a narrow and directive beam in both directions by placing several 1D leaky wave antennas in parallel [45].

Fig. 3.5 shows the directivity along the observation angle  $\theta$  of a general leaky wave antenna depending on the number of unit cells. The higher the number of unit cells, the lower is the half power beamwidth (HPBW), leading to a narrower and more directive main lobe. It can also be observed how increasing

the number of unit cell also improves the side lobe level without affecting the radiation angle  $\psi$ .

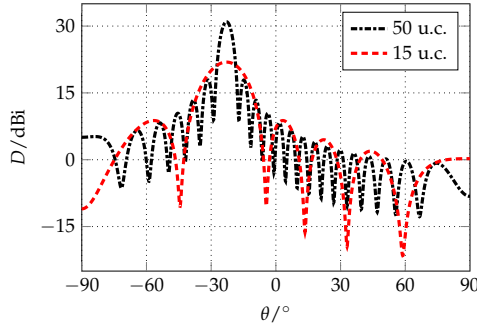


Figure 3.5: Farfield pattern of a LWA for different number of unit cells.

### 3.2 METAMATERIAL BASED LEAKY WAVE ANTENNAS

Metamaterial leaky wave antennas are a special case among leaky wave antennas. Although being based in the periodical repetition of a metamaterial unit cell, many authors consider these kind of antennas quasi-uniform since the size of the unit cell  $l$ , is much smaller than the wavelength  $\lambda_0$  and the radiated mode is also the dominant mode of the antenna [10]. Others consider them a special type of periodic leaky wave antennas due to the fact that they enable beam scanning from the backward to the forward quadrant [87, 90], which is a feature traditional uniform LWAs lack. In this work, since a continuous beam scanning from the backward to the forward quadrant is aimed, the presented LWA is considered as periodic.

This type of LWA have been widely investigated in the past years, since they unite the main advantages of leaky wave antennas, such as narrow and directive beams as well as an inherently simple feeding network, with those of metamaterial based periodic structures, which can be designed as planar structures resulting in a reduced unit cell size and low profile [10, 22, 23, 38].

The most significant advantage of an LWA consisting of a periodically repeated CRLH unit cell regarding traditional LWAs is that they provide continuous radiation from backfire to endfire, including the broadside direction [5]. According to equation 3.1, the maximum of the radiation beam points to the

broadside direction, this is  $\psi = 0$ , when the phase constant of the propagating signal  $\beta$  equals zero. For the CRLH unit cell, this corresponds to the frequency point between the LHB and the RHB. At this single point,  $\beta$  equals zero but the group velocity, which is represented by the slope of the phase shift curve, is  $v_g > 0$  as shown in section 2.1.2.

Therefore, the combination of both leaky wave antenna working principles and metamaterials is the most suitable and advantageous solution for the antenna aimed in this work.



# 4

---

## TUNABLE METAMATERIAL UNIT CELL DESIGN AND IMPLEMENTATION

---

For the design and implementation of voltage tunable leaky wave antennas at the Ka-Band, as aimed in this work, the metamaterial CRLH unit cell introduced in chapter 2 is well suited due to its dispersion characteristic.

The CRLH unit cell shows a phase shift per unit cell  $\beta l$  that can be controlled at discretion by designing the distributed lumped elements that form up the unit cell. The design of the phase shift, permits to control the radiation angle of the antenna, as shown in chapter 3, equation (3.1).

To achieve a voltage tunable LWA voltage tunable elements have to be introduced. For this purpose, liquid crystal varactors are incorporated to the unit cell. To tune the relative permittivity of these varactors and achieve, therefore, tunability a biasing network that distributes the tuning voltage along the periodic antenna is required. This, however, implies that structural modifications have to be introduced in the unit cell layout. How these modifications are carried out will be explained in detail in this chapter.

The balanced CRLH unit cell configuration offers the further advantage that, for the frequency value where  $\beta = 0$ , the group velocity  $v_g$  is greater than zero. This unique characteristic enables that the LWA radiates in the broad-side direction.

In this chapter, the design, implementation and performance of the CRLH unit cell used to form the aimed LWA are presented. The dispersion characteristics of the unit cell, the tuning capability, the effect of the manufacturing tolerances, and the losses are analyzed in detail.

#### 4.1 DISPERSION ENGINEERING OF THE UNIT CELL AND WORKING PRINCIPLE OF THE LEAKY WAVE ANTENNA

There exist several types of metamaterial unit cells that can be tunable by means of traditional tunable dielectrics such as liquid crystal or BST. Nevertheless, the choice of an appropriate unit cell configuration has to be done regarding the purpose of the application. In this work, the goal is to use the right- and left-handed propagation bands characteristic of metamaterial structures to achieve radiation both on the backward and forward quadrants.

Several metamaterial unit cell configurations can be designed to obtain this combination of LHB and RHB, such as the double serial line (DS), the double parallel line (DP), the dual composite right-/left-handed (D-CRLH), and the CRLH.

Fig. 4.1 shows the DS unit cell circuit, where all reactive elements in the series and shunt branches are positioned in series.

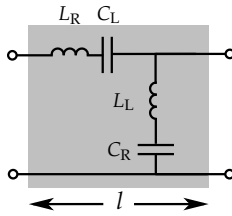


Figure 4.1: Equivalent circuit of the DS unit cell.

This configuration produces a propagation band that can be either right-handed or left-handed depending on the values of  $\omega_{se}$  and  $\omega_{sh}$ , which are determined by the lumped elements that conform the unit cell. These two possible propagation bands are shown in Fig. 4.2. As shown in Fig. 4.3,  $\text{Re}\{Z_c\}$  is greater than zero only in the propagation band and limited by two zeros independently of if the propagation band is a RHB or a LHB.

The circuit of the DP configuration is shown in Fig. 4.4. In this case, all reactive elements of both the series and shunt branches are positioned in parallel.

Similarly, to the DS configuration, the DP shows either a RHB or a LHB, which is defined by the values of  $\omega_{se}$  and  $\omega_{sh}$  regarding the circuit element.

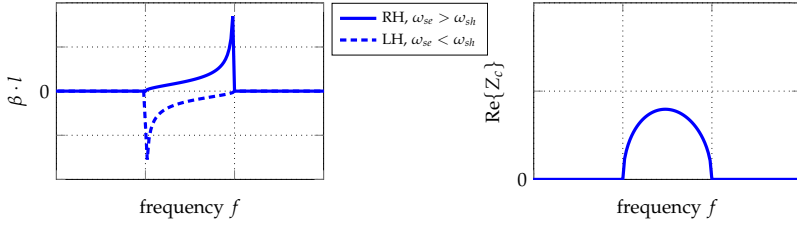


Figure 4.2: Dispersion characteristic of the DS line.

Figure 4.3:  $\text{Re}\{Z_c\}$  of the DS line.

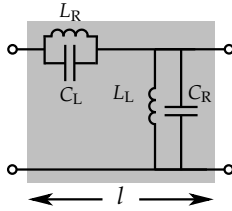


Figure 4.4: Equivalent circuit of the DP unit cell.

This can be seen in Fig. 4.5. Fig. 4.6 shows the real part of the characteristic impedance of the DP configuration. In this case, and opposite to the DS,  $\text{Re}\{Z_c\}$  is delimited by two poles.

Although DS and DP unit cell configurations show both LH and RH propagation bands, it is not possible to have both bands simultaneously. This adds the difficulty of, in order to obtain the desired tunability effect, not only tuning  $\beta$  relatively to the frequency but also the values of  $\omega_{se}$  and  $\omega_{sh}$  with respect to each other. This is, if in one tuning state  $\omega_{se} > \omega_{sh}$  then  $\omega_{sh} > \omega_{se}$  has to be achieved for the other tuning state.

The D-CRLH configuration circuit is shown in Fig. 4.7. In this unit cell, opposite to the CRLH, the elements of the series branch are positioned in parallel whereas the elements of the shunt branch are placed in series.

The D-CRLH configuration produces an LH and an RH propagation band simultaneously. This is advantageous over the DS and DP configurations

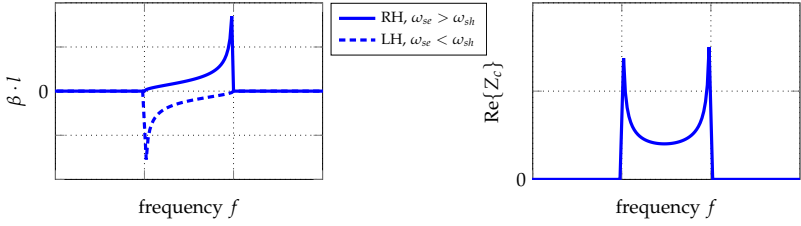


Figure 4.5: Dispersion characteristic of the DP line.

Figure 4.6:  $\text{Re}\{Z_c\}$  of the DP line.

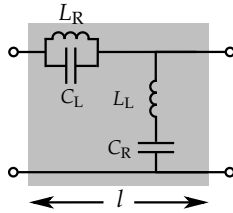


Figure 4.7: Equivalent circuit of the D-CRLH unit cell.

which can only produce one of these bands. In Fig. 4.8 both propagation bands, separated by poles at  $\omega_{se}$  and  $\omega_{sh}$ , are presented. Fig. 4.9 shows the  $\text{Re}\{Z_c\}$ , which is only greater than zero within the propagation bands, as expected.

The DS, DP, and D-CRLH unit cell configurations can be designed to present the desired dispersion characteristics and tunability capabilities. Nevertheless, they all present an important drawback when compared to the CRLH unit cell. For the DS and DP unit cell configurations, when  $\beta$  equals zero in the balanced case the group velocity  $v_g$  (2.22), represented by the slope of  $\beta$ , equals zero as well. This leads to no radiation in the broadside direction. The drawback of the D-CRLH unit cell configuration is that no continuous beam scanning from backward to forward quadrant can be carried out. With this  $\beta l$  configuration and applying equation (3.1), the antenna starts radiating at broadside in the LHB. As  $\beta l$  increases, the radiation angle  $\psi$  increases too within the forward quadrant. The scanning continues until the endfire is

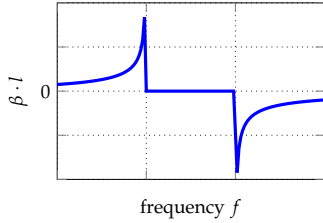


Figure 4.8: Dispersion characteristic of the D-CRLH.

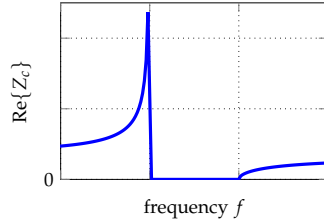


Figure 4.9:  $\text{Re}\{Z_c\}$  of the D-CRLH.

reached or  $\beta > \beta_0$ . The radiation corresponding with the LHB starts again at backfire direction approaching broadside direction for higher frequencies.

The CRLH unit cell configuration, on the contrary, shows a positive  $v_g$  between the LH and RH propagation bands for the balanced case (section 2.1.2), which makes it the most suitable configuration among all analyzed for the design of the LWA.

*Working Principle of the LWA Based on the CRLH Dispersion Properties.*

Fig. 4.10 shows the dispersion properties of the CRLH unit cell that are used for the LWA working principle. By means of liquid crystal based varactors, the dispersion characteristic of the unit cell is shifted in frequency between the unbiased and biased state. At the operating frequency  $f_0$  it is possible to continuously vary the phase shift per unit cell  $\beta l$  from its value in the unbiased state  $\beta_{\min} l$  to that corresponding to the biased state  $\beta_{\max} l$ . This shift in  $\beta l$  occurs automatically when the tuning technique chosen for the reorientation of the LC molecules is applied. Since  $\beta_{\min} < 0$  and  $\beta_{\max} > 0$ , the shift in  $\beta l$  corresponds to a beam scanning from

$$\psi_{\min} = \sin^{-1}(\beta_{\min}/\beta_0) < 0 \quad (4.1)$$

in the backward quadrant, to

$$\psi_{\max} = \sin^{-1}(\beta_{\max}/\beta_0) > 0 \quad (4.2)$$

in the forward quadrant, including the broadside direction where  $\beta l = 0$  and, hence  $\psi = 0$ .

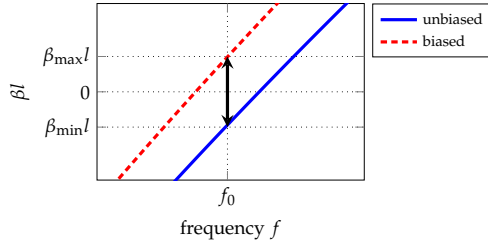


Figure 4.10: Tuning of the CRLH unit cell phase shift used as working principle of the continuously tunable LWA at a fixed frequency.

#### 4.2 IMPLEMENTATION OF THE UNIT CELL

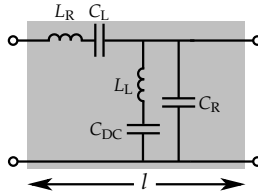


Figure 4.11: Equivalent circuit of the proposed CRLH unit cell.

The equivalent circuit of the proposed CRLH unit cell is presented in Fig. 4.11. The regular CRLH unit cell is modified by the addition of an extra capacitance  $C_{DC}$  in the series branch. To make the unit cell tunable by means of voltage biasing, it is necessary to add a DC blocking capacitor  $C_{DC}$  to the shunt branch for future electric biasing purposes. As explained in section 2.2.2, in this work both magnetic and electric alignment techniques are used to tune the LC permittivity. In order to be able to compare both techniques, the same unit cell is used in both cases. Hence,  $C_{DC}$  is incorporated as part of the unit cell, independently of the used alignment technique, in order to study its effect on the overall performance of the structure.

As shown in Fig. 4.12, when a DC biasing voltage  $V_{DC}$  is applied to a regular CRLH unit cell,  $I_{DC}$  on the shunt branch flows through the inductance, provoking a DC shortcircuit and thus preventing the tuning of the shunt capacitance. If a blocking capacitor  $C_{DC}$  is inserted in the shunt branch the DC shortcircuit is prevented and the shunt main capacitor  $C_R$  can be tuned.

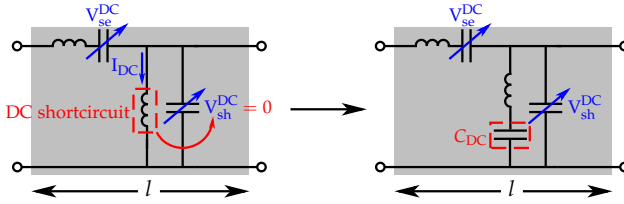


Figure 4.12: Electrical biasing scheme of the CRLH unit cell.

Despite the presence of  $C_{DC}$  in the unit cell, it is desired that this behaves as a pure CRLH. It is, therefore, necessary to specifically design the blocking capacitor so its effect on the CRLH dispersion characteristic of the unit cell is as small as possible.

As a result of the presence of  $C_{DC}$ , an additional stopband is created below

$$\omega_0 = \frac{1}{\sqrt{C_{DC}L_L}}. \quad (4.3)$$

Because  $C_{DC}$  has also an impact on the shunt branch resonance frequency  $\omega_{sh}$ , its value has to be as large as possible in order to shift its stopband out of the frequency range of operation and thereby make its effect negligible. This is

$$\omega_{sh} = \sqrt{\frac{1}{C_{DC}L_L} + \frac{1}{C_R L_L}} \approx \frac{1}{\sqrt{C_R L_L}} \quad (4.4)$$

for large values of  $C_{DC}$ , which makes the presented unit cell work as a conventional CRLH structure at the frequency range of operation.

To achieve a high capacitance value for  $C_{DC}$  while maintaining the CRLH dispersion characteristic, an interdigital capacitor (IDC) design is proposed. This shape offers more degrees of freedom for the design of  $C_{DC}$  compared to a purely parallel plate capacitor. The design steps of the interdigital  $C_{DC}$  are explained in detail in section 4.3, where the layout of the proposed unit cell is analyzed.

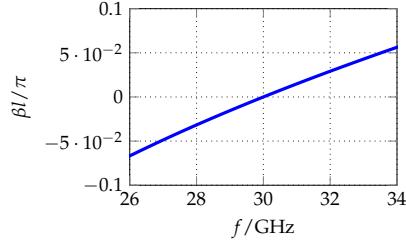


Figure 4.13: Phase shift per unit cell of the CRLH with the biasing capacitor  $C_{DC}$ .  $L_{se} = 0.056$  nH,  $C_{se} = 0.5026$  pF,  $L_{sh} = 0.11$  nH,  $C_{sh} = 0.2559$  pF,  $C_{DC} = 2$  pF.

#### 4.2.1 Circuit Simulation and Layout Implementation

If the CRLH unit cell is designed to provide a balanced dispersion characteristic with  $\beta = 0$  at 30 GHz, as shown in Fig. 4.13, the lumped elements of the unit cell shown in Fig. 4.11 take the values  $L_{se} = 0.056$  nH, and  $C_{se} = 0.5026$  pF in the series branch and  $L_{sh} = 0.11$  nH,  $C_{sh} = 0.2559$  pF, and  $C_{DC} = 2$  pF in the shunt branch.

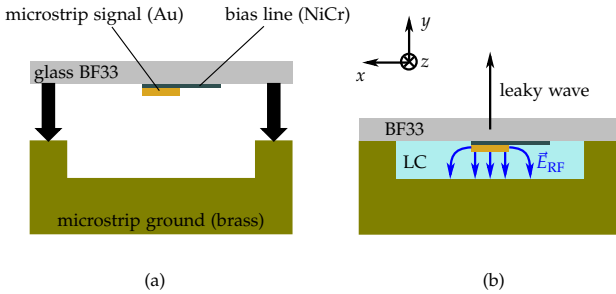


Figure 4.14: (a) BF33 substrate with radiating structure and biasing lines printed on bottom and metal block with cavity. (b) Completely mounted antenna with cavity filled with LC.

The next step is to take into account the materials that will be used to fabricate the unit cell and their characteristics at microwave frequencies. Fig. 4.14 shows a depiction of the profile of the manufactured unit cell. The RF metalization is printed on a borofloat (BF33) glass substrate with  $\epsilon_r = 4.65$ ,  $\tan \delta = 0.008$  at 30 GHz and a thickness of 700  $\mu\text{m}$ . The RF metalization

is made of gold with a thickness of  $2\ \mu\text{m}$  on the bottom side of the glass substrate. A metal block is used as ground plane. The glass substrate is glued on top of the metal block forming a  $100\ \mu\text{m}$  cavity, which is filled with LC. A detailed description of the manufacturing process and the chosen materials is given in section 4.3.

Each lumped element of the circuit configuration is progressively substituted by its equivalent component. Then the equivalent component is tailored, taking into account the technological constraints such as metalization thickness or height of the cavity to obtain the dispersion characteristic of Fig. 4.13.

First, the series branch is substituted by a transmission line section and a parallel plate capacitor. The high series frequency  $f_{se} = 30\ \text{GHz}$  forces a small value of  $L_{se}$  and  $C_{se}$ . To minimize  $L_{se}$ , the length of the unit cell has to be as small as possible. This, in turn, reduces  $C_{se}$  in excess. To significantly increase the capacitance in such a reduced length, the parallel plate capacitor is substituted by an interdigital capacitor, which allows more degrees of freedom, e.g. number of fingers, gap between fingers, and length and width of fingers, during the design process.

The lumped elements of the shunt branch,  $L_{sh}$  and  $C_{sh}$ , are substituted by a transmission line section. To obtain the designed shunt frequency  $f_{sh} = 30\ \text{GHz}$ , the length and width of the line section are optimized. This process results in an extremely long shunt branch. To obtain the same dispersion results with a reduced shunt branch length, the transmission line is meander shaped. The meandered shunt branch also allows further degrees of freedom since the length and distance between the different meander sections can be designed separately.

$C_{DC}$  is also designed as an interdigital capacitor. It is aimed that this capacitance affects as little as possible  $\omega_{sh}$ , which implies reduced length, to minimize effects on the total  $L_{sh}$ , and high capacitance value to maintain its resonance below the operating frequency range. These two requirements are satisfied by using an interdigital capacitor.

Taking into account the glass substrate BF33, the LC and gold metalization, the phase shift per unit cell shown in Fig. 4.15 is obtained. It can be observed that the dispersion characteristic is not balanced anymore since a stopband of approximately  $1\ \text{GHz}$  occurs between the LHB and RHB. Moreover, to achieve such a phase shift per unit cell, the obtained gap between the series IDC fingers equals  $7\ \mu\text{m}$ , which is far below  $17\ \mu\text{m}$ , the minimum size that can be manufactured with the available technology.

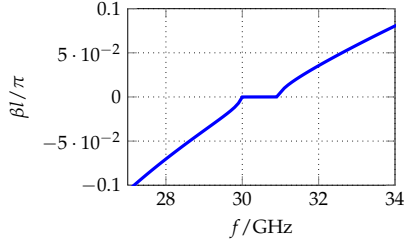


Figure 4.15: Phase shift per unit cell of the CRLH with the biasing capacitor  $C_{DC}$  obtained for from the layout analysis.

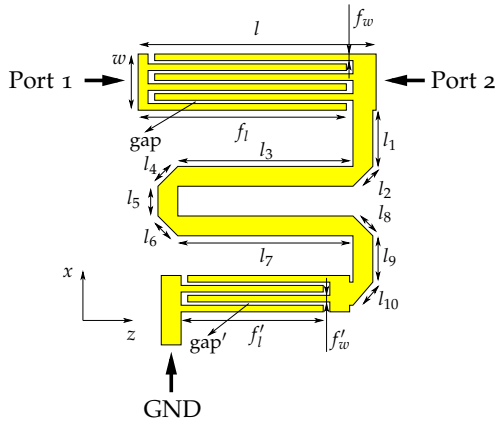


Figure 4.16: Developed unit cell layout of the modified CRLH.

If this further constraint is taken into account, the layout depicted in Fig. 4.16 is obtained for the proposed CRLH. The series branch corresponds to the main interdigital capacitor, composed of six fingers with length  $f_1 = 643 \mu\text{m}$ , width  $f_w = 21 \mu\text{m}$ , and gap =  $18 \mu\text{m}$ . The meander line represents the shunt inductance with a total length of  $l = 1900 \mu\text{m}$ . At the end of the meander line, the IDC corresponding to the DC blocking capacitor can be seen. The  $C_{DC}$  is made up of four fingers, with a finger length  $f'_1 = 340 \mu\text{m}$ , width  $f'_w = 19 \mu\text{m}$ , and gap =  $20 \mu\text{m}$ . The distributed shunt capacitance is created between the complete unit cell and the ground plane below it. All dimensions of the designed unit cell are listed in Table 4.1.

Table 4.1: Modified CRLH unit cell layout elements dimensions.

$l/\mu\text{m}$	$w/\mu\text{m}$	$f_1/\mu\text{m}$	$f_w/\mu\text{m}$	gap/ $\mu\text{m}$	$l_1 + \dots + l_{10}$
725	161	643	21	18	1.9 mm
		$f'_1/\mu\text{m}$	$f'_w/\mu\text{m}$	gap'/ $\mu\text{m}$	
		340	19	20	

Fig. 4.16 shows how  $C_{DC}$  is designed to enable contact of the shunt branch to ground. For this purpose, the left section of the IDC is extended downwards. This is the point where the unit cell contacts the metal block used as a ground plane. To ensure the electrical connection, a silver based conductive glue is used. The contact to ground is one of the most challenging steps during the manufacturing process, since an error of few  $\mu\text{m}$  in the alignment can result in a shortcircuit of the IDC that forms  $C_{DC}$  and thus the LWA. The corner sections corresponding to  $l_2$ ,  $l_4$ ,  $l_6$ ,  $l_8$ , and  $l_{10}$  are rounded in a further optimization of the unit cell in order to decrease the current losses.

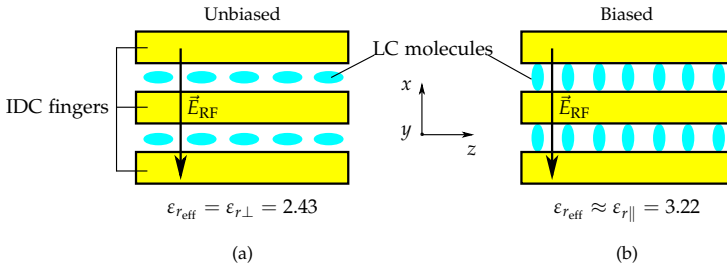


Figure 4.17: LC molecules orientation within all IDC used in this work. (a) Unbiased state. (b) Biased state.

For this unit cell and all structures presented within this work, the terms unbiased and biased describe the states where the LC molecules are oriented following the depiction in Fig. 4.17. In the unbiased state, the molecules are parallel to the IDC fingers and the effective permittivity encountered by the RF field is  $\epsilon_{r\text{eff}} = \epsilon_{r\perp} = 2.43$ . For the biased state, the molecules are oriented perpendicularly to the IDC fingers and the effective permittivity is  $\epsilon_{r\text{eff}} \approx \epsilon_{r\parallel} = 3.22$ .

### 4.2.2 Full-wave Analysis

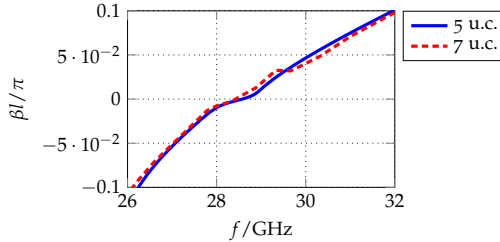


Figure 4.18: Simulated unit cell phase shift for both biased and unbiased states for seven and five unit cells.

The full-wave simulations presented in this work are carried out in Agilent Advance Desing System (ADS) simulation software. On one hand, the simulation of the complete LWA is not possible due to high computational and time costs, on the other, the simulation of just one unit cell is not accurate enough, since it neglects the effect of higher order modes that appear at the discontinuities of the unit cell. Consequently, an intermediate solution has to be found that delivers accurate results while keeping the simulation time and computational costs bearable using a state-of-the-art desktop PC.

Fig. 4.18 shows the phase shift per unit cell extracted from two full-wave simulations, one with five unit cells and the other with seven unit cells. It can be observed that both simulations deliver similar results but the dispersion curve for 7 unit cells is not as smooth as the curve for 5 unit cells. This is due to the fact that the lossless full-wave simulation for 7 unit cells is not completed and lacks thus some data points. The interruption of the lossless full-wave simulation for 7 unit cells was carried out after 25 consecutive days (600 h) of simulation. In comparison, the full-wave simulation for 5 unit cells delivers similar results and is completed after 48 h to 96 h for the lossless and lossy configurations, respectively. For this reason, henceforth the layout shown in Fig. 4.19, consisting of five unit cells, their corresponding biasing circuitry, and the ground contact to the metal block, is considered for all simulations carried on in this work regarding the presented unit cell and LWA.

Fig. 4.20 shows the phase shift per unit cell obtained by means of full-wave simulations for the unbiased and biased states. The simulations include ra-

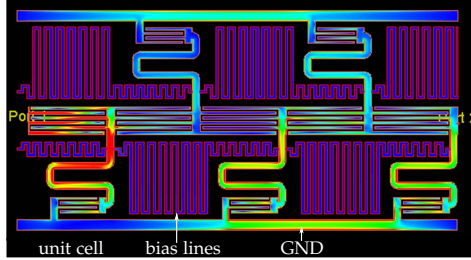


Figure 4.19: Full-wave simulated structure for the electrically biased LWA consisting of five unit cells.

diation, metallic, and dielectric losses and are extracted from the Scattering Parameters Matrix using the Ross-Weir-Method [73].

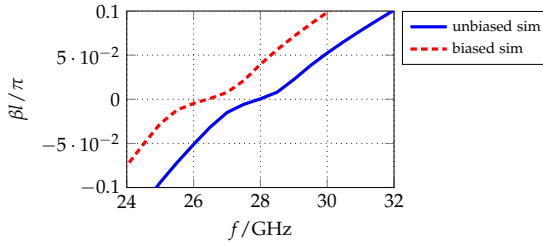


Figure 4.20: Simulated unit cell phase shift for both biased and unbiased states, including losses.

In the simulation results, a slight change in the slope of the phase shift curve can be seen around 28 GHz for the unbiased state and 26 GHz for the biased state. This is caused by the fact that  $\omega_{se}$  and  $\omega_{sh}$  are not equal and the unit cell is not balanced.

At 26.7 GHz, the phase shift per unit cell can be tuned between  $\beta l = -0.025\pi$  for the unbiased state and  $\beta l = +0.012\pi$  for the biased state. Applying Eq. (3.1), at the fixed frequency of 26.7 GHz, a minimum radiation angle of  $\psi = -11.7^\circ$  and a maximum of  $\psi = +5.34^\circ$  with respect to the broadside direction are obtained.

This implies a continuous beam scanning from the backward quadrant into the forward quadrant at a fixed Ka-Band frequency, which is the main goal of this work. For both the unbiased and biased states in the full-wave simulation,

the stopband in the dispersion characteristic almost disappears due to the losses, which also affect the slope of the curves. A detailed loss analysis is carried out in section 4.6, nevertheless the results of the full-wave simulation presented in Fig. 4.20 are the ones taken as a reference from now onwards.

The real part of the simulated impedance  $Z_B$  can be seen in Fig. 4.21. The real part of the impedance confirms that  $\omega_{se}$  and  $\omega_{sh}$  do not cancel each other out. Since the stopband is not visible anymore with  $\text{Re}\{Z_B\} = 0$ , the pole and the zero that delimit it are strongly attenuated by the losses but still recognizable.

At 26.7GHz the impedance takes a value of  $55\Omega$  for the unbiased state and  $10\Omega$  for the biased which is deviated from the initially intended  $50\Omega$  design.

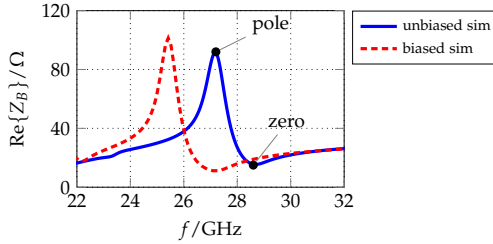


Figure 4.21: Simulated real part of the Bloch impedance  $\text{Re}\{Z_B\}$  for both biased and unbiased states.

### 4.2.3 Distributed Lumped Elements Calculation

The values of the distributed lumped elements that form the CRLH unit cell and correspond to the layout presented in Fig. 4.16 are obtained by means of analytical methods combined with circuit simulation. All obtained values are listed in Table 4.2.

Table 4.2: CRLH unit cell components and their correspondent analytical values.

	$L_{se}/\text{nH}$	$C_{se}/\text{pF}$	$L_{sh}/\text{nH}$	$C_{sh}/\text{pF}$	$C_{DC}/\text{pF}$
$\varepsilon_{r\perp} = 2.43$	0.2064	0.1507	1.3320	0.0494	0.0526
$\varepsilon_{r\parallel} = 3.22$	0.2064	0.1680	1.3320	0.0574	0.0586

For the calculation of the distributed lumped elements, the model presented in [91] is used. This model describes interdigital capacitors with multilayer substrates, which are capacitors with at least two dielectric layers, below and above the RF metalizations. In this work, these layers correspond to the glass layer above and the LC layer below the RF metalization. The overall capacitance is dependent on three minor capacitances: the capacitance of the periodical section  $C_n$ , the capacitance due to the finite width of the external fingers  $C_3$ , and the fringing capacitance of the finger ends  $C_{end}$ .

The total capacitance of the multilayered substrate with finite width fingers and finite width terminals for  $n \geq 4$  is

$$C_T = C_n + C_3 + C_{end} \quad (4.5)$$

where the series capacitance of the CRLH unit cell has a total value of  $C_{se} = 0.1507$  pF for  $\epsilon_{r_{eff}} = \epsilon_{r\perp} = 2.43$  and  $C_{se} = 0.1680$  pF for  $\epsilon_{r_{eff}} \approx \epsilon_{r\parallel} = 3.22$ , for an LC thickness of  $100 \mu\text{m}$  and a glass thickness of  $700 \mu\text{m}$ .

The detailed calculation of  $C_n$ ,  $C_3$ , and  $C_{end}$ , specifically adapted for the present unit cell, is presented in detail in A.1.  $C_{DC}$  is calculated using the same method as for  $C_{se}$ , since it is also a multilayered substrate IDC and its corresponding values for  $\epsilon_{r_{eff}} = \epsilon_{r\perp} = 2.43$  and  $\epsilon_{r_{eff}} \approx \epsilon_{r\parallel} = 3.22$  are  $0.0526$  pF and  $0.0586$  pF, respectively.

The calculation of the  $L_{sh}$ , represented by the meander line in the unit cell layout, is carried out based on [92]. For this type of inductors, not only the self inductance  $L_{self}$ , i.e. the total inductance of the conducting line, has to be taken into account but also the mutual inductance  $M_T$  resulting from the mutual coupling between the different segments of the meander, which are highly influenced by the geometry and physical characteristics of the inductive line.

$L_{sh}$  is defined as

$$L_{shT} = L_{self} + M_T. \quad (4.6)$$

The detailed calculation of both inductances is shown in A.2. As a result,  $L_{shT} = L_{self} + M_T = 0.9774$  nH +  $0.3542$  nH =  $1.332$  nH. It can be observed that the mutual coupling can not be neglected for the case of meander inductances.

To calculate the series inductance and the shunt capacitance a circuit simulation analysis is carried out using the values of  $C_{se}$ ,  $C_{DC}$ , and  $L_{sh}$  obtained

previously. Having these values fixed, the values of  $C_{sh}$  and  $L_{se}$  are tuned until the phase shift characteristic of the unit cell fits with that obtained in the full-wave simulation. The characteristic phase shift and impedance curves obtained in this process are shown in Fig. 4.22 and Fig. 4.23, respectively.

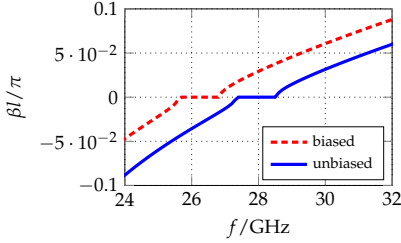


Figure 4.22: Unit cell phase shift for the unit cell values obtained by analytical calculation.

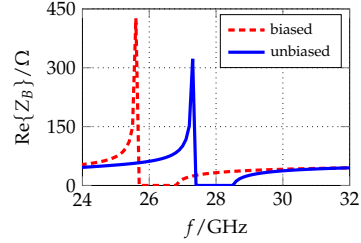


Figure 4.23: Real part of the Bloch impedance for the unit cell values obtained by analytical calculation.

If  $\beta l$  and  $\text{Re}\{Z_B\}$  obtained by the analytical calculation, shown in Figs. 4.22 and 4.23, are compared to  $\beta l$  and  $\text{Re}\{Z_B\}$  obtained by full-wave simulations, shown in Figs. 4.20 and 4.21, it can be observed that both methods deliver similar results. The difference between them is that the full-wave simulations are carried out taking into account the losses, whereas the analytical methods to calculate the distributed lumped elements do not. As a result, the stopband, which almost disappears for the full-wave simulations is clearly visible in the analytical results. This is shown in Fig. 4.24, where the phase shift per unit cell for circuit simulation, the full-wave simulation, and the analytical method are represented. The good agreement between the full-wave simulation and the analytical results makes the latter a suitable option to save simulation time when no losses need to be considered. For further investigations, where losses, higher order modes, and radiation efficiency have to be considered, full-wave simulation is the optimal solution.

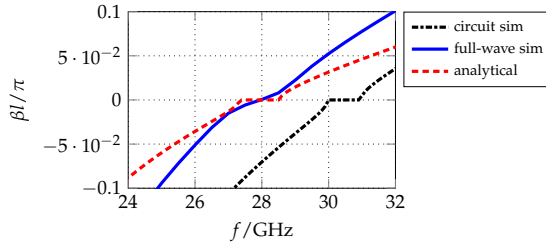


Figure 4.24: Comparison between the phase shift per unit cell for circuit simulation, analytical calculation, and full-wave analysis.

### 4.3 FABRICATION PROCESS

The lithographic manufacturing process of all microwave structures presented in this work has been carried out in a clean room environment.

A glass substrate (BF33) is chosen to structure the RF metalization on top of it. This material is specifically chosen due to its optical transparency and good performance at microwave frequencies. There are several steps along the manufacturing process that require an alignment in the order of micrometers. These alignments have to be done under a microscope and the transparency of the substrate is essential.

The glass substrate is covered by a 20 nm layer of nickel-chromium (NiCr) by means of evaporation. The NiCr layer acts as adhesion layer between the glass substrate and the gold layers and is simultaneously used to structure the resistive biasing network. Above this layer, a further 30 nm gold layer is evaporated. This gold layer serves as a seed layer for the electroplating of the RF structure.

After the evaporation, the glass substrate is covered by a 3.3  $\mu\text{m}$  thick AZ4533 photoresist layer by spin coating that is used to transfer the RF structure from the designed photo mask to the substrate by ultraviolet (UV) exposure. It is important that the photoresist forms a uniform layer, since the appearance of irregularities leads to errors in the transfer of the RF structure. Moreover, the thickness of the photoresist layer has to be constant since it is the limiting factor of the thickness of the RF metalization in later electroplating steps.

Subsequent to the UV exposure and development, the substrate is hard-backed and then immersed in a gold bath where a 2  $\mu\text{m}$  gold layer is elec-

troplated in order to form the designed RF structure. The thickness and uniformity of the obtained gold layer depend on the plating time and the applied current, respectively, i.e. the plating rate. The maximum thickness of the plated gold is thus limited by the height of photoresist.

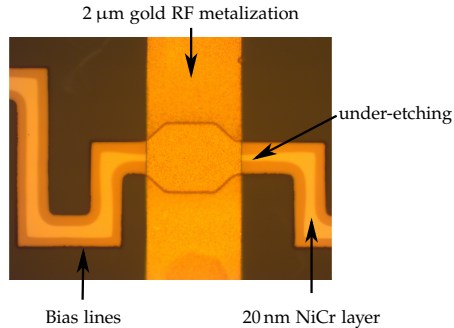


Figure 4.25: Alignment of the biasing lines and RF structure. Effect of under-etching is visible on the NiCr biasing lines.

For the case of the electrically biased LWA, the previous steps, except plating, are repeated with a photo mask for the biasing network. The biasing network has to be microscopically aligned with the RF structure. Fig. 4.25 shows the connection and designed alignment of the biasing lines with the RF structure. If alignment is not perfect, the risk of obtaining broken or defective biasing lines after the etching grows significantly. This would result in the loss of the tuning capabilities of the unit cell and hence the LWA.

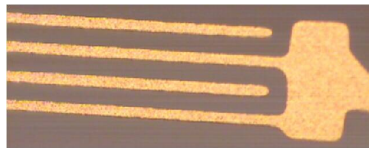


Figure 4.26: Effect of under-etching on the IDC finger. The finger width is decreased and the gap size is increased due to long etching.

Once the photoresist for the biasing network has been developed and baked, the 30 nm gold layer and 20 nm of NiCr are removed from all areas of the substrate where no structure is desired in order to reveal the biasing network and avoid short circuits. This is done by means of gold etching and subsequent chrome etching. Etching is one of the most critical steps of the whole process,

together with alignment and gluing, since its duration is highly dependent on the geometry of the structure. For the particular LWA presented in this work, a challenge lies in the fact that the size of gap between the IDC fingers is in the microscopical order whereas the complete antenna length is in the macroscopical order. The etching times in these two cases differ significantly, which increases the complexity of this process. If the fabricated structures are etched for too long, the metal layer adhering the RF metalization to the glass substrate is attacked by the etchant. Hence, the structure is under-etched, only the RF metalization on top of it will remain after the etching. If the etching time is so long that the adhering layer completely disappears, then the RF metalization separates from the glass substrate. Fig. 4.26 shows the result of under-etching on an interdigital capacitor. In this case, the gold fingers have been under-etched resulting in extremely thin fingers and bigger gap than designed.

The opposite process happens when the etching time is too short. In this case, the etchant does not remove the NiCr adherence layer from the corresponding areas and the RF elements are shortcircuited. For the specific unit cell presented here, this is critical at the gaps between the IDC fingers, since a short etching time provokes a shortcircuit between the IDC fingers, leading to a loss of the tuning capability.

Once the RF and biasing structures are completed, the surface of the glass substrate is spin coated with a polyimide film with a typical height of 10 to 100 nm. The polyimide layer is responsible for the mechanical alignment of the LC. To ensure electrical contact between the unit cell and the metal block that acts as a ground plane, the connection point between them must be free of polyimide. This is achieved by covering the line section that connects the unit cell to the ground plane before the spin coating of the polyimide. This step is carried out under a microscope. A first baking process is carried out at 90 °C for ten minutes and thereafter the temperature is increased to 120 °C for ninety minutes. Subsequently, the grooves needed for the mechanical alignment of the LC are shaped by rubbing the RF substrate with a velvet cloth. The polyimide layer anchors the LC molecules in the unbiased state parallel to the rubbing direction [68]. The working principle of this process is described in detail in 2.2.

A metal block is used as ground plane to provide mechanical stability and form the LC cavity. The glass substrate is glued with silver based conducting glue on top of the metal block forming a 100  $\mu\text{m}$  cavity between both of them. The glue is leveled to achieve a layer as thin as possible and to maintain the

LC cavity height as constant as possible along the LWA. The gluing of both LWA components is a critical step that has to be carried out under a microscope. A precise alignment is required, since the line section that connects the unit cell with the metal block is short and a misalignment could provoke a shortcircuit. Fig. 4.27 shows a microscopic photograph of the area of the unit cell where the connection to ground is made. A shortcircuit in the unit cell would also result in the loss of the tuning capabilities. A further challenge for the alignment is the liquid consistency of the glue. Not only can it spread onto the glass substrate and shortcircuit the complete unit cell but its liquid consistency makes also difficult to keep the alignment between the glass substrate and the metal block during the curing of the glue.

Finally, once the glass substrate is mounted on the metal block, the cavity is filled with LC and sealed with two-component epoxy glue. All IDCs, CRLH unit cell and LWA prototypes presented in this thesis are manufactured following this process.

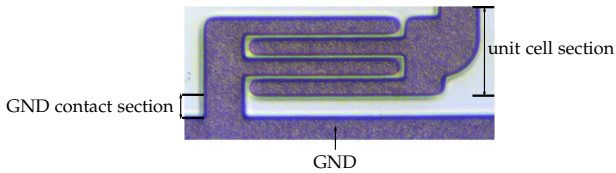


Figure 4.27: Microscopic photograph of the  $C_{DC}$  and the ground contacting line section.

#### 4.4 TUNABILITY ANALYSIS OF THE COMPOSITE RIGHT-/LEFT-HANDED UNIT CELL

During the design and implementation process of a unit cell based on a tunable material, it is of utmost importance to take into account the fact that the tunability of the material can not be directly and completely transferred to the unit cell or the complete antenna made up of these unit cells. For this reason, a detailed analysis about this transfer of the tunability from the material to the component is carried out in this section. Since a varactor is the component on which the tunability of the CRLH unit cell is based, an IDC was specifically designed, simulated and fabricated to work in the Ka-Band and its performance regarding the tunability of liquid crystal analyzed.

Table 4.3: Equivalent lumped element values for the approximated IDC model.

$\epsilon_{r,eff}$	$C_{se}/\text{pF}$
2.43	0.1379
3.22	0.1538

### The Tunable Interdigital Capacitor

The tunability of the LC material can not be completely transferred to a component, i.e. the implementation of a tunable LC based capacitor, for instance, shows smaller tunability than the LC itself. This effect has a direct impact on the tuning capabilities of structures based on these type of varactors such the LWA presented in this work.

The beam scanning capabilities of the LWA are based, among others, on the dielectric material tunability and the main components the unit cell it is made up of. The tunability of the used CRLH unit cell depends, in turn, on that of the series varactor, which, in this case, is an interdigital capacitor. In the following section, the tuning characteristics of such capacitors are analyzed in detail, since the IDC is the prior design step to the CRLH unit cell design that conforms the LWA.

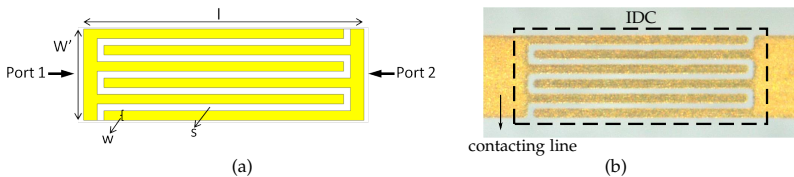


Figure 4.28: Proposed interdigital capacitor: (a) Simulated Layout (dimensions in  $\mu\text{m}$ :  $W' = 240$ ,  $l = 654$ ,  $w = 25$ ,  $s = 25$ ). (b) Fabricated prototype.

The layout, dimensions, and a microscope photograph of the manufactured IDC are presented in Fig. 4.28. The capacity of the presented IDC is calculated using the same conformal mapping method used for the CRLH unit cell [91]. The obtained  $C_{se}$  values for the unbiased and biased states are presented in Table 4.3.

Taking into consideration the values of  $C_{se}$  for the unbiased and biased states, the maximum tunability of the IDC capacitance is given by

$$\tau_{C_{IDC}} = \frac{C_{IDC} |_{Biased} - C_{IDC} |_{Unbiased}}{C_{se} |_{Unbiased}} = 11.5\%. \quad (4.7)$$

To prove the obtained analytical results, the proposed IDC is fabricated and its response in frequency measured. Fig. 4.29 shows the on-wafer measured S-parameters of the manufactured IDC.

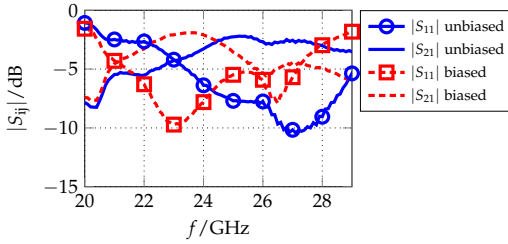


Figure 4.29: Measured scattering parameters of the manufactured IDC.

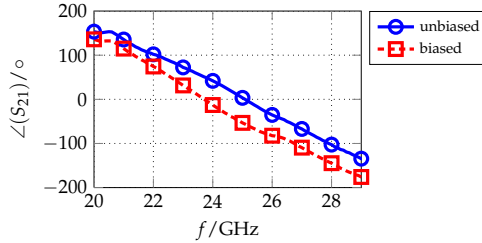


Figure 4.30: Measured transmission phase  $\angle S_{21}$  of the manufactured IDC.

The transmission band is shifted downwards in frequency when a tuning voltage of 60 V is applied. The shift in frequency due to the tuning of the capacitance of the IDC can be observed although a small resonance around 26 GHz appears due to the combination of fabrication tolerances, specially concerning the IDC finger width.

In order to verify the previously calculated capacitance tunability, the phase of the transmission  $\angle S_{21}$ , which is shown in Fig. 4.30, is used to calculate the tunability of the manufactured IDC. For a fixed phase, e.g.  $\angle S_{21} = 0$ ,

the corresponding frequencies 25.07 GHz and 23.76 GHz are obtained for the unbiased and biased states, respectively. If the capacitance tunability as a function of the frequency is now calculated as

$$\tau_{\text{IDC}} = \frac{\frac{1}{f_{\text{biased}}^2} - \frac{1}{f_{\text{unbiased}}^2}}{\frac{1}{f_{\text{unbiased}}^2}} = \frac{f_{\text{unbiased}}^2}{f_{\text{biased}}^2} - 1 = 11.33\%. \quad (4.8)$$

The measured tunability  $\tau_{\text{IDC}}$  of the manufactured IDC fits that obtained from the analytical analysis.

It can be observed that from a tunable LC material with a tunability of  $\tau_{\text{LC}} = 24.5\%$  only a tunability of  $\tau_{\text{IDC}} = 11.33\%$  is achievable for the interdigital capacitors, which implies that the the beam scanning capabilities of a LWA based on these type of varactors are limited by the tunability of the varactor itself.

#### 4.5 TOLERANCE ANALYSIS

As introduced in section 4.3, the fabrication of the structures presented in this work is a manual process susceptible, therefore, to manufacturing error. Different manufacturing steps can lead to different errors in the final prototype. For example, deficient spin coating, insufficient exposure or development time can lead to complications with gold plating, thereby influencing the RF metalization thickness. One of the most critical steps of the manufacturing process is the metal etching, which can lead to IDCs where not all fingers have the same width or gap width between them. Accordingly, a tolerance analysis of several design parameters of the unit cell is carried out in this section using analytical and circuit simulations to observe the impact of fabrication uncertainties on the performance of the unit cell.

From all parts of the unit cell, the IDCs are the most sensitive to the fabrication tolerances, which affects not only the resonance frequency of each unit cell independently and consequently the phase shift and scanning behavior of the final LWA, but has also a significant impact on the radiation characteristics and matching of the LWA.

In this section a detailed analysis is carried out about the influence on the overall performance of the antenna of the deviation of the IDC finger width

Table 4.4: Design parameters of unit cell and the maximum deviation values for each parameter.

	Designed						
	Values	$f_{w,max}, gap_{min}$	$f_{w,min}, gap_{max}$	$t_{max}$	$t_{min}$	$h_{max}$	$h_{min}$
$f_w / \mu\text{m}$	25	30	23	–	–	–	–
gap/ $\mu\text{m}$	18	15	21	–	–	–	–
$t / \mu\text{m}$	2	–	–	2.25	1.81	–	–
$h / \mu\text{m}$	100	–	–	–	–	120	80

$f_w$ , the gap between fingers, the metalization thickness  $t$ , and the LC cavity height  $h$  from the design values. For the following analysis the worst case has been considered for all parameters, i.e., when the maximum deviation from the design values affects all unit cells simultaneously. This analysis is accomplished on the main IDC of the unit cell, which is the most sensitive component of the unit cell in terms of fabrication tolerances.

Three different cases are considered for the tolerance analysis, first, when gap and  $f_w$  deviate from the standard designed values gap = 18  $\mu\text{m}$  and  $f_w = 21 \mu\text{m}$ , second, when the RF metalization thickness varies regarding the fixed  $t = 2 \mu\text{m}$ , and third, when the height of the LC cavity is bigger or smaller than  $h = 100 \mu\text{m}$ . Each of the three cases is described, in turn, for the two possible LC effective permeabilities,  $\epsilon_{r_{eff}} = \epsilon_{r_{\perp}} = 2.43$ , and  $\epsilon_{r_{eff}} = \epsilon_{r_{\parallel}} = 3.22$ .

In the first case, gap and  $f_w$  are analyzed as one since they are directly dependent from each other. Thus, when the finger width of the IDC increases, the space between the fingers decreases and vice versa. Table 4.4 shows the maximum deviation of  $f_w$ , gap,  $t$ , and  $h$  with respect to the designed values. These values have been measured on fabricated samples and averaged.

#### *Analysis of the Deviation of the Finger Width and Gap of the Interdigital Capacitor*

Table 4.5 shows the effect of  $f_w$  and gap tolerances for LC effective permittivities. For each effective permittivity, the maximum and minimum values of the parameters under analysis are listed. For each of these values, the resulting series capacitance  $C_{se}$  and its deviation error  $\epsilon_{C_{se}}$  from the designed capacitance are calculated and listed in the first and second columns. The third column shows the series resonant frequency  $f_{se}$  resulting from the new

Table 4.5: Deviation of unit cell series capacitance and frequency for the design values  $C_{se} = 0.1507$  pF and  $f_{se} = 28.54$  GHz for  $\epsilon_{r\perp} = 2.43$  and  $C_{se} = 0.1680$  pF and  $f_{se} = 27.03$  GHz for  $\epsilon_{r\perp} = 3.22$  for the worst case of  $f_w$  and gap tolerances.

$\epsilon_{r_{\text{eff}}}$	Parameter	$C_{se}$ /pF	$\epsilon_{C_{se}}$	$f_{se}$ /GHz	$\epsilon_{f_{se}}$
2.43	$f_{w_{\text{max}}}, \text{gap}_{\text{min}}$	0.1755	16.46%	26.44	-7.36%
	$f_{w_{\text{min}}}, \text{gap}_{\text{max}}$	0.1368	-9.22%	29.95	4.94%
3.22	$f_{w_{\text{max}}}, \text{gap}_{\text{min}}$	0.1980	17.86%	24.9	-7.8%
	$f_{w_{\text{min}}}, \text{gap}_{\text{max}}$	0.1525	-9.23%	28.37	4.96%

values of the series capacitance  $C_{se}$ . The fourth and last column, shows the deviation error from the series resonant frequency  $f_{se}$  regarding that of the designed unit cell.

In general, the relative deviation error of a certain parameter  $x_0$ , is calculated as

$$\epsilon_x = \frac{x - x_0}{x_0} \quad (4.9)$$

where  $x_0$  is the designed value of the parameter.

For  $\epsilon_{r_{\text{eff}}} = \epsilon_{r\perp} = 2.43$ , the total series capacitance varies between  $C_{se}^+ = 0.1755$  pF and  $C_{se}^- = 0.1368$  pF. This leads to an error in the capacitance between  $\epsilon_{C_{se}}^+ = 16.46\%$  and  $\epsilon_{C_{se}}^- = -9.22\%$ .

The series resonance frequency  $f_{se} = 28.54$  GHz is shifted for  $C_{se}^{\pm}$ , taking the values of  $f_{se}^+ = 29.95$  GHz and  $f_{se}^- = 26.44$  GHz, respectively. As a result, the relative error in frequency for the unbiased state is  $\epsilon_{f_{se}}^+ = 4.94\%$  when  $f_w$  decreases and  $gap$  increases and  $\epsilon_{f_{se}}^- = -7.36\%$  when the  $f_w$  increases and the gap decreases. The same analysis is applied for the case where the LC permittivity is  $\epsilon_{r_{\text{eff}}} = \epsilon_{r\parallel} = 3.22$ .

The effect of the tolerances on the LWA performance is analyzed by substituting the design values for the deviated ones, e.g.  $f_w$  for  $f_{w_{\text{min}}}$ , and carrying out a circuit simulation. The obtained scattering parameters are compared with those of the unit cell with the original design parameters. Moreover, the propagation constant  $\gamma l$ , and Bloch impedance  $Z_B$  are extracted and compared.

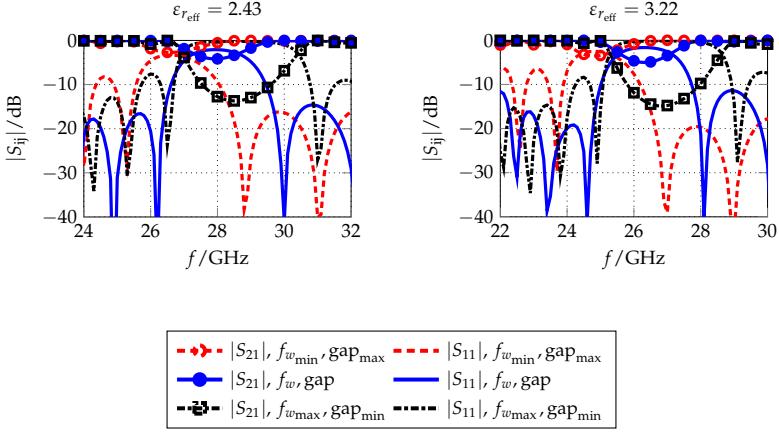


Figure 4.31: Impact of the  $f_w$  and gap tolerances on the scattering parameters for  $\epsilon_{r_{\text{eff}}} = 2.43$  (left), and  $\epsilon_{r_{\text{eff}}} = 3.22$  (right).

The tolerance effect of  $f_w$  and the gap on the LWA performance is depicted in Figs. 4.31- 4.33 for  $\epsilon_{r_{\text{eff}}} = 2.43$  and  $\epsilon_{r_{\text{eff}}} = 3.22$ .

Fig. 4.31 shows the effect on the scattering parameters when  $f_w = f_{w_{\text{max}}}$  and  $\text{gap} = \text{gap}_{\text{min}}$ , and when  $f_w = f_{w_{\text{min}}}$  and  $\text{gap} = \text{gap}_{\text{max}}$ . For easier comparison, the scattering parameters obtained for the design parameters  $f_w$  and  $\text{gap}$  are also plotted. For the maximum deviation where  $f_w = f_{w_{\text{max}}}$  and  $\text{gap} = \text{gap}_{\text{min}}$  when  $\epsilon_{r_{\text{eff}}} = 2.43$ , the input return loss increases to around 3 dB while the insertion losses deteriorate up to 10 dB with respect to the designed values. Simultaneously, the upper limit of the stopband is shifted upwards in frequency, expanding the stopband. Opposite, if  $f_w = f_{w_{\text{min}}}$  and  $\text{gap} = \text{gap}_{\text{max}}$ , both the input and return losses are reduced by 1.5 dB and 2 dB, respectively, while the stopband is narrowed. For the biased state, the general effect is similar. When  $f_w = f_{w_{\text{max}}}$  and  $\text{gap} = \text{gap}_{\text{min}}$  the input return loss increases around 3 dB as well, while the insertion losses deteriorate up to 12.5 dB with respect to the designed values. In this case, the upper stopband limit is shifted upwards by 1.2 GHz. If  $f_w = f_{w_{\text{min}}}$  and  $\text{gap} = \text{gap}_{\text{max}}$ , the insertion losses are decreased by 1.5 dB but are still 1 dB higher than at the unbiased state.

At the stopband,  $|S_{21}|$  decreases by 10 dB regarding the designed values while the input rejection increases by 1.2 dB when  $f_w = f_{w_{\max}}$  and  $\text{gap} = \text{gap}_{\min}$ . In this case, almost all input power is rejected by the unit cell, thereby reducing the amount of power that is transferred in the stopband. If  $f_w = f_{w_{\min}}$  and  $\text{gap} = \text{gap}_{\max}$ , the transmission is enhanced by 2 dB while the input reflection improves by 0.5 dB leading to a better matching of the unit cell for lower frequencies.

These strong variations around the stopband, which is the operation range of the final LWA, present a big challenge in terms of impedance matching since a small change in the IDC geometry can lead to considerable variations in the response of the unit cell.

The same tolerance analysis is performed for  $\epsilon_{r_{\text{eff}}} = 3.22$ . The obtained results show a similar tendency as for  $\epsilon_{r_{\text{eff}}} = 2.43$  but shifted downwards in frequency. At the stopband,  $|S_{21}|$  decreases by 10 dB regarding the designed values while the input rejection increases up to 1.2 dB when  $f_w = f_{w_{\max}}$  and  $\text{gap} = \text{gap}_{\min}$ . In this case, all the input power is reflected by the unit cell in the stopband. If  $f_w = f_{w_{\min}}$  and  $\text{gap} = \text{gap}_{\max}$ , the transmission is enhanced by 2 dB while the input reflection improves by 0.5 dB leading to a better matching of the unit cell for lower frequencies.

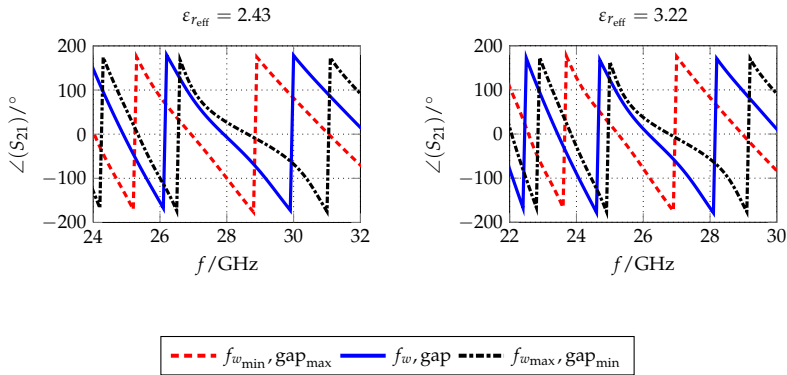


Figure 4.32: Impact of the  $f_w$  and  $\text{gap}$  tolerances on the  $\angle(S_{21})$  for  $\epsilon_{r_{\text{eff}}} = 2.43$  (left), and  $\epsilon_{r_{\text{eff}}} = 3.22$  (right).

Fig. 4.32 shows the effect of manufacturing tolerances on the phase of  $S_{21}$  for the unbiased and biased states. It can be observed that the manufacturing tolerances not only affect the magnitude of  $|S_{21}|$  but also imply a variation in the phase of the propagating signal. For the unbiased state, for a fixed phase, such as  $\angle(S_{21}) = 0$ , the frequency at which that phase is obtained is shifted by 1.7GHz upwards for  $f_w = f_{w_{\max}}$  and  $\text{gap} = \text{gap}_{\min}$  and 1GHz downwards for  $f_w = f_{w_{\min}}$  and  $\text{gap} = \text{gap}_{\max}$  regarding the design value. For the biased state, the frequency at which  $\angle(S_{21}) = 0$  is obtained is shifted 0.7GHz upwards for  $f_w = f_{w_{\max}}$  and  $\text{gap} = \text{gap}_{\min}$  and 1GHz downwards for  $f_w = f_{w_{\min}}$  and  $\text{gap} = \text{gap}_{\max}$  regarding the design value.

Fig. 4.33 shows the effect of manufacturing tolerances of the IDC finger width  $f_w$  and gap on the phase shift per unit cell  $\beta l$ , attenuation per unit cell  $\alpha l$ , and impedance  $Z_B$ . In agreement with the previously obtained results for scattering parameters, all these parameters show a frequency shift and strong variation around the stopband depending on the deviation of the manufactured IDC regarding the design parameters.

The effect of tolerances on the unit cell phase shift is visible in the top row of Fig. 4.33. For  $f_w = f_{w_{\max}}$  and  $\text{gap} = \text{gap}_{\min}$  the stopband is extended towards higher frequencies increasing the width of the stopband from 1GHz to approximately 2.5GHz. If  $f_w = f_{w_{\min}}$  and  $\text{gap} = \text{gap}_{\max}$ , the stopband width is not only reduced but also shifted towards lower frequencies. Since the stopband is delimited by  $f_{se}$  and  $f_{sh}$  and this analysis considers the impact of tolerances on the series IDC, it can be concluded that the variations in frequency of the stopband are the result of varying  $f_{se}$ . This is,  $f_{se}$  is shifted upwards or downwards in frequency while  $f_{sh}$  remains constant. This shift is 1.5GHz for  $f_w = f_{w_{\max}}$  and  $\text{gap} = \text{gap}_{\min}$  and 2GHz for  $f_w = f_{w_{\min}}$  and  $\text{gap} = \text{gap}_{\max}$ .

Similarly to the unbiased state, the strongest variations can be observed around the stopband for  $\epsilon_{r_{\text{eff}}} = 3.22$ . The shift of the series branch frequency  $f_{se}$  is also visible for the two considered cases. When  $f_w = f_{w_{\max}}$  and  $\text{gap} = \text{gap}_{\min}$ ,  $f_{se}$  is shifted upwards in frequency leading to a broader stopband of 2.4GHz. On the contrary, when  $f_w = f_{w_{\min}}$  and  $\text{gap} = \text{gap}_{\max}$ ,  $f_{se}$  experiences a stronger shift downwards in frequency, even below  $f_{sh}$ , which leads to a narrower stopband of 1GHz.

The losses per unit cell are presented in the middle row of Fig. 4.33. As expected, the same phenomenon, regarding the limits of the stopband, can be observed for  $\alpha l$ . When  $f_w = f_{w_{\max}}$  and  $\text{gap} = \text{gap}_{\min}$  the stopband is

extended and thus the attenuation is increased from  $0.01\pi$  up to  $0.0225\pi$ . When  $f_w = f_{w_{\min}}$  and  $\text{gap} = \text{gap}_{\max}$ ,  $f_{se}$  experiences a greater shift in frequency than in the previous case. However, the stopband is narrower and thus the attenuation is reduced to  $0.0075\pi$ . This effect is also reflected on the biased state with the value of  $\alpha l$  slightly higher than in the unbiased state. The stopband is expanded when  $f_w = f_{w_{\max}}$  and  $\text{gap} = \text{gap}_{\min}$ , which, in turn, increases the attenuation of the propagating signal from  $0.012\pi$  up to  $0.024\pi$ . When  $f_w = f_{w_{\min}}$  and  $\text{gap} = \text{gap}_{\max}$  the resulting stopband narrows regarding the designed one. Accordingly,  $\alpha l$  is reduced to  $0.0075\pi$ .

The real part of the Bloch impedance of the lossless unit cell is presented in the bottom row of Fig. 4.33. The effect of the IDC finger width  $f_w$  and gap deviation is also depicted. In agreement with the results obtained from the analysis of  $\beta l$ ,  $\alpha l$ , and the scattering parameters, for  $f_w = f_{w_{\max}}$  and  $\text{gap} = \text{gap}_{\min}$  the impedance characteristic remains the same except for a broader stopband, this is, the zero provoked by the  $f_{se}$  is shifted up in frequency. In opposition, for  $f_w = f_{w_{\min}}$  and  $\text{gap} = \text{gap}_{\max}$  the impedance curve varies, showing a zero first and a pole as a result of  $f_{se}$  being shifted downwards in frequency. In comparison, the impedance on the LHB shows a lower value for  $f_w = f_{w_{\min}}$  and  $\text{gap} = \text{gap}_{\max}$  since it tends to a zero while for the design parameter and  $f_w = f_{w_{\max}}$  and  $\text{gap} = \text{gap}_{\min}$  tends to a pole and, hence, is higher. This behavior is inverted for the RHB. For the biased state, the zero of  $f_{se}$  is shifted towards higher frequencies for  $f_w = f_{w_{\max}}$  and  $\text{gap} = \text{gap}_{\min}$  broadening the stopband, and downwards in frequency when  $f_w = f_{w_{\min}}$  and  $\text{gap} = \text{gap}_{\max}$ .

This variation of the pole and zero of  $Z_B$  increases the difficulty to obtain a matched antenna since each unit cell is susceptible to this manufacturing tolerances.

#### *Analysis of the Deviation of the Metalization Thickness*

The second parameter that is susceptible of deviation during the manufacturing process is the metalization thickness  $t$ . The thickness of the RF metalization influences the propagation of the signal within the unit cell and is therefore considered in this analysis.

The effect of the maximum deviation of the metalization thickness  $t$  on the scattering parameters is depicted in Fig. 4.34 for both the unbiased and biased states. The main difference regarding the analysis of the IDC finger width  $f_w$

Table 4.6: Deviation of unit cell series capacitance and frequency for the design values  $C_{se} = 0.1507$  pF and  $f_{se} = 28.54$  GHz for  $\epsilon_{r\perp} = 2.43$  and  $C_{se} = 0.1680$  pF and  $f_{se} = 27.03$  GHz for  $\epsilon_{r\perp} = 3.22$  for the maximum deviation of the metalization thickness  $t$ .

$\epsilon_{r\text{eff}}$	Parameter	$C_{se}/\text{pF}$	$\epsilon_{C_{se}}$	$f_{se}/\text{GHz}$	$\epsilon_{f_{se}}$
2.43	$t_{\text{max}}$	0.1520	0.86%	28.21	-0.42%
	$t_{\text{min}}$	0.1496	-0.71%	28.44	0.37%
3.22	$t_{\text{max}}$	0.1695	0.89%	26.72	-0.44%
	$t_{\text{min}}$	0.1669	-0.65%	26.92	0.33%

and gap is that a variation of  $t$  does not yield a strong shift in frequency. The variation of the series frequency  $f_{se}$  is 0.1 GHz regarding the design value for both  $t_{\text{max}}$  and  $t_{\text{min}}$ .

For the unbiased state, the input return losses at the LHB and RHB are better than 14 dB. At the LHB, the input return losses for the designed unit cell are 16.58 dB. This value decreases in 1.56 dB when  $t = t_{\text{max}}$  whereas for  $t = t_{\text{min}}$  the input return losses increase in 1.18 dB. Similarly, in the RHB the input return losses improve in 4.81 dB regarding the design value when  $t = t_{\text{max}}$  and increase in 0.55 dB when  $t = t_{\text{min}}$ . The insertion losses experience no variation due to the tolerances of the metalization thickness.

For the biased state, the overall input return losses are better than 11.22 dB in the propagation bands. At the LHB, the input return losses increase due to the proximity of a stopband for frequencies below 20 GHz. For the frequencies immediately below the unit cell stopband, the input return losses for the design values are 19.7 dB. This value improves to 21.15 dB when  $t = t_{\text{max}}$  and deteriorates to 17.84 dB when  $t = t_{\text{min}}$ . At the RHB, a smaller variation occurs. The input return losses for the design value  $t$  equal 11.39 dB. When  $t = t_{\text{max}}$ , this value improves in 0.56 dB and degrades in 0.39 dB when  $t = t_{\text{min}}$ . Again, the insertion losses remain invariable independently of the value of the metalization thickness.

Fig. 4.35 shows the phase of  $S_{21}$ . Both for the unbiased and biased states is visible that the deviation of RF metalization  $t$  has barely an influence on on frequency, since the distance between the frequency points for which  $\angle(S_{21}) = 0$  is obtained is 0.1 GHz.

The influence of the deviation of  $t$  on the dispersion characteristic of the unit cell is shown in Fig. 4.36. The top row represents the phase shift per unit cell  $\beta l$ , the middle row the attenuation  $\alpha l$ , and the bottom row is the real part of the impedance  $\text{Re}\{Z_B\}$ . According to the results obtained from the scattering parameters the maximum deviation, this is, when  $t = t_{\max}$  or  $t = t_{\min}$  barely affects the dispersion characteristic per unit cell or the position of the pole and zero that limit the stopband. The only parameter that appears to influence, and only to a considerably small extent, is the attenuation constant within the stopband. The stopband is expanded by 0.1 GHz when  $t = t_{\min}$ , which is reflected in an increase of  $\alpha l$  from  $0.01056\pi$  to  $0.011\pi$  and decreases to  $0.00948\pi$  when  $t = t_{\max}$ .

#### *Analysis of the Deviation of the Height of the LC Cavity*

The third parameter under analysis is the height of the LC cavity  $h$ . There are several error sources during the manufacturing process that can influence the value of  $h$ . First, the realization of the cavity in the brass metal block by a milling machine. This is a minor error source for the chosen height  $h$ , since the milling machine has a precision lower than  $2\ \mu\text{m}$ . The second error source is the gluing of the glass substrate onto the metal block to form the unit cell and LWA. The glue drops have to be leveled in order to obtain a plain and even glue layer as thin as possible so that the cavity height remains constant along the complete LWA.

Fig. 4.37 shows the unit cell scattering parameters for the design value  $h$  and the maximum deviation values  $h = h_{\max}$  and  $h = h_{\min}$  for the unbiased and biased states. As it can be observed, neither for  $h = h_{\max}$  nor  $h = h_{\min}$  a significant variation of the RF response is produced. In other words, even with a 20% variation of the cavity height  $h$ , the dispersion characteristic of the unit cell is not affected.

The values obtained for  $h = h_{\max}$  and  $h = h_{\min}$  are summarized in Table 4.7. This confirms that the effect of the  $h$  deviation is negligible in terms of frequency dispersion.

It can be concluded that the effect of deviation of the metalization thickness  $t$  and LC cavity height  $h$  on the dispersion characteristic of the unit cell and thus the LWA, can be neglected. In contrast, the deviation of finger width  $f_w$  and gap of the series branch IDC has a strong effect on the performance of the unit cell. Moreover, the tolerances on the IDC make the impedance matching

Table 4.7: Deviation of unit cell series capacitance and frequency for the design values  $C_{se} = 0.1507$  pF and  $f_{se} = 28.54$  GHz for  $\epsilon_{r\perp} = 2.43$  and  $C_{se} = 0.1680$  pF and  $f_{se} = 27.03$  GHz for  $\epsilon_{r\perp} = 3.22$  for the maximum deviation of the liquid crystal cavity height  $h$ .

$\epsilon_{r\text{eff}}$	Parameter	$C_{se}/\text{pF}$	$\epsilon_{C_{se}}$	$f_{se}/\text{GHz}$	$\epsilon_{f_{se}}$
2.43	$h_{\text{max}}$	0.1506	-0.06%	28.55	0.04%
	$h_{\text{min}}$	0.1507	0%	28.54	0%
3.22	$h_{\text{max}}$	0.1679	-0.06%	27.04	0.04%
	$h_{\text{min}}$	0.1681	0.06%	27.02	-0.04%

of the antenna a challenging issue. This is a challenging matter, that has to be approached in further investigations. An automated manufacturing process, where the tolerances are strictly controlled, could be the key for future mass production of such type of metamaterial based antennas.

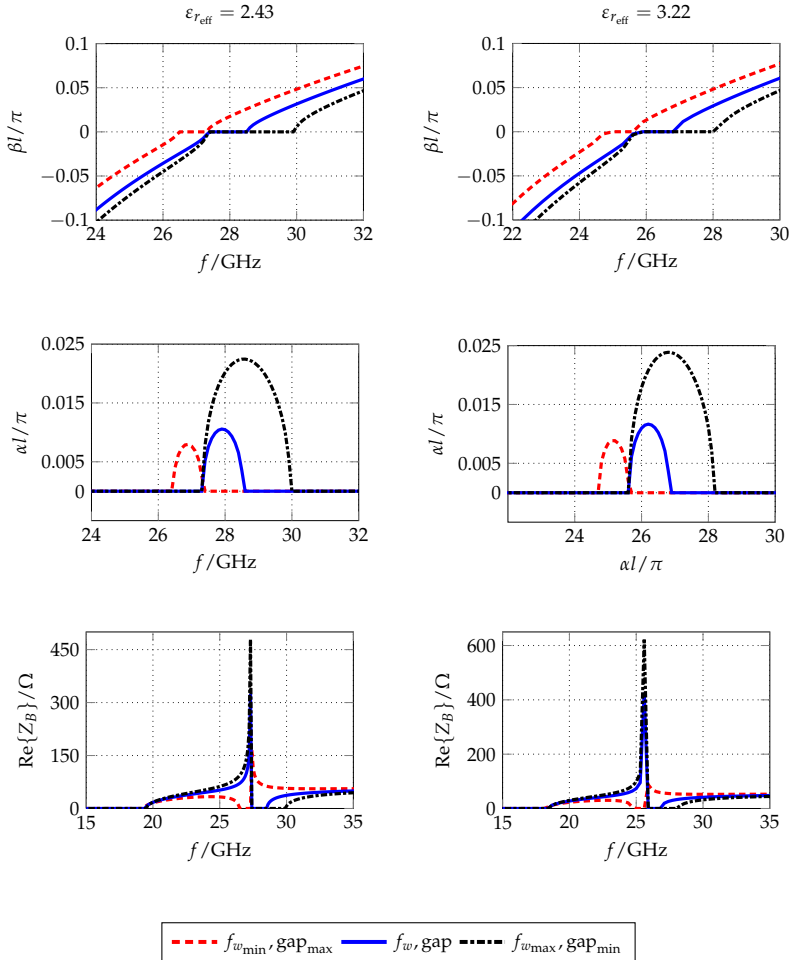


Figure 4.33: Impact of  $f_w$  and gap tolerances on  $\beta l / \pi$  and  $\alpha l / \pi$  per unit cell, and  $\text{Re}\{Z_B\}$  for  $\epsilon_{r_{\text{eff}}} = 2.43$  (left), and  $\epsilon_{r_{\text{eff}}} = 3.22$  (right).

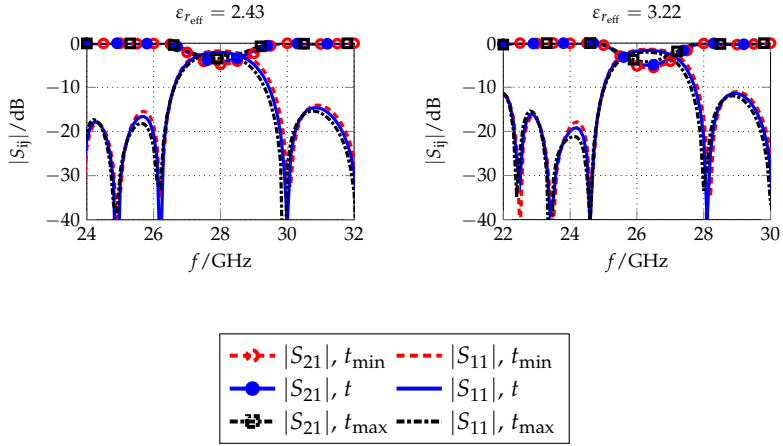


Figure 4.34: Impact of the metalization thickness  $t$  deviation on the scattering parameters for  $\epsilon_{r_{\text{eff}}} = 2.43$  (left), and  $\epsilon_{r_{\text{eff}}} = 3.22$  (right).

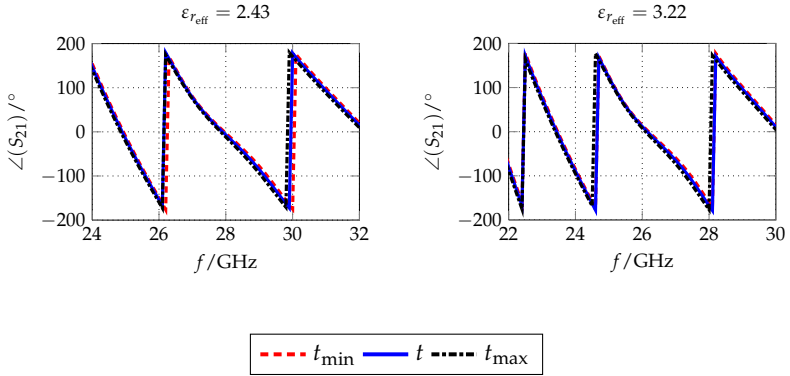


Figure 4.35: Impact of the metalization thickness  $t$  deviation on the  $\angle(S_{21})$  for  $\epsilon_{r_{\text{eff}}} = 2.43$  (left), and  $\epsilon_{r_{\text{eff}}} = 3.22$  (right).

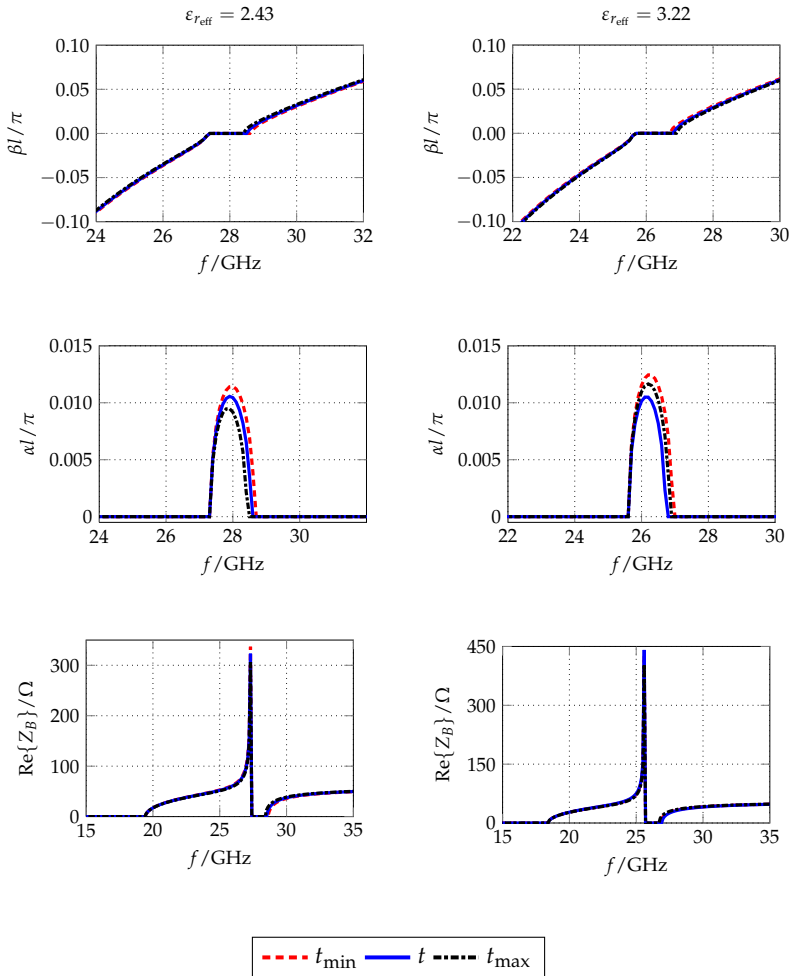


Figure 4.36: Impact of the metalization thickness  $t$  deviation on  $\beta l / \pi$  and  $\alpha l / \pi$  per unit cell, and  $\text{Re}\{Z_B\}$  for  $\epsilon_{r_{\text{eff}}} = 2.43$  (left), and  $\epsilon_{r_{\text{eff}}} = 3.22$  (right).

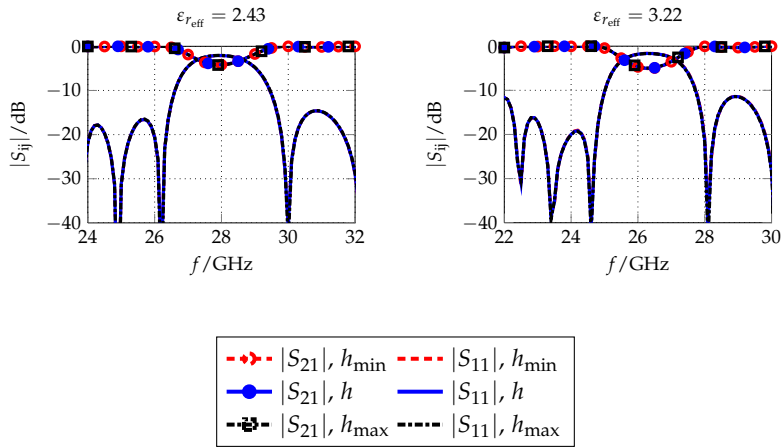


Figure 4.37: Impact of the LC cavity height  $h$  deviation on the scattering parameters for  $\epsilon_{r,\text{eff}} = 2.43$  (left), and  $\epsilon_{r,\text{eff}} = 3.22$  (right).

## 4.6 LOSS ANALYSIS

The propagation constant is defined as  $\gamma = \alpha_T + j \cdot \beta$  (2.14), where  $\alpha_T$  represents the total amount of losses of the propagating wave. For the LWA,  $\alpha_T$  is defined as

$$\alpha_T = \alpha_{\text{leak.}} + \alpha_{\text{metal.}} + \alpha_{\text{diel.}} \quad (4.10)$$

where  $\alpha_{\text{leak.}}$  represents the amount of energy that is leaked from the wave guiding structure i.e, radiated. The metallic and dielectric losses, i.e.  $\alpha_{\text{metal.}}$  and  $\alpha_{\text{diel.}}$ , represent the metallic losses in the RF metalization of the LWA and the losses in the dielectric components of the LWA such the LC and the BF33 glass substrate, respectively.  $\alpha_{\text{metal.}}$  and  $\alpha_{\text{diel.}}$  are undesired but also unavoidable.

It is desirable that the total amount of radiation losses  $\alpha_{\text{leak.}}$  of the LWA is as high as possible. Nevertheless, metamaterial unit cells are so small compared to the wavelength of the propagating wave that the amount of power radiated by a single unit cell is very little. Only the addition of the power radiated by all unit cells of the metamaterial LWA is significant. This effect is important in the design process of the LWA, since it is not possible to calculate  $\alpha_{\text{leak.}}$  in advance. Instead, it is desired that the radiation per unit cell is as small as possible so that the power is radiated along the complete length of the LWA and not just within the first unit cells. If the amount of energy leaked per unit cell is very high, then all energy is radiated at the beginning of the LWA structure. This implies a very short effective aperture of the antenna, which leads to a wide radiation lobe and very low directivity. In contrast, if the amount of power radiated by the unit cell is very low, a higher number of unit cells are needed to radiate the inputted power in its entirety, thereby resulting in a bigger effective aperture and a narrower and more directive radiation lobe.

In this section, an analysis of the losses is carried out for 1 unit cell to study the power leaked by a single element of the LWA and the effect of the metallic and dielectric losses not only on the overall losses per unit cell but also on the phase shift at the unbiased state, this is, when  $\epsilon_{r\text{eff}} = 2.43$ . Subsequently, this analysis is performed again for 5 unit cells in order to see if the effect of the losses is sustained along the complete LWA.

Fig. 4.38 shows the different losses obtained from the full-wave simulation of a single unit cell. First, a characteristic curve is presented where only radiation losses are taken into account, which means all metalizations are

simulated as perfect conductors and all dielectric components are simulated without losses. This result corresponds, therefore, to the radiation losses of the unit cell due to the leakage. Thus,  $\alpha_{\text{leak}}$  remains stable along frequency with a value of approximately  $0.45\pi$  and experiences a considerable rise at the stopband.

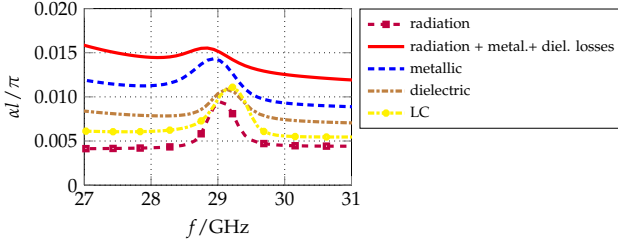


Figure 4.38: Losses for 1 unit cell for  $\epsilon_{r,\text{eff}} = 2.43$ .

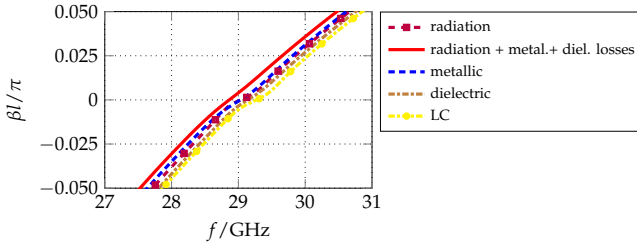


Figure 4.39: Effect of the losses on the phase shift of one unit cell for  $\epsilon_{r,\text{eff}} = 2.43$ .

As the dielectric losses are added, a shift in frequency, together with an increase of the losses can be observed. The dielectric losses are separated in two different curves to see the effect of the LC material, which is responsible for the majority of the dielectric losses.

The metallic losses produce not only a shift towards lower frequencies but are also the most significant losses of all. It can be observed that they represent the major contribution to the total amount of losses per unit cell. When all losses are taken into consideration, the difference between the losses in the stopband and the losses at what will be the operation frequency of the antenna, around 27 GHz, is not significant anymore. This effect is also visible in the phase shift of the unit cell, shown in Fig. 4.39, where for the lossy case

the stopband disappears and  $\beta l / \pi$  seems balanced. This is a typical behavior of strongly lossy CRLH transmission lines [45].

The effect of the losses on the phase shift can be seen in Fig. 4.39. It can be observed that, although metallic losses are the most important source of power loss, they barely influence the behavior in frequency of the unit cell. It is the addition of all the losses what provokes a shift in  $\omega_{se}$  and  $\omega_{sh}$  and shifts phase shift curve about 0.2 GHz downward in frequency .

Since it is not possible to simulate the complete antenna a further losses analysis is carried out for 5 unit cells to analyze the effect of the higher order modes on the losses of the LWA. The effect of the losses on the frequency can be seen in Figs. 4.40 - 4.42. The left-handed propagation band is delimited by two stopbands, one in the transition from the LHB to the RHB and a second one at lower frequencies where the discretization limit is reached. Below this frequency, the unit cell length  $l$  is not smaller than  $\lambda_g/10$  anymore. As a result, a new stopband appears that goes downwards in frequency.

Fig. 4.40 shows the losses per unit cell extracted from a 5 unit cell simulation using the scattering parameter matrix and the Nicholson-Ross-Weir Method for  $\epsilon_{r_{eff}} = 2.43$ .

The stopband between the LHB and the RHB goes from 28 GHz to 29 GHz approximately and is recognizable in Fig. 4.40 for the leakage, metallic and dielectric losses as they increase considerably within it. If the leakage, metallic and dielectric losses are considered individually a second stopband appears at 26 GHz due to the discretization limit, which forces a rise of the losses in between these two stopbands. Notwithstanding, if the overall losses are taken into account, as in the lossy case, it can be seen that the losses not only increase  $\alpha_T$  but also shift both stopbands downward in frequency.

This effect is also noticeable in Fig. 4.41 and Fig. 4.42. The lower frequency that defines the stopband between the LHB and the RHB is shifted downward in frequency, shifting also the discretization limit below 24 GHz and modifying the phase shift per unit cell in the LHB and, in turn, the radiation angle  $\psi$  of the antenna in the backward quadrant.

All in all, the contribution of each unit cell and the higher order modes can not be neglected when considering the losses, since the radiation, metallic and dielectric losses as a whole do not only influence the amount of radiated or dissipated energy but the behavior of the LWA in frequency and , therefore, the LWA beam scanning performance.

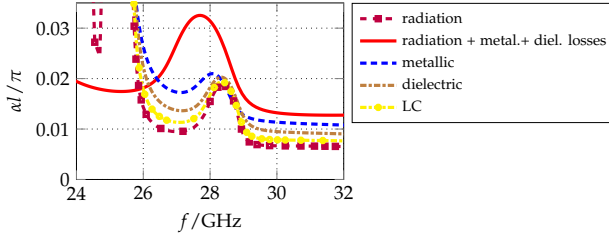


Figure 4.40: Losses per unit cell for  $\epsilon_{r_{\text{eff}}} = 2.43$  considering five unit cells.

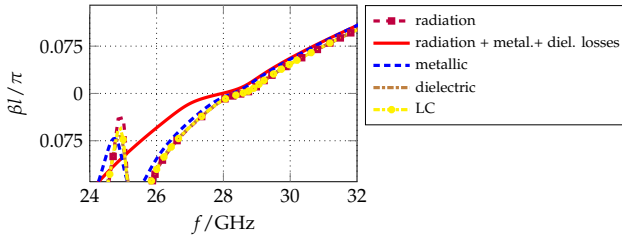


Figure 4.41: Effect of the losses on the phase shift per unit cell for  $\epsilon_{r_{\text{eff}}} = 2.43$  considering five unit cells.

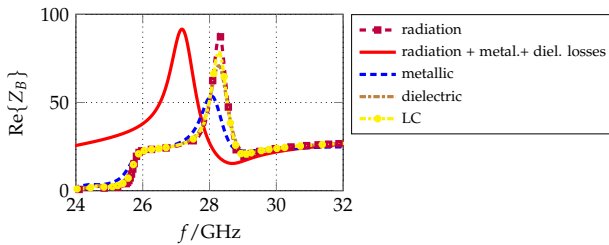


Figure 4.42: Effect of the losses on the  $\text{Re}\{Z_B\}$  for  $\epsilon_{r_{\text{eff}}} = 2.43$  considering five unit cells.

# 5

---

## LIQUID CRYSTAL BASED TUNABLE METAMATERIAL LEAKY WAVE ANTENNA

---

In this chapter, a leaky wave antenna is designed and manufactured based on the unit cell presented in chapter 4. To the best knowledge of the author, the leaky wave antenna presented in this work is the first metamaterial based leaky wave antenna that can perform continuous beam steering from the backward to the forward quadrant through the broadside direction in the Ka-Band.

In this chapter, two prototypes of the metamaterial leaky wave antenna are fabricated, a magnetically biased LWA with 15 unit cells and an electrically biased LWA with 32 unit cells. The first is used not only as a proof-of-concept but to test the capability of the magnetic tuning and, by comparison, evaluate the impact of parasitic effects introduced by the biasing circuitry in the electrically tuned LWA. The electrically tuned leaky wave antenna is the main objective of this work. Accordingly, not only its scanning behavior and radiation properties are presented but also response time investigations are carried out in this chapter.

### 5.1 TUNING TECHNIQUES: DESIGN AND IMPLEMENTATION

Two prototypes of the LWA are fabricated, one working with magnetic tuning and the other with electric tuning. The tuning of the prototypes is based on the LC alignment techniques introduced in section 2.2. For magnetic tuning, a special setup is designed and fabricated. The electric tuning is carried out by incorporating a biasing network to the RF structure of the LWA..

### 5.1.1 Magnetic Tuning

Magnetic tuning varies the orientation of the LC director  $\vec{n}$  and, therefore, the effective permittivity encountered by the electromagnetic wave by applying a static magnetic field  $\vec{H}_{DC}$ . For this purpose, two rare earth magnets with a field strength of 1.4 T are used. For the far field measurements a magnetic biasing setup was specially designed and fabricated to hold the magnets while providing the maximum magnetic flux in the LC filled cavity.

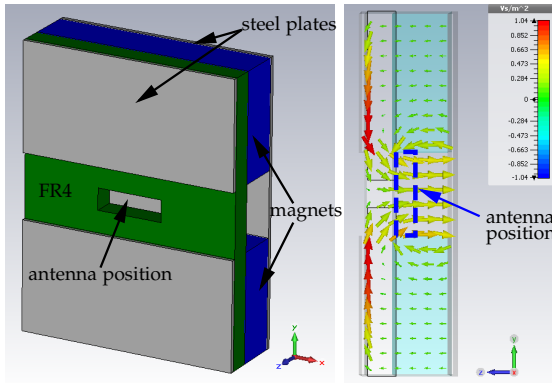


Figure 5.1: Profile and cross section of the designed magnetic biasing setup.

Fig. 5.1 shows the magnetic biasing setup profile and the simulation of the magnetic flux in the cavity where the antenna is intended to be positioned. The setup is made up of three layers: the bottom and top layers are steel plates used to concentrate the magnetic flux. The middle layer consists of two separated PVC holders that contain the magnets. The FR4 (epoxy) substrate, placed between the magnets and the top steel plates, supports the antenna and coaxial K-connectors.

Fig. 5.2 depicts the magnetic flux density  $|B|$  between both magnets.  $|B|$  is simulated in CST EM Studio for the antenna plane represented as  $zy$  in the figure. The center of the antenna is taken as reference position  $d = 0$ . At this position, the magnetic flux density that aligns the LC molecules equals 0.38 T.

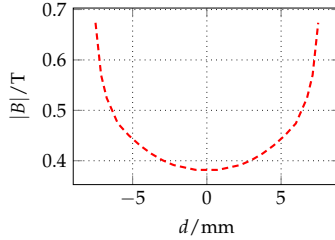


Figure 5.2: Simulated magnetic flux density between the magnets in vertical direction.

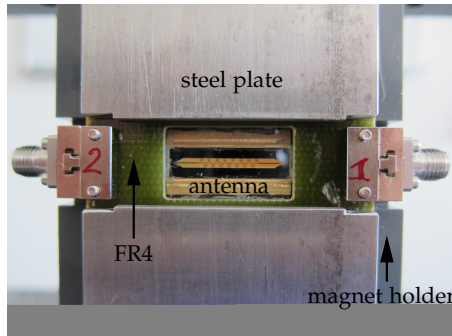


Figure 5.3: Photograph of the antenna prototype inside the biasing setup.

In Fig. 5.3 the final manufactured prototype consisting of fifteen unit cells can be seen incorporated into the magnetic biasing setup for far field measurements.

### 5.1.2 Electric Tuning

Electric tuning is performed by means of highly resistive biasing lines that are made of nickel chromium with a thickness of 20 nm, a width of 15  $\mu\text{m}$ , and a length of 10.98 mm which leads to a resistance of 73.2 k $\Omega$ . They are meander shaped in order to increase their length and thus their resistance. Fig. 5.4 depicts how the NiCr lines connect every second unit cell, delivering two voltages  $V_{DC1}$  and  $V_{DC2}$  at each side of the IDCs. To orient the LC

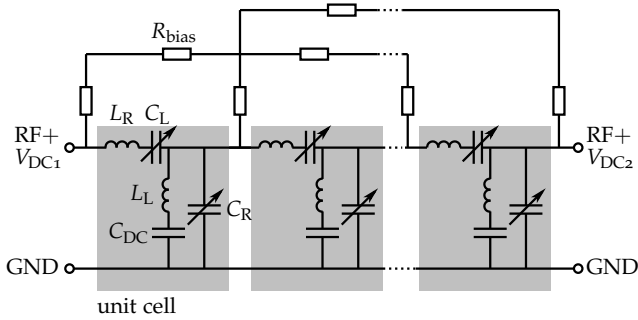


Figure 5.4: LWA periodically repeated unit cell with resistive biasing network incorporated.

director  $\vec{n}$  parallel to the RF electric field in the biased state, the condition  $V_{DC1} = -V_{DC2}$  has to be fulfilled. Fig. 5.5 shows a microscope photograph of several unit cells and the biasing lines interconnecting them.

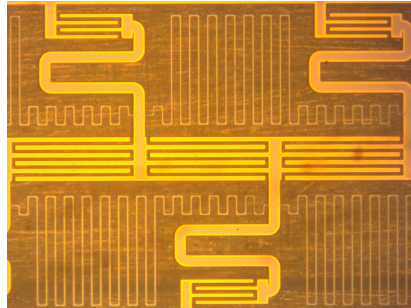


Figure 5.5: Microscopic picture of the biasing network implemented within the unit cell layout. The RF structure consists of  $2\ \mu\text{m}$  thick gold and the resistive biasing network of  $10\ \text{nm}$  NiCr.

Figs. 5.6a and 5.6b show the simulated current density along 5 unit cells of the LWA when the biasing lines have an inductive or resistive characteristic, respectively. If the biasing network section belonging to the first two unit cells is compared, it can be observed that the current density in the bias lines in both cases is different. Fig. 5.6a shows how the RF signal propagates along the biasing lines when these are made of gold, which has a significant lower resistivity than NiCr, and thus provides them with an inductive nature. To

prevent this undesired effect, the biasing lines are made of highly resistive NiCr. This forces the RF signal to propagate only along the purposely designed structure, i.e. the unit cells, as depicted in Fig. 5.6b.

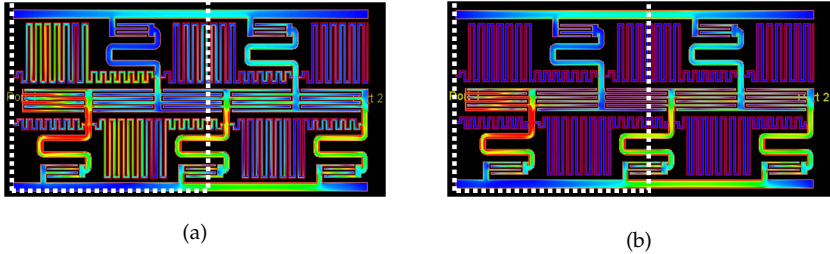


Figure 5.6: Simulated RF current distribution at 26.7 GHz for different biasing network implementations. (a) Inductive biasing network. (b) Resistive biasing network.

The fabrication of both LWA prototypes is made following the process described in detail in section 4.3. For the case of the electrically biased LWA some further manufacturing steps are carried out for the implementation of the biasing network.

## 5.2 MAGNETICALLY BIASED LEAKY WAVE ANTENNA

The magnetically biased LWA is fabricated following the process described in section 4.3. The fabricated prototype of the magnetically biased LWA consists of a periodical repetition of the unit cell as presented in Fig. 5.7.

The scattering parameter measurements are carried out in order to obtain the unit cell phase shift with the on-wafer measurement setup shown in Fig. 5.8. For the S-parameter measurements, GSG Probes with 250  $\mu\text{m}$  pitch size are used. These probes are not suited for far field measurements with a turntable due to their high sensitivity to movement. Hence, K-connectors are used for the far field measurements.

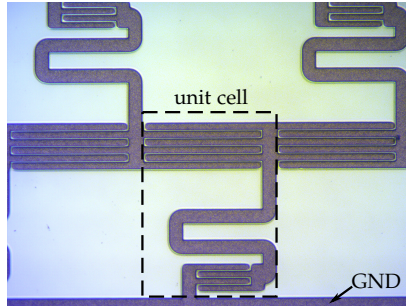


Figure 5.7: Microscope view of the magnetically biased leaky wave antenna. The unit cell layout of the magnetically biased LWA includes  $C_{DC}$  but not the biasing lines.

The K-connectors are mounted after the S-parameter measurement. Due to the difficulty to mount the connectors on the glass substrate, a taper between the antenna and the connector is required. The taper section is fabricated on PET film. A gold layer of  $2\ \mu\text{m}$  thick is plated on it. The PET taper is manufactured following the same process described in section 4.3.

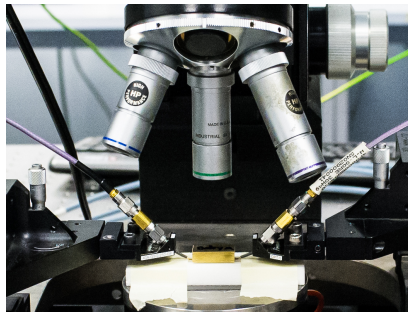


Figure 5.8: On-wafer measurement setup used for S-parameter characterization.

Fig. 5.9a shows the frontside of the manufactured magnetically biased LWA prototype, inserted in the FR4 support. In Fig. 5.9b, the backside of the LWA antenna with the PET taper sections that connect the antenna to the K-connectors is presented.

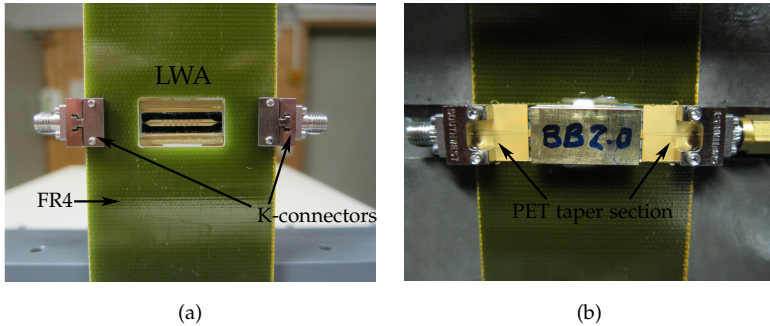


Figure 5.9: Photograph of the magnetically biased LWA prototype inside the biasing setup. (a) Frontside. (b) Backside with the PET taper sections.

The PET taper section connects the K-connectors with the LWA by means of bonding wires. A microscope picture of the complete connection is shown in Fig. 5.10a, where, from left to right, the antenna GSG contact, the taper section, and the contact pin of the K-connector can be seen.

Fig. 5.10b shows the bonding wires that electrically connect the taper to the antenna. The process to build the bonding wires is extremely complicated in this case. Two major challenges are faced during this process. First, the wires do not fix perfectly to the PET substrate due to the inherent flexibility of the substrate. If too much tension is applied while bonding the wire, this detaches from the PET substrate taking the gold metal on the surface of the taper with it. This can be observed on the lower side of the picture, marked as gold bare spots. Second, the proximity of the bonding area to the antenna complicates the work of the bonding machine since there is almost no place for it to perform the bonding. As a result, the PET taper and the bonding wires are only used in the magnetically biased LWA and a more optimal solution was searched for the electrically biased LWA.

### 5.2.1 Dispersion Characteristics

The simulations for the magnetically biased LWA are carried out in the full wave simulator of Agilent Advanced Design System taking into account metallic and dielectric losses as well as radiation effects. In Fig. 5.11 the simu-

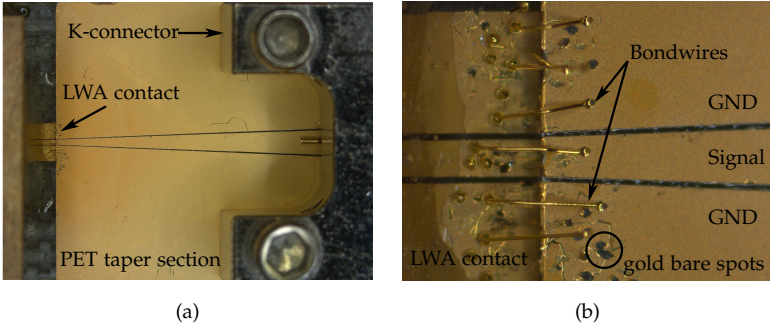


Figure 5.10: Microscope photograph of the K-connector, PET taper transition, and bonding wires connecting the taper to the magnetically biased LWA. (a) Overall view. (b) Detailed photograph of the bonding wires that connect the PET taper to the LWA.

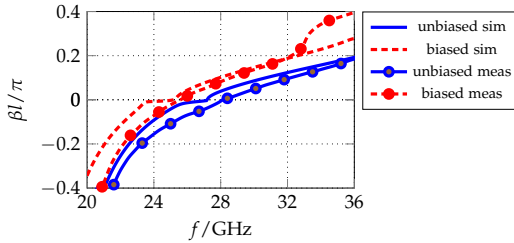


Figure 5.11: Measured and simulated unit cell phase shift for the different tuning states.

lated and measured unit cell phase shift is presented for both biased and unbiased states. The phase shift per unit cell is extracted from the simulated and measured scattering parameters applying the Nicholson-Ross-Weir-Extraction method [73] (section 2.3.1). Simulations show a stopband between 23.5 GHz and 25 GHz for the biased state and 25.8 GHz and 27.3 GHz for the unbiased state. As expected, the dispersion curve is shifted downwards in frequency for the biased state.

In the measurements, the stopband disappears due to the overall losses and the anisotropy of LC, which cannot be taken into account in the simulations and provokes the shunt  $\omega_{sh}$  and series  $\omega_{se}$  frequencies to be shifted in opposite directions. For the biased and unbiased states, the frequencies for the

broadside radiation, i.e. where  $\psi = 0$ , are 28.15 GHz and 25.6 GHz, respectively.

Since both measured dispersion curves are balanced, with  $\omega_{se} = \omega_{sh}$ , it is possible for a fixed frequency of 27 GHz to vary the unit cell phase shift between  $\beta l = -0.04\pi$  and  $\beta l = 0.05\pi$ . According to (3.1) this corresponds to a nearly symmetrical beam steering range of  $\psi = -19.6^\circ$  to  $\psi = 22.5^\circ$  with respect to the broadside direction. This is confirmed by the extracted radiation angle along frequency, shown in Fig. 5.12. The extracted radiation angle is obtained applying equation (3.1) over the measured unbiased and biased phase shift curves presented in Fig. 5.11.

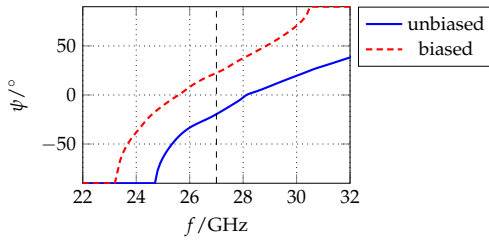


Figure 5.12: Radiation angle extracted from the measured phase shift per unit cell.

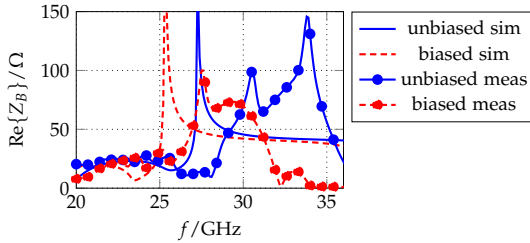


Figure 5.13: Measured and simulated characteristic impedance for the different tuning states.

The simulated and measured real part of the Bloch impedance  $\text{Re}\{Z_B\}$  are depicted in Fig. 5.13. In the simulated impedance, the zero at  $\omega_{se}$  and the pole at  $\omega_{sh}$  correspond to the stopband cutoff frequencies of the unit cell phase shift diagram for both states. In the LHB, the matching is not optimal since the impedance takes values around  $25\ \Omega$ . This is due to the resonance introduced by  $C_{DC}$  at lower frequencies which makes  $Z_B$  tend to zero. A

possible solution for future designs would be to implement a larger  $C_{DC}$  so its resonance frequency is shifted much further downwards in frequency. In the RHB,  $Z_B$  is  $40\Omega$  which is close to the desired value of  $50\Omega$  and kept almost constant along the complete band.

In a CRLH structure, as introduced in section 2.1.2, the stopband frequencies  $\omega_{se}$  and  $\omega_{shr}$ , correspond to a pole and a zero in the Bloch impedance, respectively [45]. In the balanced case, i.e. for  $\omega_{se} = \omega_{shr}$ , the pole and the zero cancel out which provides a flat impedance response. This cancellation has to be perfect, which makes the impedance extremely sensitive to manufacturing inaccuracies and explains the strong impedance variation near the transition frequency between the LHB and the RHB. However, despite the fact that the measured dispersion diagrams are balanced, the zeros and poles of the measured  $Z_B$  do not cancel exactly at the same frequency. This is due to inaccuracies in the manufacturing process that lead to slightly different resonance frequencies for the different unit cells as seen in section 4.5.

### 5.2.2 Calculation of Far Field Patterns of Leaky Wave Antennas.

The simulation of a leaky wave antenna far field pattern is a highly arduous process in terms of memory consumption and simulation time. Consequently, the conventional approach to the problem is considering the LWA as an array of isotropic radiating elements separated by a fixed distance [89, 93, 94]. The far field pattern  $FF(\theta, \phi)$  of a LWA is defined as

$$FF(\theta, \phi) = UC(\theta, \phi) \cdot AF(\theta, \phi) \quad (5.1)$$

where  $UC(\theta, \phi)$  is the pattern of one single radiating element corresponding to one unit cell and  $AF(\theta, \phi)$  the array factor of the complete antenna [45].

If the number of elements of the LWA is low, i.e. the electrical length of the antenna is short, then the total far field pattern  $FF(\theta, \phi)$  will be more influenced by the single element pattern  $UC(\theta, \phi)$ . On the contrary, if the electrical length of the antenna is big (ideally infinite) the total far field pattern will tend to the value of the array factor [45]. This is,

$$FF(\theta, \phi) \approx \begin{cases} UC(\theta, \phi), & \text{if } NI/\lambda_0 \rightarrow 0. \\ AF(\theta, \phi), & \text{if } NI/\lambda_0 \rightarrow \infty, \end{cases} \quad (5.2)$$

where  $N$  is the number of unit cells that conform the LWA and  $l$ , which is the length the unit cell, is considered the distance between two consecutive radiators.

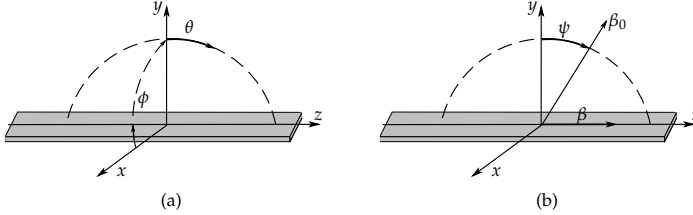


Figure 5.14: (a) Spherical coordinates  $(\theta, \phi)$  used to calculate the array factor of the LWA. (b) Radiation angle of the main beam of the LWA  $\psi$  regarding the broadside direction.

For the antennas presented in this work, each CRLH unit cell is considered as a point radiator along the  $z$ -axis, with a field distribution of  $\vec{E}_0(x, y = 0, z) = \vec{E}_0(x, z)$  in the LWA plane ( $XZ$ ), according to Fig. 5.14. This field distribution is Fourier transformed to obtain the spectral power density of one single radiator in terms of wave number in directions  $x$  and  $z$ :

$$\text{UC}(k_x, k_z) = \frac{1}{4\pi^2} \int_{-1/2}^{1/2} \int_{-p/2}^{p/2} \vec{E}_0(x, z) \cdot e^{j(k_x \cdot x + k_z \cdot z)} dk_x dk_z. \quad (5.3)$$

The unit cell far field contribution  $\text{UC}(k_x, k_z)$  is then transformed into spherical coordinates [89, 95]:

$$\text{UC}(r, \theta, \phi) \approx j \frac{k_0 e^{-jk_0 r}}{2\pi r} \cdot \cos\theta \cdot \sin\phi \cdot \text{UC}(k_x, k_z). \quad (5.4)$$

The array factor  $\text{AF}$  of a unidimensional leaky wave antenna placed along the  $z$ -axis can be written as [45]

$$\text{AF}(\theta) = \sum_{n=0}^{N-1} e^{np(jk_0 \sin\theta - \alpha + j\beta)}, \quad (5.5)$$

where the radiation angle  $\psi$  is represented through (3.1) and  $\alpha$  takes into account the losses due to leakage.

Hence, the radiated far field of the leaky wave antenna is given by

$$\vec{E}(r, \theta, \phi) = \text{UC}(r, \theta, \phi) \cdot \text{AF}(\theta). \quad (5.6)$$

Equation (5.6) is used to calculate the simulated far field radiation pattern, directivity  $D$  and half power beamwidth HPBW of the two antenna prototypes presented in further sections of this chapter.

### 5.2.3 Directivity Calculations

For the calculation of the leaky wave antenna directivity  $D$ , the array factor method introduced previously is used. For the antenna prototypes presented within this work,  $AF(\theta)$  is obtained considering each unit cell as an isotropic point radiator. The array factor method provides information not only about the directivity of the antenna but also about its performance along the left- and right-handed bands, including beamwidth and secondary lobes. Moreover, it can be applied to both simulated and measured dispersion parameters.

Figs. 5.15 shows the directivity  $D$  of the magnetically biased LWA over frequency for the unbiased and biased states, respectively. This directivity is obtained by applying the array factor to dispersion parameters  $\alpha$  and  $\beta$  obtained from full-wave simulations. To compare between the array factor method and the radiation angle obtained from (3.1), the later is also represented as a white line in every directivity depiction. The radiation angle corresponding to the main lobe varies when the frequency is changed. This characteristic can be used for frequency scanning. Nevertheless, since a fixed operating frequency is used within the frame of the work, the far field pattern is shown for both the unbiased state (a) and the biased state (b).

If a fixed frequency is chosen in Fig. 5.15 along the observation angle, e.g. 27 GHz, it can be observed how the radiation angle varies when the biasing is applied. At this frequency, the antenna works in the stopband for the unbiased state and in the right-handed band in the biased state, which agrees with the results presented in Fig. 5.11 for the simulated magnetically biased leaky wave antenna.

Fig. 5.16 shows the directivity calculated with the measured dispersion parameters  $\alpha$  and  $\beta$  for the unbiased and biased states of the magnetically biased LWA, respectively. The radiation angle obtained applying equation (3.1) is represented by a white line. In agreement with Fig. 5.11, the stopband disappears, showing a continuous beam scanning from the backward to the forward quadrant along frequency. For the operation frequency of 27 GHz,

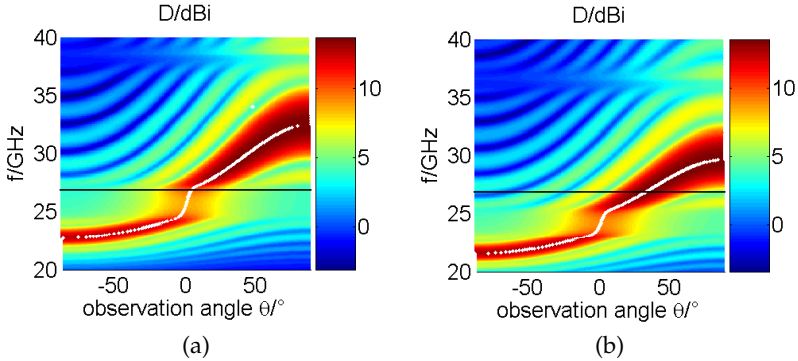


Figure 5.15: Directivity along frequency and observation angle calculated with simulated dispersion characteristics of the magnetically biased LWA. (a) Unbiased state. (b) Biased state.

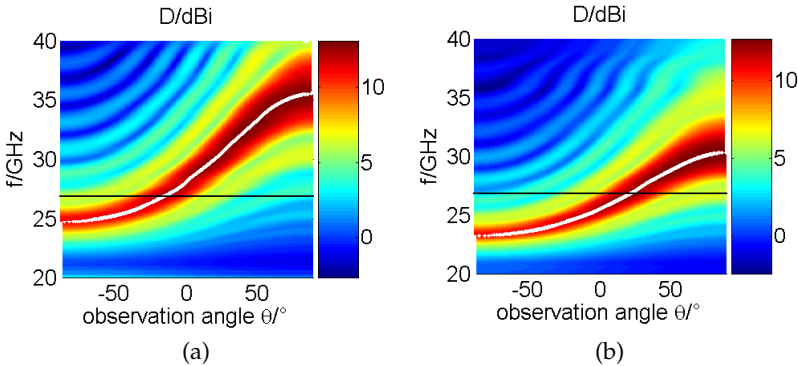


Figure 5.16: Directivity along frequency and observation angle calculated with measured dispersion characteristics of the magnetically biased LWA. (a) Unbiased state. (b) Biased state.

the magnetically biased LWA radiates at  $\psi = -19,6^\circ$  for the unbiased state and at  $\psi = 22.5^\circ$  for the biased state.

Taking a cut along observation angle for the operation frequency of 27 GHz in Fig. 5.16, then Fig. 5.17 is obtained. Here, the directivity of the magnetically biased LWA is shown for the unbiased and biased states. For the unbiased state, the antenna radiates at  $\psi = -18.8^\circ$  and shows a maximum directivity

of  $D = 13.4$  dBi and a half power beamwidth of  $\text{HPBW} = 56.6^\circ$  for the unbiased state. For the biased state, the antenna radiates in the forward quadrant at  $\psi = 23.8^\circ$  with a maximum directivity of  $D = 13.43$  dBi and a  $\text{HPBW} = 58.5^\circ$ . The beam scanning range is  $\Delta\psi = 42.6^\circ$ , which agrees with the results presented in Fig. 5.12.

The effective aperture of the antenna is  $L/\lambda_0 = 1.044$ , which is considerably below the standard  $L/\lambda_0 = 9$  of traditional LWAs (section 3.1) and leads to a considerably larger half power beamwidth.

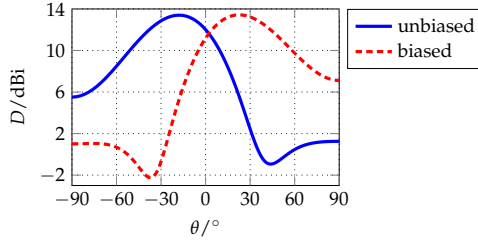


Figure 5.17: Directivity of the magnetically biased LWA at 27 GHz obtained from the measured dispersion characteristics.

#### 5.2.4 Measured Radiation Pattern

The measured radiation pattern of the magnetically biased LWA for the desired operation frequency of 27 GHz is shown in Fig. 5.18. According to the radiation angle extracted from the measured dispersion diagram shown in Fig. 5.11 and the resulting pattern obtained from the array factor method shown in Fig. 5.16, the main beam should be shifted from  $\psi = -19.6^\circ$  to  $22.5^\circ$  when the magnetic biasing is applied. In the measured far field for the unbiased state, this is confirmed by the maximum radiated power at an angle of  $\psi = -18^\circ$ . For the biased state, though, the main beam points to  $\psi = -7^\circ$ , which equals a beam scanning range of  $11^\circ$ .

The good agreement of the unbiased state and the decreased scanning range indicate that the lower scanning range is due to the fact that the LC director  $\vec{n}$  is not completely parallel to the applied  $\vec{B}_{DC}$  field lines in the biased state. This is due to the larger distance of the rare earth magnets, which have to be placed behind the antenna in the purposely designed setup of section 5.1,

in comparison to the on-wafer measurements, where the biasing magnets are placed directly under the glass substrate and thus, closer to the LC layer.

The side lobe level can be improved by increasing the number of unit cells, which is done in the electrically biased LWA prototype.

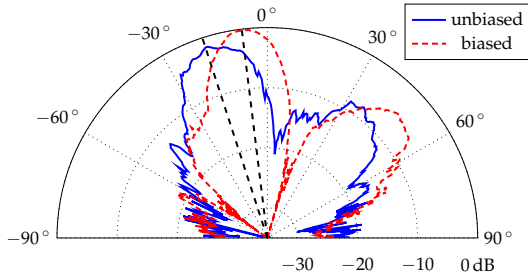


Figure 5.18: Measured far field patterns at 27 GHz for the magnetically biased LWA.

The presented antenna is designed to work at the fixed frequency of 27 GHz and achieve continuous beam scanning. Nevertheless, the antenna is capable of performing beam steering at other frequencies as well. As an example of the antenna beam scanning capabilities in the LHB and RHB, the far field pattern at 26 GHz and 28 GHz is presented in Figs. 5.19 and 5.20, respectively.

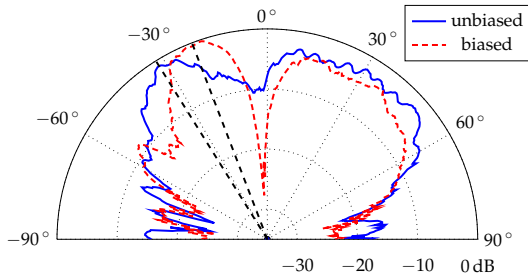


Figure 5.19: Measured far field patterns at 26 GHz for the different tuning states.

At 26 GHz, the antenna is working on the LHB. For the unbiased state, the LWA radiates at  $\psi = -32^\circ$ , which is in agreement with the radiation angle extracted from the measured dispersion characteristic presented in Figs. 5.12 and 5.16. At the biased case, and according to the extracted angle and directivity, the LWA is expected to radiate at  $\psi = 8^\circ$ . Instead, the main beam

radiates at  $\psi = -21^\circ$ , leading to a total scanning of  $\Delta\psi = 11^\circ$ . Again, the longer distance at which the magnets are placed within the far field measurement setup in comparison to that of the scattering parameters measurements is responsible for this effect. In the far field measurements, the flux of the used magnets is not large enough to completely reorient the LC molecules and, as a result, the scanning range is strongly diminished.

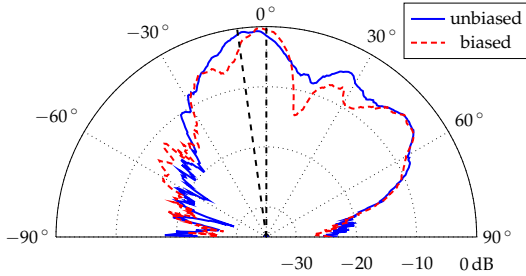


Figure 5.20: Measured far field patterns at 28 GHz for the different tuning states.

The far field plot of the magnetically biased LWA at 28 GHz is presented in Fig. 5.20. Similarly to the results obtained at 27 GHz and 26 GHz, the unbiased state shows agreement with the predicted results shown in Figs. 5.12 and 5.16 and the antenna main direction is  $\psi = -8^\circ$ . For the biased state, both the extracted angle method and the array factor method predict that the antenna main beam direction is  $\psi = 40^\circ$ . However, the measured far field pattern shows that the radiation angle is reduced to  $\psi = 0^\circ$ .

Moreover, for those frequencies for which the LWA is not specifically designed, a strong degradation of the side lobe level can be observed.

On the whole, it has been proved by the present magnetically biased LWA that continuous beam scanning through broadside is possible with this metamaterial based LWA. Nevertheless, an increase on the number of unit cells and an optimization on the LC biasing is required to obtain a LWA that satisfies the required continuous beam scanning from the backwards to the forward quadrant while providing high directivity and optimal side lobe level.

## 5.3 ELECTRICALLY BIASED LEAKY WAVE ANTENNA

The electrically biased LWA is formed by 32 unit cells. The electric biasing circuitry is incorporated to the unit cell to distribute the tuning voltage along the structure. The LWA is shown in Fig. 5.21 before mounting the BF33 substrate on the metal block. In Fig. 5.21a can be seen that four holes are drilled in the glass substrate for the K-connector so there is no need to use the PET taper and the bonding wires anymore. This configuration provides more stability to the whole antenna once mounted. Moreover, the cables needed to measure the S-parameters with a VNA can be directly connected to the antenna without using an on-wafer measurement setup. The slot along the metal block will form the LC cavity once the BF33 is glued on top. Fig. 5.21b shows a detailed microscope view of the RF structure of the LWA with the biasing circuitry incorporated in the layout.

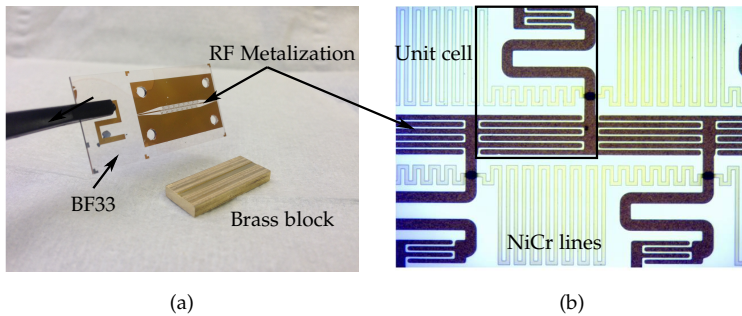


Figure 5.21: (a) Electrically biased LWA components: BF33 substrate with the RF metalization, and ground metal block. (b) Microscopic photograph of the RF metalization and NiCr lines that form the unit cells and the biasing circuitry, respectively.

## 5.3.1 Dispersion Characteristics

The scattering parameters of the electrically biased leaky wave antenna are obtained by means of full-wave simulation in Agilent Advanced Design System including dielectric and metallic losses as well as radiation effects. The highly resistive nickel chromium lines are included in the simulations. The antenna

is simulated and measured for both untuned and tuned states. To obtain the corresponding radiation angles at each state, vectorial network analysis measurements are carried out. From the obtained S-parameters, the phase shift per unit cell  $\beta l$  is calculated using the Nicholson-Ross-Weir-Extraction method mentioned in section 2.3.1. For the obtained phase shift  $\beta l$  at each frequency, the corresponding radiation angles are extracted using (3.1) for the unbiased and biased states.

For the electric biasing, DC voltages between 0 V and 60 V are applied at each port of the antenna. First, the antenna characteristic is measured for the unbiased state. This is, the applied voltage equals 0 V. Afterward, the DC voltage is progressively increased in 10 V steps until the applied voltage reaches 60 V, when the maximum tuning is achieved.

Fig. 5.22 shows the measured and simulated normalized unit cell phase shift  $\beta l / \pi$  for biased and unbiased states. Simulations show a slight change in the slope of the phase shift curve. This is caused by the fact that  $\omega_{se}$  and  $\omega_{sh}$  have not exactly the same value.

The frequency shift between unbiased and biased states is around 1.8 GHz for simulation and measurements. At 26.7 GHz, the measured phase shift per unit cell can be tuned between  $\beta l = -0.025\pi$  for the unbiased state and  $\beta l = +0.012\pi$  for the biased state.

For lower frequencies, the phase shift curves diverge due to fact that the unit cell size is not anymore small compared to the wavelength of the propagating signal within the structure. This a discretization effect and implies that the unit cell can not be considered infinitely small as assumed in section 2.1, since the condition  $l < \lambda_g/10$  is not satisfied anymore.

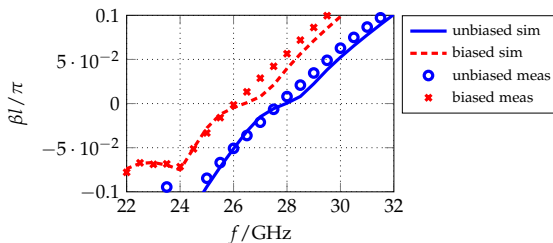


Figure 5.22: Measured and simulated unit cell phase shift for both biased and unbiased states for the electrically biased leaky wave antenna.

Fig. 5.23 represents the frequency dependent radiation angle  $\psi$  obtained from the simulated and measured phase shift using (3.1). The LHB is limited by the stopband below 23 GHz which provokes that for frequencies corresponding to this band the variation of the radiation angle is higher compared to that in the RHB, which extends to frequencies above 32 GHz.

For the operation frequency of 26.7 GHz, the extracted measured angles correspond to  $\psi = -11.7^\circ$  for the unbiased state and  $\psi = 5.34^\circ$  for the biased state. From this, it can be derived that it is possible to continuously steer the LWA beam for a fixed frequency from the backward quadrant to the forward quadrant through broadside direction when a DC voltage is applied.

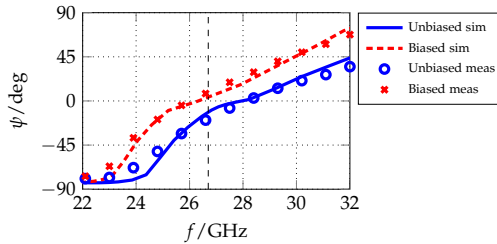


Figure 5.23: Radiation angle extracted from the measured and simulated unit cell phase shift for both biased and unbiased states.

Fig. 5.24 shows the simulated and measured input reflection at the biased and unbiased states. It can be observed that applying the biasing voltage in the simulation shifts the transmission bands of the antenna by around 1.5 GHz. In the case of measurements, this shift is not visible anymore. This is due to the fact that these kind of structures are, by definition, very narrow banded, which means the LWA is only matched at certain frequency. This, together with the strong phase shift per unit cell increases the difficulty to obtain a constant impedance value  $Z_B$ , which leads to general degradation of  $|S_{11}|$  along the spectrum.

In the simulated biased state, where the LHB spans between 23 GHz and 25.5 GHz, the matching degrades the lower the frequency due to the vicinity of a stopband for frequencies below 23 GHz. This effect is also visible in the unbiased state where the LHB covers from 23 GHz to 27 GHz. The input reflection increases in the stopband up to  $-3$  dB for the biased state, between 26 GHz and 27.8 GHz, and up to  $-5$  dB for the unbiased, from 27.5 GHz to 28.5 GHz, respectively.

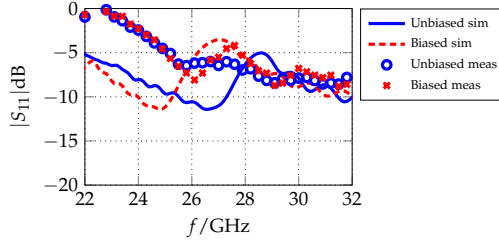


Figure 5.24: Simulated and measured input reflection for biased and unbiased states.

For the measured input reflection, the stopband between the LHB and the RHB is drastically reduced in the biased case and even disappears for the unbiased case. Similarly to the magnetically biased LWA, this is due to the combination of the overall losses and the anisotropy of the liquid crystal, which cannot be taken into account in the simulations and provokes the series and shunt frequencies  $\omega_{se}$  and  $\omega_{sh}$  to be shifted in opposite directions.

In the simulations, all molecules of the liquid crystal material are considered to be positioned parallel among themselves and oriented in the same direction. Consequently, LC appears as a dielectric with uniform effective permittivity  $\epsilon_{r,eff}$  to the propagating RF field  $\vec{E}_{RF}$ . Conversely, real LC is an anisotropic material, which implies that, although the general macroscopic director  $\vec{n}$  is oriented according to the aimed effective permittivity, it is possible that individual molecules are not oriented in the direction of the macroscopic director  $\vec{n}$ . This effect is stronger, the further these molecules are from the metalization where the DC voltage is applied.

The simulated and measured real part of the Bloch impedance  $\text{Re}\{Z_B\}$  are depicted in Fig. 5.25. In the simulated impedance, the pole and the zero that correspond with  $\omega_{se}$  and  $\omega_{sh}$  and define the stopband are recognizable. Similarly to the magnetically biased LWA, the matching in the LHB takes values around  $25\Omega$  due to the low frequency resonance introduced by  $C_{DC}$ . In the RHB, the impedance shows an increasing tendency, from the zero limiting the stopband to higher values around  $30\Omega$ . At the desired operation frequency of  $26.7\text{GHz}$ , the impedance for the unbiased state takes a value of approximately  $47\Omega$  and  $23\Omega$  for the biased state. These variations in the impedance of the antenna difficult the matching and degrade, therefore, the input reflection.

For the measured  $\text{Re}\{Z_B\}$ , it can be observed that, in accordance with the phase shift curves shown in Fig 5.22, the stopband has almost disappeared and the impedance varies between  $10\ \Omega$  and  $55\ \Omega$  for the presented frequency range. At  $26.7\ \text{GHz}$ , the impedance is  $17\ \Omega$  for the unbiased state and  $20\ \Omega$  for the biased which is deviated from the initially intended  $50\ \Omega$  design. This effect strongly degrades the input reflection of the electrically biased LWA and is provoked by working so close to the stopband. The impedance matching represents, therefore, one of the biggest challenges in the design and fabrication of this metamaterial antennas.

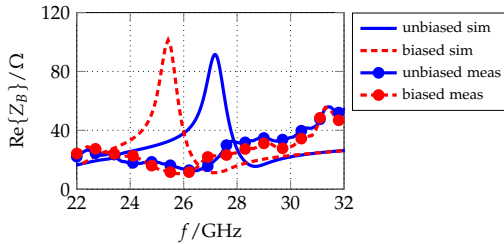


Figure 5.25: Simulated and measured real part of the Bloch impedance  $\text{Re}\{Z_B\}$  for both biased and unbiased states.

### 5.3.2 Impact of the Biasing Circuitry on the Dispersion Characteristic

Fig. 5.26 shows the lossless simulated phase shift per unit cell of the LWA with and without the biasing circuitry. First, the simulation is carried out with perfect dielectrics and conductors, except for the NiCr biasing lines. Second, the simulation is repeated without the biasing circuitry. This is made to compare the effect of the electric biasing circuitry on the dispersion characteristic of the presented leaky wave antenna. As it can be observed in Fig. 5.26, both results agree showing that the effect of the bias lines on the dispersion characteristic of the antenna is negligible.

### 5.3.3 Directivity Calculations

If equation (3.3) with the leakage ratio  $\alpha_{\text{leak}}/k_0 = 0.02$  is applied to the present electrically biased LWA, the amount of unit cells required to achieve

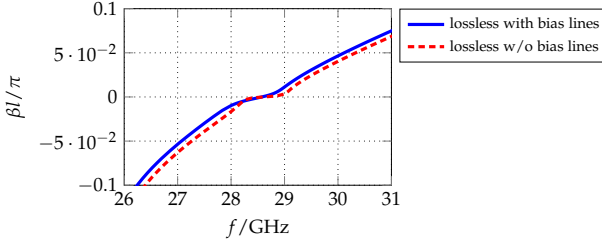


Figure 5.26: Lossless simulated phase shift per unit cell with and without the electric biasing circuitry.

the ideal radiation of 90% of the power with high directivity is  $N = 140$ . However, due to limitations in the fabrication process, the LWA can be manufactured with a maximum of  $N = 32$  unit cells. As a result, the presented LWA has an effective aperture of  $L/\lambda_0 = 2.065$ , which is 4.5 times smaller than the effective aperture of standard LWAs  $L/\lambda_0 = 9$ . Accordingly, the shorter aperture leads to a lower directivity and higher HPBW in comparison with traditional LWA.

Fig. 5.27 shows the directivity  $D$  for along frequencies and observation angle  $\theta$  for the unbiased and biased states, respectively. Here, the directivity is obtained applying the array factor method to the simulated dispersion characteristic of the LWA. In addition, the radiation angle obtained with equation (3.1) is also represented as a white line for comparison. The main beam varies its width depending on the frequency and shows the LH and RH propagation bands and the stopband in between for both the biased and unbiased states. The radiation angle varies from the unbiased to the biased state along frequency, being shifted downwards as the effective permittivity of the liquid crystal is increased.

For the operating frequency of the electrically biased LWA of 26.7 GHz, the main beam points at  $\psi = -11.6^\circ$ , which corresponds to the LHB, for the unbiased state. For the biased state shown in Fig. 5.27b, the radiation direction is  $\psi = 5.2^\circ$ , corresponding to the RHB of the LWA.

Fig. 5.28 shows, for both unbiased and biased states, the directivity  $D$  along frequency obtained from the measured dispersion characteristic of the electrically biased LWA. In agreement with the results obtained for the measured phase shift per unit cell (Fig. 5.22), the stopband is barely visible and the antenna shows the capability of continuous beam scanning at broadside direc-

tion when operated at 26.7 GHz and from  $-90^\circ$  to  $90^\circ$  if frequency scanning is applied.

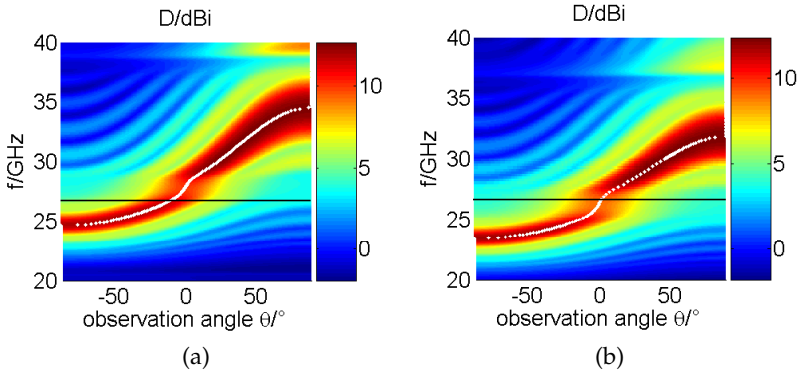


Figure 5.27: Directivity along frequency and observation angle calculated with simulated dispersion characteristics of the electrically biased LWA. (a) Unbiased state. (b) Biased state.

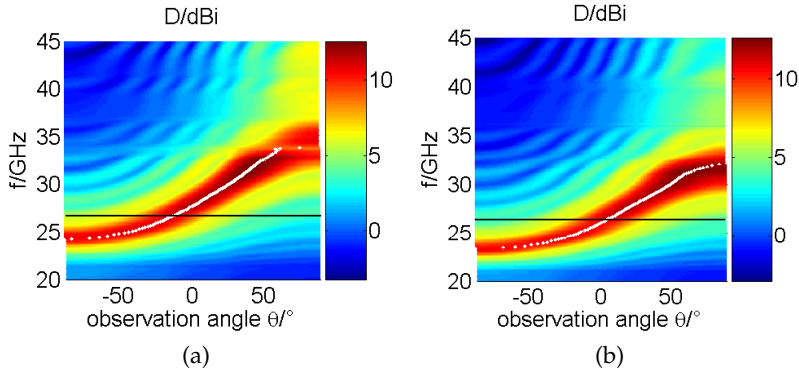


Figure 5.28: Directivity along frequency and observation angle calculated with measured dispersion characteristics of the electrically biased LWA. (a) Unbiased state. (b) Biased state.

For a cut of the directivity plot at 26.7 GHz along the observation angle in Figs. 5.28a and 5.28b, Fig. 5.29 is obtained. Here, the directivity and HPBW can be observed in more detail. The radiation angles presented in Fig. 5.29 confirm those obtained from Figs. 5.28a and 5.28b. In this case, the LWA an-

tenna is made up of 32 unit cells and, for the operating frequency of 26.7 GHz, shows a maximum directivity of  $D = 15.81$  dBi and a half power beamwidth of  $\text{HPBW} = 29.9^\circ$  for the unbiased state. For the biased state, the antenna radiates in the forward quadrant with a maximum directivity of  $D = 17.4$  dBi and a  $\text{HPBW} = 26.6^\circ$ . Therefore, the scanning range obtained from the simulated far field pattern is  $\Delta\psi = 20.7^\circ$ , which is better than the scanning range of  $17.04^\circ$  extracted from the S-parameter measurements, as shown in Fig. 5.23.

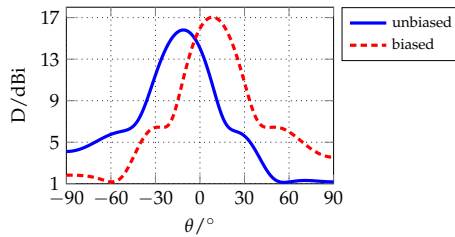


Figure 5.29: Directivity of the electrically biased LWA at 26.7 GHz obtained from the measured dispersion characteristics.

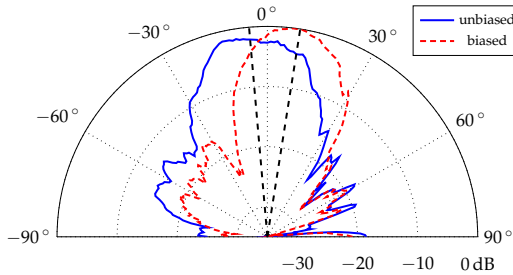


Figure 5.30: Measured far field patterns normalized to maximum power level of the main beam at 26.7 GHz for the two tuning states.

#### 5.3.4 Measured Radiation Pattern

Fig. 5.30 shows the measured radiation pattern of the electrically biased leaky wave antenna for the operation frequency 26.7 GHz. The presented LWA is able to scan through broadside direction, i.e. from  $\psi = -6^\circ$  for the unbiased

state to  $\psi = 9^\circ$  for the biased. The radiation patterns are normalized to the maximum power level of the main beams.

The measured scanning range is slightly smaller than the angle difference obtained from Fig. 5.23 and the simulated far field pattern of Fig. 5.29. The higher losses in the LH propagation band (unbiased state) lead to a degradation of the beam amplitude and the side lobe level regarding the RHB (biased state).

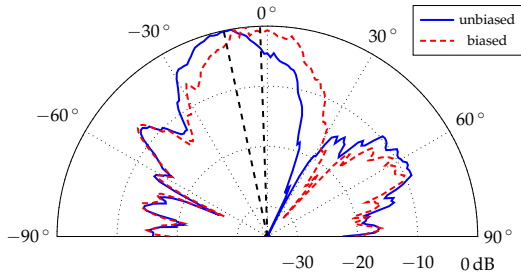


Figure 5.31: Measured far field patterns normalized to maximum power level of the main beam at 26 GHz for the two tuning states.

Similarly to the the magnetically biased LWA, this prototype can also be tuned in the left- and right-handed bands. Figs. 5.31 and 5.32 show the measured radiation patterns of the electrically biased leaky wave antenna operating at 26 GHz, and 28 GHz, respectively. All radiation patterns are normalized to the maximum power level of the main beam in each case.

For 26 GHz, the antenna radiates in the backward quadrant since it works in the left-handed band LHB for both unbiased and biased states. The radiation angles at this frequency are  $\psi = -12^\circ$  for the unbiased and  $\psi = -2^\circ$  for the biased state. The LWA beam scanning measured in the far field is smaller than the beam scanning predicted from the extracted angle presented in Fig. 5.23. The higher steepness of the LHB due to the proximity of the stopband for frequencies below 23 GHz makes the matching difficult and increases, therefore, the losses. The higher losses in this band lead to a degradation of the main beam and the side lobe level.

For the RHB, the radiation pattern at 28 GHz is presented. In this case, the radiation pattern shows a radiation angle of  $\psi = 12^\circ$  for the unbiased state and  $\psi = 29^\circ$  for the biased, leading to a total scanning range of  $\Delta\psi = 17^\circ$ .

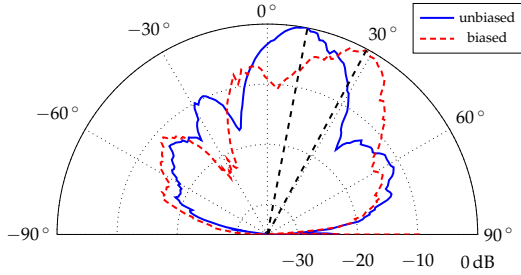


Figure 5.32: Measured far field patterns normalized to maximum power level of the main beam at 28 GHz for the two tuning states.

Table 5.1 summarizes the measured radiation angle  $\psi$ , beam scanning  $\Delta\psi$ , side lobe level SLL, and the difference in the main beam power level  $|\Delta P|$  for both unbiased (0 V) and biased states (60 V) at the previously mentioned frequencies.

Table 5.1: Far field properties: measured radiation angle  $\psi$ , beam scanning  $\Delta\psi$ , side lobe level SLL and power amplitude difference  $|\Delta P|$ .

	$\psi/^\circ$	$\Delta\psi/^\circ$	SLL/dB	$ \Delta P /dB$
	0 V/60 V		0 V/60 V	
26 GHz	-12/ -2	10	7/6	1
26.7 GHz	-6/9	15	-13/ -17	2
28 GHz	12/29	17	10/7	0.25

This shows a scanning range of  $10^\circ$  in the LHB,  $15^\circ$  around broadside, in the transition between LHB and RHB, and  $17^\circ$  in the RHB and proves that the electrically biased LWA is not only able to continuously radiate through broadside for a fixed frequency but also in the left- and right-handed bands, offering the possibility of performing beam steering by frequency scanning as well as at a fixed frequency.

### 5.3.5 Cross Polarization Measurement

The polarization of a plane wave is the trace described with time by the electric field vector when observed from a fixed point. This polarization

is that of the antenna that transmitted the electromagnetic wave and varies with the antenna radiation pattern angle, i.e.  $\theta$  [96]. Among other antenna parameters such as directivity, the amount of power received by an antenna strongly depends on the polarization of the incoming wave and that of the receiving antenna [89, 96].

The LWA presented in this work has a linear polarization. Accordingly, if the major polarization axis of the incident wave is parallel to that of the receiving antenna, i.e. the LWA, the signal will be received with the maximum power. In this case, antenna and incident wave are matched in polarization, i.e. they are co-polarized. If the major polarization axis of the incident wave is perpendicular to that of the antenna, then incident wave and LWA are mismatched in polarization [97, 98]. This is depicted in Fig. 5.33.

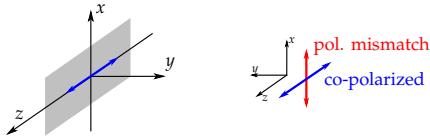


Figure 5.33: Polarization match and mismatch between a propagating wave and a receiving antenna.

Ideally, when the antenna and the incident wave are co-polarized, the power received by the antenna in the perpendicular direction  $P_{\perp}$  is zero. Although this power is not zero in reality, it is aimed to minimize it as much as possible. The ratio between the power received when the LWA and incident wave are co-polarized  $P_{\parallel}$  and the power received when they are mismatched  $P_{\perp}$  is calculated as

$$\frac{X_{\text{pol}}}{\text{dB}} = \frac{P_{\perp}}{\text{dBm}} - \frac{P_{\parallel}}{\text{dBm}}. \quad (5.7)$$

Fig. 5.34 shows  $X_{\text{pol}}$  along the radiation pattern angle  $\theta$  for the electrically biased LWA at 26.7 GHz. For the unbiased case, the cross-polarization  $X_{\text{pol}}$  at  $\psi = -6^{\circ}$ , i.e. the main beam direction of the LWA, is  $-24.82$  dB whereas for the biased state the cross-polarization level equals  $-25.77$  dB at the radiation angle  $\psi = 9^{\circ}$ .

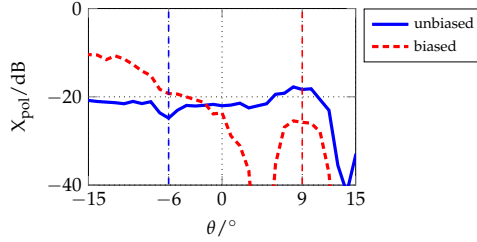


Figure 5.34: Measured cross-polarization of the LWA at 26.7 GHz for the unbiased and biased states.

### 5.3.6 Radiation Efficiency

The radiation efficiency

$$\eta_r = \frac{P_{\text{rad}}}{P_{\text{inj}}}, \quad (5.8)$$

is obtained from full-wave simulations in ADS.  $P_{\text{rad}}$  is the radiated power and  $P_{\text{inj}}$  is the power injected to the antenna. Hence, the input reflected power is taken into account for the calculation of the radiation efficiency  $\eta_r$ .

Since only a maximum of  $N = 7$  unit cells can be simulated, the total radiation efficiency of the complete leaky wave antenna is unknown. To analyze the dependence of the radiation efficiency with the number of unit cells simulated, Fig. 5.35 shows the radiation efficiency obtained for simulations of different number of unit cells.

The obtained  $\eta_r$  increases with the number of the unit cells but no guess can be done about the final  $\eta_r$  of the presented LWA prototype. The simulated  $\eta_r$  is strongly influenced by the lack of perfect impedance matching, that keeps  $P_{\text{inj}}$  low. Achieving better matching, one of the challenges faced during this work and requiring further investigations, would considerably enhance the radiation efficiency.

Table 5.2 summarizes the measured radiation angle  $\psi$ , beam scanning  $\Delta\psi$ , side lobe level SLL, the difference in the main beam power level  $|\Delta P|$ , directivity  $D$ , half power beamwidth HPBW, and cross-polarization  $X_{\text{pol}}$  for both unbiased (0 V) and biased (60 V) states at the operation frequency 26.7 GHz.

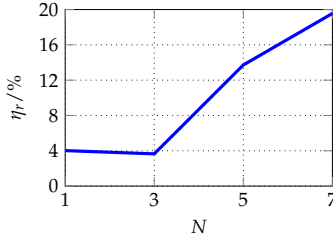


Figure 5.35: Simulated radiation efficiency of the LWA at 26.7 GHz for different number of unit cells.

Table 5.2: Far field properties at 26.7 GHz: measured radiation angle  $\psi$ , beam scanning  $\Delta\psi$ , side lobe level SLL, power amplitude difference  $|\Delta P|$ , directivity  $D$ , half power beamwidth HPBW, and cross-polarization  $X_{\text{pol}}$ .

$\psi / ^\circ$	$\Delta\psi / ^\circ$	SLL/dB	$ \Delta P  / \text{dB}$	$D / \text{dBi}$	HPBW/ $^\circ$	$X_{\text{pol}} / \text{dB}$
0 V/60 V		0 V/60 V		0 V/60 V	0 V/60 V	
-6/9	14	-13/ -17	2	15.8/17.4	29.9/26.6	-24.82/ -25.77

The directivity of the LWA can be enhanced by increasing the number of unit cells. With an increasing number of unit cells, the directivity and side-lobe level of the LWA are improved [79]. This rise of the number of unit cells improves the gain and the side lobe level but has no effect on the radiation angle. The number of unit cells that can be added to the LWA to improve the side lobe level is limited by the leakage factor, since when all power has been leaked, no further improvement can be obtained by adding further unit cells. Instead, the leakage factor has to be modified which implies a modification of the unit cell itself.

Fig. 5.36 shows the effect of the number of unit cells  $N$  on the simulated far field pattern of the presented antenna. If  $N$  is decreased from 32 to 16 unit cells, the HPBW is increased and the directivity decreases by 5 dB. On the contrary, if the number of unit cells is increased up to  $N = 64$  the HPBW decreases strongly and the directivity increases up to  $D = 11$  dBi, which is already in the order of metamaterial based leaky wave radiators [99, 100]. In each case, the radiation angle remains constant.

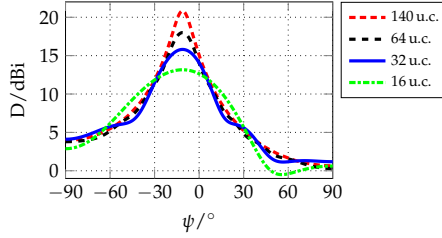


Figure 5.36: Directivity of the presented electrically biased LWA at the unbiased state for different number of unit cells.

### 5.3.7 Response Time Investigations

Technological evolution nowadays leads to real time applications, where fast response times are a crucial matter. Although liquid crystal is slower than other technologies such as semiconductor diodes, it is very well suited for high frequency real time systems with middle to high latency like satellite communications [101, 102]. In this section, both the response and relaxation times of the CRLH LC based LWA as well as their influence on the beam steering capabilities of the leaky wave antenna are measured and presented. For this purpose, voltages between 0 V for the unbiased state and 120 V for the maximum biased state are applied. All presented results in this section correspond to 99% of the total beam steering  $\psi(V_{DC})$  achieved.

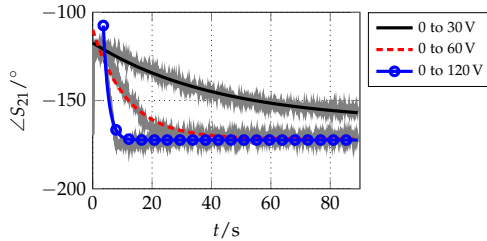


Figure 5.37: Switch on time influence on the phase of  $S_{21}$  for different biasing voltages.

For the operation frequency 26.7 GHz, the measured far field pattern shown in Fig. 5.30 is obtained. At this operation frequency, the applied maximum biasing voltage  $V_{DC,MAX}$  is 120 V. Applying higher tuning voltages  $V_{DC}$  does

not influence the beam scanning but decreases the response time of the liquid crystal.

Fig. 5.37 shows the measured response times of the phase of  $S_{21}$  when different tuning voltages are applied to the metamaterial based LWA. It can be seen that with an increased tuning voltage, the time needed to reach a stabilization of the phase is reduced. When the maximum voltage of 120 V is applied, the LC needs approximately 19 s to reach the maximum tunability state, this is,  $\varepsilon_{eff} = \varepsilon_{r||} = 3.22$ . This time increases up to 250 s when only 30 V are applied.

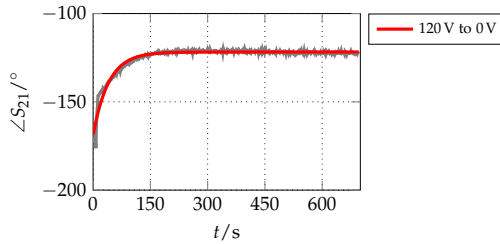


Figure 5.38: Switch off time influence on the phase of  $S_{21}$  for 120 V.

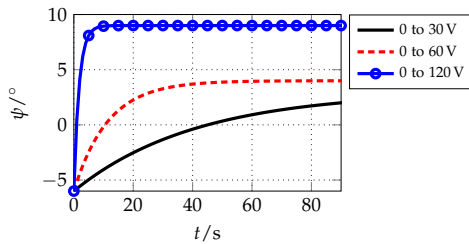


Figure 5.39: Radiation angle along time with respect to broadside direction.

Fig. 5.38 shows the variation on the measured phase of  $S_{21}$  for the worst case regarding response time, this is, when the applied maximum voltage  $V_{DC_{MAX}}$  is switched off. In this case, only the polyimide layer pulls the molecules back to the parallel state. Since the strength of the polyimide layer is considerably minor to that of  $V_{DC}$ , the relaxation time, about 700 s, is considerably higher than the response time in the switch-on phase.

From the measurements shown in Fig. 5.37, the phase decay time constant  $\tau$  for the different applied voltages can be obtained. Since the decay constant  $\tau$ , the initial angle,  $\psi(V = 0)$ , and the final angle,  $\psi(V = V_{DC})$ , are known from the measurements, it is possible to define the radiation angle along time as

$$\psi(t, V_{DC}) = [\psi(V = 0) - \psi(V = V_{DC})] \cdot e^{-t/\tau} + \psi(V = V_{DC}). \quad (5.9)$$

Using (5.9) and the time constants obtained from Figs. 5.37 and 5.38, the time the CRLH based LWA needs to reach the aimed beam steering for the different tuning states can be calculated. This time is shown in Fig. 5.39 for different voltages.

Table 5.3: Time constant  $\tau$  and needed time to reach the aimed radiation angle for different tuning voltages from  $\psi(0V) = -6^\circ$

$V_{DC}/V$	$\tau/s$	$t_{\text{tune}}/s$	$\psi(V_{DC})/^\circ$
30	41	234	3
60	11.45	67.3	4
120	1.78	9	9

Table 5.3 shows the correspondence between the applied voltage  $V_{DC}$ , the time constant  $\tau$  and the absolute response time  $t_{\text{tune}}$ , in seconds, for 99% of the total beam steering  $\psi(V_{DC})$  reached. As it can be seen, the stronger the static electric field applied, the faster the desired angle will be reached.

For the maximum biasing voltage  $V_{DC_{MAX}} = 120V$  the CRLH LWA needs 9s to steer the beam from  $-6^\circ$  to  $9^\circ$ . The size of the cavity and, hence, the volume of liquid crystal has an enormous influence on the response time of the liquid crystal material since this response time is directly proportional to the square of the cavity height [68]. Consequently, the response time of the leaky wave antenna can be reduced by decreasing the LC cavity height.

In this chapter, two liquid crystal based tunable composite right-/left-handed leaky wave antenna prototypes have been presented. The tuning of the liquid crystal is achieved by magnetic and electric biasing techniques specifically designed for planar structures. The different prototypes have been designed and manufactured for each biasing technique. For the electric biasing, highly resistive NiCr lines are integrated in the unit cell layout.

The tuning of the liquid crystal and comparison of both prototypes has been done by simulation and measurements of the S-parameters, dispersion characteristics, and far field patterns. From the measured far field pattern of each prototype, the corresponding radiation angles are extracted and a beam scanning range of  $\pm 11^\circ$  at 27 GHz is achieved with the magnetically biased LWA and  $\pm 15^\circ$  at 26.7 GHz for the electrically biased LWA, regarding broadside.

As a result, the electric biasing provides similar or better tuning behavior as the magnetic one with the further advantage of avoiding the manipulation of bulky magnets and being easily integratable in the unit cell layout. This electric biasing technique can be easily applied not only to leaky wave antennas but also to different types of planar voltage tunable components such as tunable phase shifters and filters.



---

## CONCLUSION AND OUTLOOK

---

The use of metamaterials for radiating structures is highly advantageous, since they not only allow the size of the designed structure to be minimized, but also their dispersive response can be tailored to obtain the desired propagation constant, impedance, and group velocity. This flexibility enables the design of propagation and stopbands responsible for the radiation performance of the presented metamaterial based leaky wave antenna. Moreover, by adding a tunable material such as liquid crystal to the metamaterial configuration, a tunable response of the leaky wave antenna can be achieved. The liquid crystal material allows for varying the effective permittivity encountered by the wave propagating within the leaky wave antenna, providing the antenna with tunability, i.e. beam steering capability without modifying its RF structure.

Among the many advantages that justify the choice of leaky wave antennas for this work are high directivity, narrow bandwidth, and a simple feeding network. Furthermore, the radiation angle for this kind of antennas is defined as a function of the phase shift. This relation facilitates control of the radiation angle either by frequency scanning or for a fixed frequency by changing the phase shift of the propagating wave. The latter can be done combining the leaky wave antenna principle with liquid crystal based tunable metamaterials.

The combination of the leaky wave antenna principle with tunable metamaterials offers a new and unique range of advantages adding planarity, low profile and continuous radiation from backfire to endfire through broadside to those of regular LWAs. Moreover, the combination of these two concepts allows beam scanning at higher frequencies to be performed such as mm-

wave bands and THz, which is a promising field of applications for tunable antennas and metamaterials.

The CRLH unit cell phase shift can be tailored by designing the geometry of the distributed lumped elements that conform the unit cell. This enables control of the radiation angle of the antenna along frequency or for a fixed operation frequency. The radiation at the broadside direction corresponds to the frequency for which the phase shift equals zero, while the group velocity is greater than zero, which is a unique feature of the CRLH unit cell that can not be achieved by other metamaterial unit cell configurations. This is the basis for the broadside radiation of the leaky wave antenna. This implies that, even when the phase shift equals zero, the energy still propagates for this frequency and, hence, there is radiation.

To achieve tunability tunable components are required, which have to be incorporated into the unit cell thus the layout of the unit cell has to be modified. The tunability of the leaky wave antenna and, hence, its beam scanning performance is limited by the tunability of its tunable components, i.e. the liquid crystal based interdigital varactors. The LC varactors show a tunability of 11.33%, which is limited, in turn, by the material tunability of the liquid crystal of 24.5%.

The leaky wave antennas presented in this work are made up of a periodic repetition of a metamaterial unit cell. The novel unit cell layout and geometry are investigated, designed, and fabricated to provide a CRLH dispersion characteristic, while simultaneously enabling the continuous beam scanning capability. To do so, the liquid crystal based varactors are built in as a series interdigital capacitor or a distributed capacitance. Overcoming the technological constraints while delivering the desired tunable dispersion characteristic at the operating frequency was one of the most significant challenges of this work. For this purpose, different materials and techniques have been tested. A glass substrate is used for the RF metalization and a brass block for the ground plane. Different approaches are tested to introduce the RF signal into the completely mounted LWA such as bonding wires or coaxial K-connectors.

The radiation at the broadside direction is possible even if the CRLH based radiating structure is unbalanced due to the high losses around the stopband. Besides, losses do not only provoke a frequency shift of the stop and propagating bands but also influence the steepness of the phase shift per unit cell curve, which has a direct impact on the radiation angle of the leaky wave antenna. This effect is emphasized by the higher order modes that are excited at

the discontinuities of the unit cell. The metallic losses of the RF metalization are the ones that contribute most to this effect.

The manufacturing process of the leaky wave antenna contributes enormously to the scanning behavior of the antenna and its matching. The varactors, implemented in the form of interdigital capacitors, are susceptible to fabrication tolerances that significantly influence the dispersion characteristic of the leaky wave antenna, since the deviation from the designed parameters can directly affect the propagation and stopbands of the antenna. Maintaining the designed IDC geometry and dimensions is one of the most challenging aspects during the manufacturing process. This challenge increases, the higher the operating frequency and the number of unit cells of the leaky wave antenna.

Two prototypes of the metamaterial based leaky wave antenna are presented within the frame of this work: First, a fifteen unit cell magnetically biased prototype for proof-of-concept purposes in the laboratory and, second, an electrically biased prototype with thirty two unit cells for real world applications. For the magnetically biased leaky wave antenna a biasing setup is designed and fabricated. The setup contains two magnets positioned above and below the antenna to maximize the magnetic flux that flows through the liquid crystal cavity. As a result, the liquid crystal molecules are oriented by following the static magnetic field lines. However, the bulkiness of the magnets and difficulty to manipulate them represent a significant drawback for the use of this biasing technique. To overcome this inconvenience, an electrically biasing network is designed and integrated in the layout of the unit cell. This biasing technique offers the advantages of planarity, easy integration and manufacturing, and facilitates the tuning of the antenna. The biasing network is implemented by means of high resistive nickel-chromium biasing lines that distribute the biasing voltages along the leaky wave antenna.

For both, the magnetically biased and the electrically biased antenna prototypes, the phase shift, the Bloch impedance, the radiation angle and the beam scanning range are simulated and measured. Furthermore, applying the array factor method and considering the leaky wave antenna as an array of isotropic radiators, the far field pattern is calculated. Although both antennas are designed to provide beam scanning through the broadside direction at a fixed frequency, they can also be operated in the left-handed and right-handed propagation bands, i.e. the backward and forward quadrants, which implies that this configuration could also perform frequency scanning if required.

For the magnetically biased leaky wave antenna, a directivity of 13.4 dBi and scanning range of  $42.6^\circ$  around broadside is expected from the phase shift measurements. When the far field pattern is measured with the antenna within the designed setup, a beam scanning range of  $11^\circ$  can be achieved. This effect is a consequence of positioning the biasing magnets above and below the leaky wave antenna. The resulting increase of distance between the magnets and the antenna provokes the static magnetic field that flows through the cavity where the liquid crystal is contained to be weaker. The weaker static magnetic field is not sufficient to reorient the majority of the liquid crystal molecules, leading to a smaller scanning range. This effect is overcome by the usage of electric biasing, which provides similar or better tuning behavior as the magnetic one with the further advantage of avoiding the manipulation of bulky magnets and being easily integratable in the unit cell layout. This electric biasing technique can be easily applied not only to leaky wave antennas but also to different types of planar voltage tunable components such as tunable phase shifters and filters.

The electrically biased leaky wave antenna is operated at 26.7 GHz. For this operation frequency, the antenna shows a beam scanning of  $15^\circ$  around broadside with a directivity above 15.8 dBi. The two stopbands that delimit the left-handed propagation band enforce a high phase shift variation per unit cell. This significant variation complicates the impedance matching of the antenna, and increases the losses in the left-handed propagation band. As a consequence, the left-handed band suffers a degradation of the beam amplitude and the side lobe level with respect to the right-handed propagation band. As a result, a half power beamwidth better than  $29.9^\circ$  and a side lobe level of minimum  $-13$  dB is obtained. The directivity, half power beamwidth, and side lobe level are limited by the number of unit cells that form the antenna. By increasing the number of unit cells, these parameters can be enhanced [79]. This increment of the number of unit cells improves the gain and the side lobe level but has no effect on the beam scanning range. The polarization of the leaky wave antenna plays an important role. For the electrically biased antenna the measured cross polarization is  $-25$  dB for both biased and unbiased states.

Current technological evolution leads to real time applications, where fast response times are a crucial matter. Although liquid crystal is slower than other technologies such as semiconductors, it is very well suited for high frequency real time systems with middle to high latency such as satellite communications [101, 102]. For the operating frequency of 26.7 GHz, if a

maximum biasing voltage of 120 V is applied, the LC needs approximately 9 s to perform the maximum possible beam scanning. Applying higher tuning voltages does not influence the beam scanning but decreases the response time of the liquid crystal. The relaxation time, about 700 s, is considerably higher than the response time in the switch-on phase, since the force that orients the liquid crystal molecules back to the unbiased configuration is much weaker than that applied for the biasing. This limits its application to slow beam scanning operation.

In conclusion, the first voltage tunable metamaterial based leaky wave antenna that performs continuous beam scanning from the backward to the forward quadrant through broadside operating at the Ka-Band is presented in this thesis. Other works that have addressed this same goal have only proved successful at lower frequencies, below 10 GHz. At the present moment, the leaky wave antenna presented in this work is the only fabricated and full working prototype of a voltage tunable metamaterial based leaky wave antenna capable of performing continuous beam scanning from the backward quadrant to the forward quadrant, through broadside direction, at the Ka-Band.

On the basis of the results obtained in this work, there are mainly two aspects that have to be addressed towards a marketable product in future: an efficient method to achieve optimal matching and an automation of the manufacturing process.

Metamaterial based antennas are very narrow band structures, which means they are matched only for a very particular frequency. The addition of a tunable matching network to the complete system could not only reduce the insertion losses of the antenna but also allow its usage at different frequencies. This would be advantageous for applications such as mm-wave systems such as LTE Advanced, 5G or Mobile Backhaul, where multiband antennas are used to provide different services within the same hardware. Additionally, placing several of these antennas in parallel it is possible to perform beam scanning in two dimensions, covering the whole space above the antenna array.

An efficient automated manufacturing process is still required and one of the major challenges when it comes to the utilization of planar metamaterial based antennas in real systems. A mechanized manufacturing process would enable an increase of the number of unit cells as required, enhancing the

directivity, half power beamwidth, and side lobe level of the produced leaky wave antenna.

Moreover, since the performance of LC increases with frequency [66], the voltage tunable leaky wave antenna principle presented in this work can also be used for higher frequency applications such as automotive radar at 77 GHz where continuous beam scanning is required, satellite communications with middle to high latency such as remote sensing or direct broadcast satellite, or communication and image systems at mm-waves and THz.

# A

---

## APPENDIX

---

### A.1 CAPACITANCE CALCULATION METHOD FOR MULTILAYERED SUBSTRATE BASED INTERDIGITAL CAPACITORS

The capacitance of the periodical section  $C_n$  is based on an IDC configuration with a minimum of three fingers and is the sum of partial capacitances due to the multilayered profile, i.e. the influence of the substrate and cover layer are taken into account in this calculation. Thus,  $C_n$  is defined as [91]

$$C_n = (n - 3)\varepsilon_0\varepsilon_{en}\frac{K(k)}{K'(k)}l \quad (\text{A.1})$$

where the relative permittivity is defined as

$$\varepsilon_{en} = 1 + q_{11}\frac{\varepsilon_1 - 1}{2} + q_{21}\frac{\varepsilon_2 - 1}{2}, \quad (\text{A.2})$$

$$q_{in} = \frac{K(k_{in})}{K(k'_{in})} \cdot \frac{K(k'_0)}{K(k_0)}, \quad (\text{A.3})$$

$$k_{in} = \frac{\sinh\left(\frac{\pi f_w}{4h_i}\right)}{\sinh\left(\frac{\pi(f_w + g)}{4h_i}\right)} \cdot \sqrt{\frac{\cosh^2\left(\frac{\pi(f_w + g)}{4h_i}\right) + \sinh^2\left(\frac{\pi(f_w + g)}{4h_i}\right)}{\cosh^2\left(\frac{\pi f_w}{4h_i}\right) + \sinh^2\left(\frac{\pi(f_w + g)}{4h_i}\right)}}, \quad (\text{A.4})$$

and

$$k'_i = \sqrt{1 - k_i^2}. \quad (\text{A.5})$$

The effect of the finite width external fingers is studied in  $C_3$  for a three fingered IDC. In  $C_{\text{end}}$ , the fringing fields that appear at the end of the finger strip and near the corners of the IDC are considered. According to [91], the calculation of  $C_3$ , the capacitance of a three finger IDC section with finite width strips, and  $C_{\text{end}}$ , that due to the fingers ends, also for the finite width terminals case, can be done using the previous algorithm, adapted to the specific boundary conditions in each case. So, adapting the algorithm parameters to those of our unit cell,  $C_3$  is

$$C_3 = 4\epsilon_0\epsilon_{e3} \frac{K(k'_{03})}{K(k_{03})} l \quad (\text{A.6})$$

where

$$\epsilon_{e3} = 1 + q_{13} \frac{\epsilon_1 - 1}{2} + q_{23} \frac{\epsilon_2 - 1}{2}, \quad (\text{A.7})$$

and

$$q_{i3} = \frac{K(k_{i3})}{K(k'_{i3})} \cdot \frac{K(k'_{03})}{K(k_{03})}, i = 1, 2. \quad (\text{A.8})$$

In this case,

$$k_{03} = \frac{f_w}{f_w + 2g} \sqrt{\frac{1 - \left(\frac{f_w + 2g}{3f_w + 2g}\right)^2}{1 - \left(\frac{f_w}{3f_w + 2g}\right)^2}}, \quad (\text{A.9})$$

$$k_{i3} = \frac{\sinh\left(\frac{\pi f_w}{4h_i}\right)}{\sinh\left(\frac{\pi(f_w + 2g)}{4h_i}\right)} \cdot \sqrt{\frac{1 - \sinh^2\left(\frac{\pi(f_w + 2g)}{4h_i}\right) / \sinh^2\left(\frac{\pi(3f_w + 2g)}{4h_i}\right)}{1 - \sinh^2\left(\frac{\pi f_w}{4h_i}\right) / \sinh^2\left(\frac{\pi(3f_w + 2g)}{4h_i}\right)}}, \quad (\text{A.10})$$

and

$$k'_{i3} = \sqrt{1 - k_{i3}^2}, i = 1, 2. \quad (\text{A.11})$$

For  $C_{\text{end}}$  not only the gap between fingers is taken into account in the calculations but also a central finger strip and the IDC section in front of it.

Approximating this field with a regular field distribution [91] the end capacitance of the  $n$  fingers is

$$C_{\text{end}} = 4n (f_w/2) \varepsilon_0 \varepsilon_{\text{end}} \frac{K(k_{0\text{end}})}{K(k'_{0\text{end}})} l \quad (\text{A.12})$$

where

$$\varepsilon_{\text{end}} = 1 + q_{1\text{end}} \frac{\varepsilon_1 - 1}{2} + q_{2\text{end}} \frac{\varepsilon_2 - 1}{2}, \quad (\text{A.13})$$

and

$$q_{i\text{end}} = \frac{K(k_{i\text{end}})}{K(k'_{i\text{end}})} \cdot \frac{K(k'_{0\text{end}})}{K(k_{0\text{end}})}, i = 1, 2. \quad (\text{A.14})$$

$k_{0\text{end}}$  and  $k_{i\text{end}}$  are,

$$k_{0\text{end}} = \frac{f_w}{f_w + 2g} \sqrt{\frac{1 - \left(\frac{f_w + 2g}{3f_w + 2g}\right)^2}{1 - \left(\frac{f_w}{3f_w + 2g}\right)^2}}, \quad (\text{A.15})$$

and

$$k_{i\text{end}} = \frac{\sinh\left(\frac{\pi f_w}{4h_i}\right)}{\sinh\left(\frac{\pi(f_w + g)}{4h_i}\right)}, \quad (\text{A.16})$$

respectively. It can be observed that equations A.9 and A.15 are exactly the same. This is a consequence of particularizing the algorithm to the dimensions of our unit cell, where all fingers, internal and external, have the same width and same gap between fingers and between fingers and their corresponding front sections.

## A.2 INDUCTANCE CALCULATION METHOD FOR A COMPOSITE RIGHT-/LEFT-HANDED UNIT CELL MEANDER INDUCTOR

The widely used standard algorithm used in [103] to calculate inductances on a microstrip substrate lacks, however, enough accuracy in the case of a meander line. To overcome this, the more suitable algorithm from [92] is applied.

The general total inductance of a meander line based on microstrip technology is

$$L_T = L_{\text{self}} + M_T, \quad (\text{A.17})$$

where  $L_{\text{self}}$  and  $M_T$  are the self inductance and the mutual inductance, respectively.

The self inductance is, in this specific case, calculated as the sum of the inductances of all segments that form the meander

$$L_{\text{self}} = L_1 + L_2 + L_3 + L_4 + L_5 + L_6 = L_1 + 2L_2 + 2L_3 + L_6, \quad (\text{A.18})$$

since  $L_2 = L_4$  and  $L_3 = L_5$ . In addition, the inductance of the different sections is

$$L_i = 0.002l \left[ \ln \left( \frac{2l}{w_m + t} \right) + 0.50049 + \left( \frac{w + t}{3l} \right) \right], \quad (\text{A.19})$$

where  $w_m = 62 \mu\text{m}$  is the width of the meander line,  $t = 2 \mu\text{m}$  the thickness of the metallization, and  $l$  the length of the different sections. Given the approximation used in [92] the length of the different sections that form the meander is calculated. For the obtained lengths, their corresponding self inductances are represented in Table A.1 together with the total self inductance  $L_{\text{self}}$ . The mutual inductance  $M_T$  is also an addition of the mutual coupling

$L_1$	$L_2$	$L_3$	$L_6$	$L_{\text{self}}$
0.1452 nH	0.3394 nH	0.0731 nH	0.0072 nH	0.9774 nH

Table A.1: Total self Inductance and individual self inductances of the meander segments.

between the multiple meander segments, thus

$$M_T = M_1 + M_2 + M_3 + M_4 + M_5 + M_6. \quad (\text{A.20})$$

As seen in Table A.2 every of these inductances refers to the coupling of the different segments. Also in Table A.2 the values of such inductance and the total mutual inductance are listed.

Table A.2: Total mutual inductance  $M_T$  and mutual inductances of the corresponding sections  $M(i, j)$  in nH.

$M_1(2,4)/\text{nH}$	$M_2(2,6)/\text{nH}$	$M_3(4,6)/\text{nH}$	$M_4(1,3)/\text{nH}$	$M_5(3,5)/\text{nH}$	$M_6(1,5)/\text{nH}$	$M_T/\text{nH}$
$(\mu_0/2\pi) \cdot 61.6$	$(\mu_0/2\pi) \cdot 103$	$(\mu_0/2\pi) \cdot 730.5$	$(\mu_0/2\pi) \cdot 3.9$	$(\mu_0/2\pi) \cdot 2.4$	$(\mu_0/2\pi) \cdot 6.1$	0.3542



---

## LIST OF ABBREVIATIONS

---

ADS	Advanced Design System
BF33	Borofloat substrate
CRLH	Composite right-/left-handed
CST	Computer Simulation Technology
DS	Double serial line
DP	Double parallel line
D-CRLH	Dual composite right-/left-handed
FSS	Frequency selective surface
FR4	Flame retardant
GND	Ground
IDC, IDCs	Interdigital capacitor, interdigital capacitors
i.e.	That is
LWA, LWAs	Leaky wave antenna, leaky wave antennas
LC	Liquid crystal
MEMS	Microelectromechanical systems
NRD	Non-radiative dielectric waveguide
NiCr	Nickel Chromium
PET	Polyethylene terephthalate
RF	Radio frequency
UV	Ultraviolet



---

## LIST OF SYMBOLS

---

### A, a

---

AF	array factor
$\alpha$	attenuation constant

### B, b

---

$B$	magnetic flux density
$\beta$	phase constant
$\beta_0$	phase constant in free space
$\beta_{\max}, \beta_{\min}$	maximum phase constant, minimum phase constant

### C, c

---

$C, C'$	capacitance, per unit length capacitance
$C_{se}, C_{se}$	series capacitance, shunt capacitance
$C_L, C'_L$	left-handed capacitance, per unit length left-handed capacitance
$C_R, C'_R$	right-handed capacitance, per unit length right-handed capacitance
$C_{DC}, C'_L$	DC blocking capacitance

### D, d

---

$D$	antenna directivity
$\Delta\psi$	beam scanning range
$\delta$	angle in a complex plane used to define the lossy reaction to the electric field E

### E, e

---

$\vec{E}$	electric field strength
-----------	-------------------------

$\epsilon_0$	vacuum permittivity: $\epsilon_0 \approx 8.854 \cdot 10^{-12}$ F/m
$\epsilon_{\text{eff}}$	effective permittivity
$\epsilon_{r_{\parallel}}, \epsilon_{r_{\perp}}$	relative parallel, perpendicular permittivity of liquid crystal
$\epsilon$	relative error
$\eta_0$	vacuum wave impedance: $\eta_0 \approx 376.73 \Omega$

E, f


---

$f$	frequency
$f_{\text{ser}}, f_{\text{sh}}$	series frequency, shunt frequency
$f_0$	operation frequency
$f_w$	finger width of an interdigital capacitor
$\phi$	observation angle along plane XY

G, g


---

$\gamma$	complex propagation constant
gap	gap between the fingers of an interdigital capacitor

H, h


---

$h$	height of the liquid crystal cavity
$\vec{H}$	magnetic field strength
HPBW	half power beamwidth

I, i


---

$I$	current
-----	---------

J, j


---

$j$	imaginary unit
-----	----------------

K, k


---

$\vec{k}, k$	complex wavevector, complex wavenumber
$k_x, k_y, k_z$	$x, y, z$ component of the wavevector

$k_0$	wavenumber in vacuum
<hr/>	
L, l	
$L, L'$	inductance, per unit length inductance
$L_{se}, L_{sh}$	series inductance, shunt inductance
$L_L, L'_L$	left-handed inductance, per unit length left-handed inductance
$L_R, L'_R$	right-handed inductance, per unit length right-handed inductance
$L_{self}$	self inductance
$\lambda, \lambda_0$	wavelength, wavelength in free space
$l$	length of the unit cell
$L$	length of the aperture of a leaky wave antenna
<hr/>	
M, m	
$M$	mutual inductance
$\mu_0$	vacuum permeability: $\mu_0 \approx 1.257 \cdot 10^{-6}$ H/m
<hr/>	
N, n	
$\vec{n}$	director of the liquid crystal molecules
$N$	number of unit cells
<hr/>	
O, o	
$\omega$	angular frequency
$\omega_{se}, \omega_{sh}$	angular series frequency, angular shunt frequency
$\omega_0$	angular resonance frequency
<hr/>	
P, p	
$P, P_{rad}, P_{inj}$	power, radiated power, injected power
$\psi$	radiation angle with respect to broadside
$\psi_{max}$	maximum radiation angle with respect to broadside
$\psi_{min}$	minimum radiation angle with respect to broadside

---

 R, r
 

---

 R, R'      resistance
 

---

 S, s
 

---

 $\sigma$       electric conductivity
 

---

 SLL      side lobe level
 

---

 T, t
 

---

*t*      thickness of the RF metalization, time
 

---

*t*<sub>tune</sub>      time needed to perform the desired beam scanning
 

---

 $\tau$       tunability, time constant
 

---

 $\theta$       observation angle along plane YZ
 

---

 V, v
 

---

*V*, *V*<sub>DC</sub>      voltage, DC applied voltage
 

---

*v*<sub>*p*</sub>, *v*<sub>*g*</sub>      phase velocity , group velocity
 

---

 X, x
 

---

*X*<sub>pol</sub>      cross polarization
 

---

 Y, y
 

---

*Y*, *Y*'      admittance, complex per unit length admittance
 

---

 Z, z
 

---

*Z*, *Z*'      impedance, complex per unit length impedance
 

---

*Z*<sub>*B*</sub>, *Z*<sub>*c*</sub>      complex Bloch impedance, complex characteristic impedance of a transmission line
 

---

---

## BIBLIOGRAPHY

---

- [1] D. Jackson, C. Caloz, and T. Itoh, "Leaky-wave antennas," *Proceedings of the IEEE*, vol. 100, no. 7, pp. 2194–2206, 2012.
- [2] S. Podilchak, A. Freundorfer, and Y. M. M. Antar, "Broadside radiation from a planar 2-d leaky-wave antenna by practical surface-wave launching," *Antennas and Wireless Propagation Letters, IEEE*, vol. 7, pp. 517–520, 2008.
- [3] C. Caloz, T. Itoh, and A. Rennings, "Crlh metamaterial leaky-wave and resonant antennas," *Antennas and Propagation Magazine, IEEE*, vol. 50, pp. 25–39, Oct 2008.
- [4] S. Paulotto, P. Baccarelli, F. Frezza, and D. Jackson, "Full-wave modal dispersion analysis and broadside optimization for a class of microstrip crlh leaky-wave antennas," *Microwave Theory and Techniques, IEEE Transactions on*, vol. 56, pp. 2826–2837, Dec 2008.
- [5] M. Hashemi and T. Itoh, "Evolution of composite right/left-handed leaky-wave antennas," *Proceedings of the IEEE*, vol. 99, pp. 1746–1754, Oct 2011.
- [6] S. Otto, A. Rennings, K. Solbach, and C. Caloz, "Transmission line modeling and asymptotic formulas for periodic leaky-wave antennas scanning through broadside," *Antennas and Propagation, IEEE Transactions on*, vol. 59, no. 10, pp. 3695–3709, 2011.
- [7] A. Grbic and G. Eleftheriades, "Experimental verification of backward-wave radiation from a negative refractive index metamaterial," *Journal of Applied Physics*, vol. 92, pp. 5930–5935, Nov 2002.
- [8] A. Grbic and G. Eleftheriades, "A backward-wave antenna based on negative refractive index 1-c networks," in *Antennas and Propagation Society International Symposium, 2002. IEEE*, vol. 4, pp. 340–343 vol.4, 2002.
- [9] G. Eleftheriades, A. Iyer, and P. Kremer, "Planar negative refractive index media using periodically 1-c loaded transmission lines," *Microwave Theory and Techniques, IEEE Transactions on*, vol. 50, pp. 2702–2712, Dec 2002.

- [10] L. Liu, C. Caloz, and T. Itoh, "Dominant mode leaky-wave antenna with backfire-to-endfire scanning capability," *Electronics Letters*, vol. 38, pp. 1414–1416, Nov 2002.
- [11] S. Eggermont, R. Platteborze, and I. Huynen, "Investigation of metamaterial leaky wave antenna based on complementary split ring resonators," in *Microwave Conference, 2009. EuMC 2009. European*, pp. 209–212, Sept 2009.
- [12] C. Liu and W. Menzel, "Frequency-scanned leaky-wave antenna from negative refractive index transmission lines," in *Antennas and Propagation, 2007. EuCAP 2007. The Second European Conference on*, pp. 1–4, Nov 2007.
- [13] D. Upadhyay and S. Pal, "Design of full scanning miniaturized antenna using left handed materials," in *Devices and Communications (ICDeCom), 2011 International Conference on*, pp. 1–4, Feb 2011.
- [14] D. Upadhyay and S. Pal, "Design of miniaturized dominant mode leaky-wave antenna using left handed metamaterials," in *Devices and Communications (ICDeCom), 2011 International Conference on*, pp. 1–4, Feb 2011.
- [15] R. Goto, H. Deguchi, and M. Tsuji, "Composite right/left-handed transmission lines based on conductor-backed coplanar strips for antenna application," in *Microwave Conference, 2006. 36th European*, pp. 1040–1043, Sept 2006.
- [16] A. Hamdi, A. Kouki, and A. Samet, "Leaky coplanar waveguide antenna with tunable beamwidth and radiation angle using composite right/left-handed materials," in *Quantum, Nano and Micro Technologies, 2009. IC-QNM '09. Third International Conference on*, pp. 152–156, Feb 2009.
- [17] R. Ogaki, D. Inada, H. Deguchi, and M. Tsuji, "New unit-cell structures of crlh-tl for antenna application," in *Antennas and Propagation (APSURSI), 2011 IEEE International Symposium on*, pp. 2857–2860, July 2011.
- [18] Y.-J. Chi and F.-C. Chen, "Novel crlh leaky wave antenna with horizontal scanning property," in *Microwave Conference Proceedings (APMC), 2011 Asia-Pacific*, pp. 935–938, Dec 2011.
- [19] Y. Sasaki, A. Sanada, and H. Kubo, "Slotted composite right/left-handed strip lines for leaky wave antenna applications," in *Microwave Conference, 2006. APMC 2006. Asia-Pacific*, pp. 923–926, Dec 2006.

- [20] G. Zamora, S. Zuffanelli, F. Paredes, F. Herraiz-Martinez, F. Martin, and J. Bonache, "Leaky-wave antenna (lwa) based on slot line and non-bianisotropic split ring resonators (nb-srrs) and comparison with cpw approach," in *Antennas and Propagation in Wireless Communications (APWC), 2014 IEEE-APS Topical Conference on*, pp. 48–51, Aug 2014.
- [21] L. Markley and G. Eleftheriades, "A metamaterial transition layer for free-space radiation from a slot-line leaky-wave antenna," in *Antennas and Propagation Society International Symposium (APSURSI), 2014 IEEE*, pp. 759–760, July 2014.
- [22] Y. Weitsch and T. Eibert, "A left-handed/right-handed leaky-wave antenna derived from slotted rectangular hollow waveguide," in *Proc. European Microwave Conference*, pp. 917–920, 2007.
- [23] C. Damm, M. Maasch, R. Gonzalo, and R. Jakoby, "Tunable composite right/left-handed leaky wave antenna based on a rectangular waveguide using liquid crystals," pp. 13–16, may. 2010.
- [24] T. Yang, P.-L. Chi, and R.-M. Xu, "Novel composite right/left-handed leaky-wave antennas based on the folded substrate-integrated-waveguide structures," *Progress In Electromagnetics Research C*, vol. 29, pp. 235–248, 2006. doi:10.2528/PIERC12040215.
- [25] J. Machac and M. Polivka, "A dual band crlh substrate integrated waveguide leaky wave antenna," in *Microwave Conference (EuMC), 2011 41st European*, pp. 535–538, Oct 2011.
- [26] Q. Yang, X. Zhang, and Y. Zhang, "A shunt-capacitance-aided composite right/left-handed leaky wave antenna with large scanning-range/bandwidth ratio," in *Progress In Electromagnetics Research Symposium Proceedings, Moscow, Russia, August 19-23, 2012*.
- [27] J. Machac, M. Polivka, and K. Zemlyakov, "A dual band leaky wave antenna on a crlh substrate integrated waveguide," *Antennas and Propagation, IEEE Transactions on*, vol. 61, pp. 3876–3879, July 2013.
- [28] O. Losito, M. Gallo, V. Dimiccoli, D. Barletta, and M. Bozzetti, "A tapered design of a crlh-tl leaky wave antenna," in *Antennas and Propagation (EUCAP), Proceedings of the 5th European Conference on*, pp. 357–360, April 2011.

- [29] J. Jacome-Munoz, J. Gomez-Diaz, J. Perruisseau-Carrier, and A. Alvarez-Melcon, "A tapered crlh mushroom-like leaky wave antenna with reduced sidelobe level," in *Antennas and Propagation (EuCAP), 2014 8th European Conference on*, pp. 588–592, April 2014.
- [30] H. Wang, W. Hu, Y. Sun, L. Dong, Y. He, and L. Si, "Design for microstrip leaky wave antenna based on srr structure," in *Microwave Technology Computational Electromagnetics (ICMTCE), 2013 IEEE International Conference on*, pp. 160–163, Aug 2013.
- [31] S. Eggermont and I. Huynen, "Influence of number of rings on radiation of csrr-loaded leaky wave antenna," in *Antennas and Propagation (EUCAP), Proceedings of the 5th European Conference on*, pp. 1227–1229, April 2011.
- [32] F. Casares-Miranda, C. Camacho-Penalosa, and C. Caloz, "Active composite right/left-handed leaky-wave antennas," in *Antennas and Propagation Society International Symposium 2006, IEEE*, pp. 23–26, July 2006.
- [33] D. Piazza, M. Capacchione, and M. D'Amico, "Crlh leaky wave antenna with tunable polarization," in *Antennas and Propagation (EuCAP), 2010 Proceedings of the Fourth European Conference on*, pp. 1–5, April 2010.
- [34] M. Hashemi and T. Itoh, "Novel composite right/left-handed leaky-wave antennas," in *Antennas and Propagation, 2009. EuCAP 2009. 3rd European Conference on*, pp. 606–610, March 2009.
- [35] F. Bilotti, A. Aluf, N. Engheta, and L. Vegni, "Leaky-wave metamaterial antennas: Conical and pencil beam radiation," in *Antennas and Propagation, 2007. EuCAP 2007. The Second European Conference on*, pp. 1–5, Nov 2007.
- [36] J. Liu, D. Jackson, and Y. Long, "Substrate integrated waveguide (siw) leaky-wave antenna with transverse slots," *Antennas and Propagation, IEEE Transactions on*, vol. 60, no. 1, pp. 20–29, 2012.
- [37] M. Hashemi and T. Itoh, "Dispersion engineered metamaterial-based transmission line for conformal surface application," in *Microwave Symposium Digest, 2008 IEEE MTT-S International*, pp. 331–334, 2008.
- [38] T. Kodera and C. Caloz, "Uniform ferrite-loaded open waveguide structure with crlh response and its application to a novel backfire-to-endfire leaky-wave antenna," *Microwave Theory and Techniques, IEEE Transactions on*, vol. 57, no. 4, pp. 784–795, 2009.

- [39] S. Lim, C. Caloz, and T. Itoh, "Electronically scanned composite right/left handed microstrip leaky-wave antenna," *Microwave and Wireless Components Letters, IEEE*, vol. 14, pp. 277–279, June 2004.
- [40] S. Lim, K. Leong, and T. Itoh, "Novel reconfigurable leaky-wave aperture with tunable directivity," in *Antennas and Propagation Society International Symposium, 2005 IEEE*, vol. 1B, pp. 381–384 vol. 1B, 2005.
- [41] L. Huang, J.-C. Chiao, and P. De Lisio, "An electronically switchable leaky wave antenna," *Antennas and Propagation, IEEE Transactions on*, vol. 48, no. 11, pp. 1769–1772, 2000.
- [42] S. Mueller, F. Goelden, P. Scheele, M. Wittek, C. Hock, and R. Jakoby, "Passive phase shifter for w-band applications using liquid crystals," in *Microwave Conference, 2006. 36th European*, pp. 306–309, sept. 2006.
- [43] C. Simovski, I. Kolmakov, and S. Tretyakov, "Approaches to the homogenization of periodical metamaterials," in *Mathematical Methods in Electromagnetic Theory, 2006 International Conference on*, pp. 41–44, 2006.
- [44] D. Pozar, *Microwave Engineering*. John Wiley & Sons, John, 4ed., 2011.
- [45] C. Caloz and T. Itoh, *Electromagnetic metamaterials: transmission line theory and microwave applications*. Wiley-IEEE Press, 2005.
- [46] S. Tretyakov, P. Barois, V. Scharf, T. Kruglyak, and I. Bergmair, "Nanos-structured metamaterials," 2010.
- [47] R. M. Foster, "A reactance theorem," *Bell System Technical Journal, The*, vol. 3, pp. 259–267, April 1924.
- [48] C. Caloz and T. Itoh, "Novel microwave devices and structures based on the transmission line approach of meta-materials," in *Microwave Symposium Digest, 2003 IEEE MTT-S International*, vol. 1, pp. 195–198 vol.1, 2003.
- [49] J. P. Turpin, J. A. Bossard, K. L. Morgan, D. H. Werner, and P. L. Werner, "Reconfigurable and tunable metamaterials: A review of the theory and applications," *International Journal of Antennas and Propagation*, p. 18 pages, 2014. Article ID 429837, doi:10.1155/2014/429837.
- [50] S. Lim, C. Caloz, and T. Itoh, "Electronically-controlled metamaterial-based transmission line as a continuous-scanning leaky-wave antenna,"

- Microwave Symposium Digest, 2004 IEEE MTT-S International, vol. 1, June 2004, pp. 313 – 316 Vol.1., 2004.*
- [51] S. Lim, C. Caloz, and T. Itoh, "Metamaterial-based electronically controlled transmission-line structure as a novel leaky-wave antenna with tunable radiation angle and beamwidth," *Microwave Theory and Techniques, IEEE Transactions on*, vol. 53, pp. 161 – 173, Jan. 2005.
- [52] J. Fu, X. Li, Q. Wu, and C. Feng, "Metamaterial based electronically-scanned circularly-polarized lwa," *Magnetics, IEEE Transactions on*, vol. 48, pp. 4301–4304, Nov 2012.
- [53] J. Perruisseau-Carrier, K. Topalli, and T. Akin, "Low-loss ku-band artificial transmission line with mems tuning capability," *Microwave and Wireless Components Letters, IEEE*, vol. 19, pp. 377–379, June 2009.
- [54] T. Kim, J. Kang, W. Che, and L. Vietzorreck, "Development of a tunable antenna using rf-mems based crlh-transmission lines," in *Applied Electromagnetics and Communications (ICECom), 2013 21st International Conference on*, pp. 1–3, Oct 2013.
- [55] H. Nguyen, S. Abielmona, and C. Caloz, "Performance-enhanced and symmetric full-space scanning end-switched crlh lwa," *Antennas and Wireless Propagation Letters, IEEE*, vol. 10, pp. 709–712, 2011.
- [56] D. Goshi, K. Leong, and T. Itoh, "Mode switching for printed antenna structures," in *Antennas and Propagation, 2006. EuCAP 2006. First European Conference on*, pp. 1–4, Nov 2006.
- [57] H. Tao, A. C. Strikwerda, K. Fan, W. J. Padilla, X. Zhang, and R. D. Averitt, "Mems based structurally tunable metamaterials at terahertz frequencies," *Journal of Infrared, Millimeter, and Terahertz Waves*, vol. 32, no. 5, pp. 580–595, 2011.
- [58] K. Fuchi, A. Diaz, E. J. Rothwell, R. O. Ouedraogo, and J. Tang, "An origami tunable metamaterial," *Journal of Applied Physics*, vol. 111, no. 8, 2012.
- [59] I. M. Pryce, K. Aydin, Y. A. Kelaita, R. M. Briggs, and H. A. Atwater, "Highly strained compliant optical metamaterials with large frequency tunability," *Nano letters*, vol. 10, no. 10, pp. 4222–4227, 2010.

- [60] H.-T. Chen, W. J. Padilla, J. M. O. Zide, A. C. Gossard, A. J. Taylor, and R. D. Averitt, "Active terahertz metamaterial devices," *Nature*, vol. 444, no. 7119, p. 597–600, 2006.
- [61] J. Han and A. Lakhtakia, "Semiconductor split-ring resonators for thermally tunable terahertz metamaterials," *Journal of Modern Optics*, vol. 56, no. 4, pp. 554–557, 2009.
- [62] L. Kang, Q. Zhao, H. Zhao, and J. Zhou, "Magnetically tunable negative permeability metamaterial composed by split ring resonators and ferrite rods," *Optics express*, vol. 16, no. 12, pp. 8825–8834, 2008.
- [63] E. Ozbay, K. Aydin, S. Butun, K. Kolodziejek, and D. Pawlak, "Ferroelectric based tuneable srr based metamaterial for microwave applications," in *Microwave Conference, 2007. European*, pp. 497–499, Oct 2007.
- [64] M. Gil, C. Damm, A. Giere, M. Sazegar, J. Bonache, R. Jakoby, and F. Martin, "Electrically tunable split-ring resonators at microwave frequencies based on barium-strontium-titanate thick films," *Electronics Letters*, vol. 45, pp. 417–418, April 2009.
- [65] C. Weickhmann, R. Jakoby, E. Constable, and R. Lewis, "Time-domain spectroscopy of novel nematic liquid crystals in the terahertz range," in *Infrared, Millimeter, and Terahertz Waves (IRMMW-THz), 2013 38th International Conference on*, pp. 1–2, Sept 2013.
- [66] S. Mueller, A. Moessinger, R. Marin, F. Goelden, A. Lapanik, W. Haase, and R. Jakoby, "Liquid crystals-microwave characterization and tunable devices," *Frequenz*, vol. 61, pp. 217–223, 10 2007.
- [67] M. Maasch, M. Roig, C. Damm, and R. Jakoby, "Voltage-tunable artificial gradient-index lens based on a liquid crystal loaded fishnet metamaterial," *Antennas and Wireless Propagation Letters, IEEE*, vol. 13, pp. 1581–1584, 2014.
- [68] F. Goelden, A. Gäbler, S. Müller, A. Lapanik, W. Haase, and R. Jakoby, "Liquid-crystal varactors with fast switching times for microwave applications," *Electronics Letters*, vol. 44, no. 7, pp. 480–481, 2008.
- [69] T. Uchida, *Liquid Crystals: Applications and Uses*. No. v. 3 in *Liquid Crystals: Applications and Uses*, World Scientific, 1992.
- [70] A. Sonin, *The Surface Physics of Liquid Crystals*. Gordon and Breach Publishers, 1995.

- [71] F. Goelden, *Liquid Crystal Based Microwave Components with Fast Response Times: Material, Technology, Power Handling Capability*. PhD thesis, Technische Universität Darmstadt, 2009.
- [72] Karabey, *Electronic Beam Steering and Polarization Agile Planar Antennas in Liquid Crystal Technology*. PhD thesis, Technische Universität Darmstadt, 2014.
- [73] V. V. Varadan and R. Ro, "Unique retrieval of complex permittivity and permeability of dispersive materials from reflection and transmitted fields by enforcing causality," *Microwave Theory and Techniques, IEEE Transactions on*, vol. 55, pp. 2224–2230, oct. 2007.
- [74] J. Sheen, "Comparisons of microwave dielectric property measurements by transmission/reflection techniques and resonance techniques," *Measurement Science and Technology*, vol. 20, 2001.
- [75] D. R. Smith and J. B. Pendry, "Homogenization of metamaterials by field averaging (invited paper)," *Journal of the Optical Society of America*, vol. 23, pp. 391–403, 2006.
- [76] C. R. Simovski and S. A. Tretyakov, "Local constitutive parameters of metamaterials from an effective-medium perspective," *Phys. Rev. B*, vol. 75, p. 195111, May 2007.
- [77] C. Simovski, "Material parameters of metamaterials (a review)," *Optics and Spectroscopy*, vol. 107, no. 5, pp. 726–753, 2009.
- [78] C. Simovski, "On electromagnetic characterization and homogenization of nanostructured metamaterials," *Journal of Optics*, vol. 13, no. 1, pp. 1–22, 2011.
- [79] A. A. Oliner and D. R. Jackson, *Leaky-wave antennas*, in *Antenna Engineering Handbook*, 4th ed., Chap. 11. McGraw-Hill, New York, 2007.
- [80] R. C. Johnson and H. Jasik, *Antenna Engineering Handbook*. New York, NY: McGraw-Hill, 1984.
- [81] F. Zucker, *Surface- and Leaky-Wave Antennas*, vol. Antenna Engineering Handbook. New York: McGraw-Hill, 1 ed., 1961.
- [82] C. Walter, *Traveling wave antennas*. McGraw-Hill electronic science series, New York: McGraw-Hill, 1965.

- [83] A. Sanchez and A. Oliner, "Microwave network analysis of a leaky-wave structure in non-radiative dielectric waveguide," in *Microwave Symposium Digest, 1984 IEEE MTT-S International*, pp. 118–120, May 1984.
- [84] A. Oliner, S. Peng, and K. Sheng, "Leakage from a gap in nrd guide," in *Microwave Symposium Digest, 1985 IEEE MTT-S International*, pp. 619–622, June 1985.
- [85] P. Pahlavan, M. Sorkherizi, A. Tadjalli, and S. Hosseini, "Frequency scanning in the uniform leaky-wave antenna based on nonradiative dielectric (nrd) waveguide," in *Electrical Engineering (ICEE), 2011 19th Iranian Conference on*, pp. 1–5, May 2011.
- [86] S. Tretyakov, *Analytical Modeling in Applied Electromagnetics*. Artech House electromagnetic analysis series, Artech House, 2003.
- [87] S. Paulotto, P. Baccarelli, F. Frezza, and D. Jackson, "A microstrip periodic leaky-wave antenna optimized for broadside scanning," in *Antennas and Propagation Society International Symposium, 2007 IEEE*, pp. 5789–5792, June 2007.
- [88] F. Schwing and S.-T. Peng, "Design of dielectric grating antennas for millimeter-wave applications," *Microwave Theory and Techniques, IEEE Transactions on*, vol. 31, pp. 199–209, Feb 1983.
- [89] C. A. Balanis, *Antenna Theory: Analysis and Design, Third Edition*,. Hoboken, NJ, Wiley, 2005.
- [90] C. Caloz and S. Otto, "A tour on recent developments and discoveries of crucial practical importance in leaky-wave antennas," in *Microwave Conference (EuMC), 2013 European*, pp. 495–498, Oct 2013.
- [91] S. Gevorgian, T. Martinsson, P. Linner, and E. Kollberg, "Cad models for multilayered substrate interdigital capacitors," *Microwave Theory and Techniques, IEEE Transactions on*, vol. 44, pp. 896–904, Jun 1996.
- [92] G. Stojanović, L. Živanov, and M. Damjanović, "Compact form of expressions for inductance calculation of meander inductors," *Serbian journal of electrical engineering*, vol. 1, no. 3, pp. 57–68, 2004.
- [93] C. Caloz and T. Itoh, "Array factor approach of leaky-wave antennas and application to 1-d/2-d composite right/left-handed (crlh) structures," *Microwave and Wireless Components Letters, IEEE*, vol. 14, pp. 274–276, June 2004.

- [94] T. Ueda, N. Michishita, M. Akiyama, and T. Itoh, "Dielectric-resonator-based composite right/left-handed transmission lines and their application to leaky wave antenna," *Microwave Theory and Techniques, IEEE Transactions on*, vol. 56, pp. 2259–2269, Oct 2008.
- [95] S. J. Orfanidis, *Electromagnetic Waves and Antennas*.
- [96] W. Stutzman and G. Thiele, *Antenna Theory and Design*. Wiley, 3rd ed., 2012.
- [97] K. Kelleher, W. Scott, and N. Marchand, "Cross polarization effects on antenna radiation patterns," in *1958 IRE International Convention Record*, vol. 4, pp. 153–159, March 1956.
- [98] A. Ludwig, "The definition of cross polarization," *Antennas and Propagation, IEEE Transactions on*, vol. 21, pp. 116–119, Jan 1973.
- [99] F. Casares-Miranda, C. Camacho-Penalosa, and C. Caloz, "High-gain active composite right/left-handed leaky-wave antenna," *Antennas and Propagation, IEEE Transactions on*, vol. 54, pp. 2292–2300, Aug 2006.
- [100] Y. Dong and T. Itoh, "Composite right/left-handed substrate integrated waveguide and half mode substrate integrated waveguide leaky-wave structures," *Antennas and Propagation, IEEE Transactions on*, vol. 59, pp. 767–775, March 2011.
- [101] A. Hoehn, P. Hager, and J. Harder, "Design characterization of an electronic steerable ka-band antenna using liquid crystal phase shifters," in *Aerospace Conference, 2013 IEEE*, pp. 1–14, March 2013.
- [102] C. Weickhmann, N. Nathrath, R. Gehring, A. Gaebler, M. Jost, and R. Jakoby, "A light-weight tunable liquid crystal phase shifter for an efficient phased array antenna," in *Microwave Conference (EuMC), 2013 European*, pp. 428–431, Oct 2013.
- [103] I. J. Bahl, *Lumped Elements for RF and Microwave Circuits*. Artech House, 2003.

---

## LIST OF PUBLICATIONS OF THE AUTHOR

---

- [Roig1] **M. Roig**, M. Maasch, C. Damm, and R. Jakoby, "Investigation and application of a liquid crystal loaded varactor in a voltage tunable crlh leaky-wave antenna at ka-band," *International Journal of Microwave and Wireless Technologies*, pp. 1–7, 7 2015.
- [Roig2] **M. Roig**, M. Maasch, C. Damm, and R. Jakoby, "Liquid crystal-based tunable crlh-transmission line for leaky wave antenna applications at ka-band," *International Journal of Microwave and Wireless Technologies*, vol. 6, pp. 325–330, March 2014.
- [Roig3] **M. Roig**, M. Maasch, C. Damm, and R. Jakoby, "Dynamic beam steering properties of an electrically tuned liquid crystal based crlh leaky wave antenna," *8th International Congress on Advanced Electromagnetic Materials in Microwaves and Optics - Metamaterials 2014 Copenhagen, Denmark, 25-30 August 2014*, 2014.
- [Roig4] **M. Roig**, M. Maasch, C. Damm, and R. Jakoby, "Electrically tunable liquid crystal based composite right/left-handed leaky-wave antenna at 26.7 GHz," in *Microwave Conference, 2014. 44<sup>th</sup> European*, Oct. 2014.
- [Roig5] M. Maasch, **M. Roig**, C. Damm, and R. Jakoby, "Voltage tunable artificial gradient-index lens based on a liquid crystal loaded fishnet metamaterial," *Antennas and Wireless Propagation Letters*, 2014.
- [Roig6] M. Maasch, **M. Roig**, C. Damm, and R. Jakoby, "Realization of a voltage tunable gradient-index fishnet loaded with liquid crystal," in *Metamaterials 2014*, 2014.
- [Roig7] **M. Roig**, M. Maasch, C. Damm, and R. Jakoby, "Steerable ka-band leaky wave antenna based on liquid crystal material," in *Advanced Electromagnetic Materials in Microwaves and Optics (METAMATERIALS)*, 2013 *7th International Congress on*, pp. 540–545, Sept 2013.
- [Roig8] **M. Roig**, M. Maasch, C. Damm, O. Karabey, and R. Jakoby, "Liquid crystal based tunable composite right/left-handed leaky-wave

antenna for ka-band applications," in *Microwave Conference, 2013. 43rd European*, oct. 2013.

- [Roig9] M. Maasch, **M. Roig**, C. Damm, and R. Jakoby, "Planar metamaterial with separately voltage tunable electric and magnetic dispersion based on liquid crystal," in *Advanced Electromagnetic Materials in Microwaves and Optics (METAMATERIALS), 2013 7th International Congress on*, pp. 556–559, Sept 2013.
- [Roig10] M. Maasch, **M. Roig**, C. Damm, and R. Jakoby, "Efficient farfield computation from eigenmode simulations for leaky-wave antennas," in *Antennas and Propagation Society International Symposium (APSURSI), 2013 IEEE*, pp. 1656–1657, July 2013.
- [Roig11] **M. Roig**, M. Sazegar, Y. Zheng, and R. Jakoby, "Tunable frequency selective surface based on ferroelectric ceramics for beam steering antennas," in *Microwave Conference (GeMiC), 2012 The 7th German*, pp. 1–4, March 2012.
- [Roig12] M. Maasch, O. Karabey, C. Damm, **M. Roig**, and R. Jakoby, "Investigation on the beam-scanning capability of a gradient index fishnet structure," in *Antennas and Propagation Society International Symposium (APSURSI), 2012 IEEE*, pp. 1–2, July 2012.

---

## AWARDS

---

- 2nd Prize Best Poster Award in Metamaterials 2013 for the contribution "Steerable ka-band leaky wave antenna based on liquid crystal material"



---

SUPERVISED BACHELOR-, MASTER-, AND DIPLOMA  
THESES

---

- Analysis and Implementation of Homogenization Methods based on Electromagnetic Eigenmode Simulations, Christian Steger, St-2192-B, 04.04.2013
- Design and Implementation of a Voltage Tunable Liquid Crystal based CRLH Leaky-Wave Antenna at Ka-Band, Xiyue Fang, St-2197, 22.08.2013



## CURRICULUM VITAE

### *Personal Information:*

Name	María Roig Parras
Date of birth	24.05.1983
Place of birth	Madrid, Spain
Nacionality	Spanish

### *Education:*

1998 – 2001	High School Education, Institut d'Educació Secundària L'Eliana, Valencia, Spain
09.2001 – 09.2008	Diploma in Telecommunications Engineering, Universitat Politècnica de València, Valencia, Spain
10.2008 – 12.2010	International Master Program – Information and Communication Engineering, Technische Universität Darmstadt, Darmstadt, Germany
02.2011 – 10.2015	Research assistant at Institute for Microwave Engineering and Photonics, Technische Universität Darmstadt, Darmstadt, Germany

Darmstadt, 14. July 2015

María Roig Parras